ICEBEAR-3D: An Advanced Low Elevation Angle Auroral E region Imaging Radar

A thesis submitted to the
College of Graduate and Postdoctoral Studies
in partial fulfillment of the requirements
for the degree of Master of Science
in the Department of Physics and Engineering Physics
University of Saskatchewan
Saskatoon

By
Adam Lozinsky

Permission to Use

In presenting this thesis in partial fulfillment of the requirements for a Postgraduate degree from the University of Saskatchewan, I agree that the Libraries of this University may make it freely available for inspection. I further agree that permission for copying of this thesis in any manner, in whole or in part, for scholarly purposes may be granted by the professor or professors who supervised my thesis work or, in their absence, by the Head of the Department or the Dean of the College in which my thesis work was done. It is understood that any copying or publication or use of this thesis or parts thereof for financial gain shall not be allowed without my written permission. It is also understood that due recognition shall be given to me and to the University of Saskatchewan in any scholarly use which may be made of any material in my thesis.

Disclaimer

Reference in this thesis to any specific commercial products, process, or service by trade name, trademark, manufacturer, or otherwise, does not constitute or imply its endorsement, recommendation, or favoring by the University of Saskatchewan. The views and opinions of the author expressed herein do not state or reflect those of the University of Saskatchewan, and shall not be used for advertising or product endorsement purposes.

Requests for permission to copy or to make other uses of materials in this thesis in whole or part should be addressed to:

Head of the Department of Physics and Engineering Physics
163 Physics Building
116 Science Place
University of Saskatchewan
Saskatoon, Saskatchewan
Canada
S7N 5E2

OR

Dean
College of Graduate and Postdoctoral Studies
University of Saskatchewan
116 Thorvaldson Building, 110 Science Place
Saskatoon, Saskatchewan S7N 5C9 Canada

Abstract

The Ionospheric Continuous-wave E region Bistatic Experimental Auroral Radar (ICEBEAR) is an auroral E region radar which has operated from 7 December 2017 until the September 2019. During the first two years of operation, ICEBEAR was only capable of spatially locating E region scatter and meteor trail targets in range and azimuth. Elevation angles were not determinable due to its East-West uniform linear receiving antenna array. Measuring elevation angles of targets when viewing from low elevation angles with radar interferometers has been a long standing problem. Past high latitude radars have attempted to obtain elevation angles of E region targets using North-South baselines, but have always resulted in erroneous elevation angles being measured in the low elevation regime (0° to $\approx 30^\circ$ above the horizon), leaving interesting scientific questions about scatter altitudes in the auroral E region unanswered. The work entailed in this thesis encompasses the design of the ICEBEAR-3D system for the acquisition of these important elevation angles.

The receiver antenna array was redesigned using a custom phase error minimization and stochastic antenna location perturbation technique, which produces phase tolerant receiver antenna arrays. The resulting 45-baseline sparse non-uniform coplanar T-shaped array was designed for aperture synthesis radar imaging. Conventional aperture synthesis radar imaging techniques assume point-like incoherent targets and image using a Cartesian basis over a narrow field of view. These methods are incompatible with horizon pointing E region radars such as ICEBEAR. Instead, radar targets were imaged using the Suppressed Spherical Wave Harmonic Transform (Suppressed-SWHT) technique. This imaging method uses precalculated spherical harmonic coefficient matrices to transform the visibilities to brightness maps by direct matrix multiplication. The under sampled image domain artefacts (dirty beam) were suppressed by the products of differing harmonic order brightness maps. From the images, elevation and azimuth angles of arrival were obtained. Due to the excellent phase tolerance of ICEBEAR new light was shed on the long standing low elevation angle problem. This led to the development of the proper phase reference vertical interferometry geometry, which allowed horizon pointing radar interferometers to unambiguously measure elevation angles near the horizon. Ultimately resulting in accurate elevation angles from zenith to horizon.

Acknowledgements

It is with immense gratitude that I thank my Supervisor, Dr. Glenn Hussey. His unwavering patience and words of encouragement guided me over the most insurmountable of hurdles.

I thank my wife, for her dutiful care and steadfast resolve. I would not have been able to focus on my labors without her.

I graciously thank Dr. Devin Huyghebaert whom I often referred to as my *step supervisor*. His stewardship and continued friendship is most appreciated.

Collectively I thank the welcoming and nurturing SuperDARN Canada community members: Dr. Kathryn McWilliams, Marci Detwiller, Kevin Krieger, Keith Kotyk, Bion Larson, Draven Galeschuk, Dr. Ashanti Maxworth, and Dr. Ashton Reimer.

I acknowledge the support of the Canadian Space Agency (CSA) [20SUGOICEB], the Canada Foundation for Innovation (CFI) John R. Evans Leaders Fund [32117] and the Province of Saskatchewan. Also, I acknowledge, the support of the Natural Science and Engineering Research Council (NSERC) and the programs: the International Space Mission Training Program supported by the Collaborative Research and Training Experience (CREATE) [479771-2016] program and the Discovery grants program [RGPIN-2019-19135]; and the Digital Research Alliance of Canada [RRG-FT2109].

To my future self, I hope all this effort paid off.

Contents

List of Tables

List of Figures

List of Abbreviations

ICEBEAR	Incoherent Continuous-wave E region Bistatic Experimental Auroral Radar
SDR	Software Defined Radio
CW	Continuous Wave
PRN	Pseudo-Random Noise
RF	Radio Frequency
DAC	Digital to Analog Converter
ADC	Analog to Digital Converter
GPS	Global Positioning System
PPS	Pulse Per Second
HPA	High Power Amplifier
NEC	Numerical Electromagnetic Code
BPF	Bandpass Filter
LPF	Lowpass Filter
LNA	Low Noise Amplifier
FPGA	Field Programmable Gate Array
IQ	In-phase and Quadrature
HDF5	Hierarchical Data Format version 5
GPU	Graphics Processing Unit
SNR	Signal to Noise Ratio
FFT	Fast Fourier Transform
RDI	Range Doppler Intensity
SAR	Synthetic Aperture Radar
ISAR	Inverse Synthetic Aperture Radar
VLBI	Very Long Baseline Interferometry
SAI	Synthesis Aperture Imaging
vCZ	van-Cittert Zernike
SWHT	Spherical Wave Harmonic Transform
pyIRIS	Python Interferometric Radar Imaging Suite
CDF	Common Data Format

List of Symbols

Chapter 2: ICEBEAR Background

λ	Radar wavelength
$\rho_{RF}, \Delta\rho_{RF}$	Total RF path length, and path length resolution
$\rho, \Delta\rho$	Range from source to receive, and range resolution
c	The speed of light in a vacuum $299,792,458$ m/s
τ_c	The time length of a chip in a sequence
$f, \Delta f$	Carrier frequency, and frequency bandwidth
$\nu, \Delta\nu$	Doppler shift, and Doppler resolution
s	A complex valued signal
A	Amplitude of an arbitrary signal
$u(t)$	The unit step function
ψ_n	The phase applied to the nth chip
Z_0	Freespace impedance 377 Ω
μ_0	The permeability of free space 12.566×10^{-7} H/m
ϵ_0	The permittivity of free space 8.854×10^{-12} F/m
R, L, G, C	Resistance, inductance, conductance, and capacitance
r, θ, ϕ	Spherical coordinates distance, azimuth, and elevation
P_{in}	Power input into an antenna
P_{rad}	Power radiated from an antenna
$U(\theta, \phi)$	Antenna power at range r in direction (θ, ϕ)
$D(\theta, \phi)$	Array or antenna directivity in direction (θ, ϕ)
$AF(\theta, \phi)$	Array factor in direction (θ, ϕ)
a_{mn}	Complex valued excitation of antenna m, n in an array
$\vec{d}_{mn}$	Baseline separation vector between antennas m and n
$\vec{k}$	Wave vector of incident wave
$G(\theta, \phi)$	Array or antenna gain in direction (θ, ϕ)
δ	Noise and unwanted signal
$m(\tau_d, \nu)$	Matched filter response at some time delay and Doppler shift
t, τ_d	Time, and time delay
$\chi(\tau_d, \nu)$	Ambiguity function response
S_m	The range-Doppler-intensity spectrum for some antenna m
V_{mn}	Visibility value for antenna pair m and n

Chapter 3: Array Design

$\eta, \eta\prime$	Arbitrary angle of arrival of some signal, and grazing angle
λ	Radar wavelength
ψ	The phase difference between two antennas separated by a distance
ψ'_{mn}	The phase difference including the $n2\pi$ ambiguity
d	The separation distance between two antennas
k_0	Wave number $k_0 = \frac{2\pi}{\lambda}$
ρ	Signal path lengths, either direct or reflected
R	Complex ground reflection coefficients
S	Complex voltage values with amplitude A and phase
Δ	Path length difference $\Delta = \rho_{d1} - \rho_{d2} \approx \rho_{r1} - \rho_{r2}$
C	Complex reflection function $C = \epsilon - \cos\eta\prime^2 - j60\sigma\lambda$
$P(\psi'_{mn}, \psi'_{ml})$	A phase measurement point in phase-phase space
w_q, e_q, d_q	Random-walk Annealing weighting, elasticity, and dampening terms

Chapter 4: Radar Imaging

τ_g	Geometric time delay between two separated antennas
c	The speed of light in vacuum
η	Arbitrary angle of arrival of some signal
Θ, Φ	Angular components of $\vec{k}$ on the imaging celestial sphere
$\vec{k}, k_0$	Wave vector and wavenumber $k_0 = \frac{2\pi}{\lambda}$
λ	Continuous-wave signal carrier wavelength
x, y, z	Antenna local Cartesian coordinates
u, v, w	Antenna baseline vector components, i.e. $u = \frac{x_i - x_j}{\lambda}$
r, θ, ϕ	Antenna baseline vector components in Spherical coordinates
$\vec{b}$	Antenna baseline $\vec{b} = (u, v, w)$ or $\vec{b} = (r, \theta, \phi)$
Y_{lm}	Spherical harmonic function with degree l and order m
J_l	Spherical Bessel function of the first kind with degree l
V_i	Visibility value of the i^{th} baseline
$\mathbf{B_l}$	Brightness map taken with l^{th} harmonic degree
$\mathbf{C_l}$	Coefficient SWHT matrix for the l^{th} harmonic degree
L, M	Direction cosines
$F(u, v), G(L, M)$	Visibility sampling function and its Fourier transform, the dirty beam

Chapter 5: Elevation Angles

ψ	The phase difference between two antennas separated by a distance
λ	Radar wavelength
$\vec{d}$	Antenna pair separation vector
$\vec{s}$	Direction vector of an incident wave
f	Carrier frequency
n	Index of refraction
N_e	Electron density in m^{-3}
D	Divergence factor of the glistening surface
R_c	Radius of curvature
R_E	Radius of the Earth in kilometers
r, θ, ϕ	Spherical coordinates
s_g, s_{rp}	Ground distance from the receiver to target and receiver to reflection point
ρ	Slant range from target to receiver in kilometers
ρ_{RF}	Total RF propagation path distance in kilometers
ρ_D	Distance between the transmitter and receiver arrays in kilometers
h	Altitude above the Earth's surface of some target in kilometers
η	Arbitrary angle of arrival of some signal
α	Elevation angle with respect to the tangent to antenna array plane
β	Elevation angle measured with respect to the constant phase reference chord g
Γ	Geocentral angle subtended between the receiver array, center of the Earth and target
g	Constant phase reference chord from receiver array to target Earth pierce point
ε	The angle between the transmitted signal and received signal
χ	An intermediary angle used in calculations
κ	The angle subtended by the target, receiver, and transmitter
$\hat{u}$	Unit vector

1 Introduction

The original Ionospheric Continuous-Wave E Region Bistatic Experimental Auroral Radar (ICEBEAR) was developed at the University of Saskatchewan by Huyghebaert et al. (2019). It was a radar instrument, operating at 49.5 MHz, that was designed to probe the auroral E region of the terrestrial ionosphere. First light was 7 December 2017, and it operated on a campaign basis, unchanged, until the summer of 2019. During the two-year operating period, the original ICEBEAR instrument collected high quality measurements, meeting its design goals. However, it was apparent that improvements to the receiving system could be made that would better leverage the modern Software Defined Radio (SDR) hardware. Starting in the summer 2019 a new non-uniform receiver antenna array was designed and constructed. This thesis details the design of that radar receiver antenna array and the complex novel processing method required to interpret the data collected by the new array.

The two primary functions of a radar are the detection and range estimation of targets (Nathanson et al., 1991). Additionally, most modern radars have secondary functions to measure angular locations and Doppler velocities of targets. A radar measures these quantities by emitting an electromagnetic wave and sensing a returned wave that has either been reflected or scattered off a target, this is called an echo. A radar is designed with respect to a specific set of targets so that it can best discriminate target echoes from background noise. Target characteristics, such as: spatial extent, scattering cross-section, velocity, lifetime, spatial orientation, sensitivity, and expected spatial locations, all inform the radar's design. Variables such as radar type (monostatic, multistatic, bistatic, pulsed, continuous-wave), geolocation, mobility, antenna array pattern, radio hardware, pulse length, encoding, and others are all used to tune a radar for specific targets. The original ICEBEAR instrument studied two broad classes of targets: the primary targets were auroral ionospheric E region plasma, and the secondary targets were meteor trails. The new design was required to maintain focus on these targets.

The E region forms the base for the large current system surrounding Earth, which is known as the magnetosphere (Kivelson & Russel, 1995). The terrestrial E region is the ionospheric plasma layer existing between 90 km and 130 km above the Earths surface (Kelly, 1989). The depositing of energetic particles into the E region creates plasma waves and instabilities. By their nature, E region instabilities are turbulent rapidly changing targets, sometimes changing significantly in mere seconds. Thus, E region radars must collect fine spatial data, rapidly, and continuously. Radar scattering from E Region plasma instabilities are generally classified into four types (Haldoupis, 1989). The typical Doppler spectra response of these four types are illustrated in Figure 1.1. Type I is characterized by narrow spectral width with a peak Doppler velocity around the ion-acoustic speed, C_s. Type II is characterized by a broad spectral width with a peak around zero Doppler velocity. Type III is characterized by a very narrow spectral width with Doppler velocities around $\frac{C_s}{2}$. Type IV is characterized by narrow spectral width with Doppler velocities around $2C_s$. Types I and II are observed at all latitudes, whereas Types III and IV are only observed at high latitudes. Observation of these four types requires the probing radar waveforms to be perpendicular or very close to perpendicular to the magnetic field of the Earth or geomagnetic field. For high latitude auroral and polar observations, this necessitates a radar with a low, close to the horizon, view.

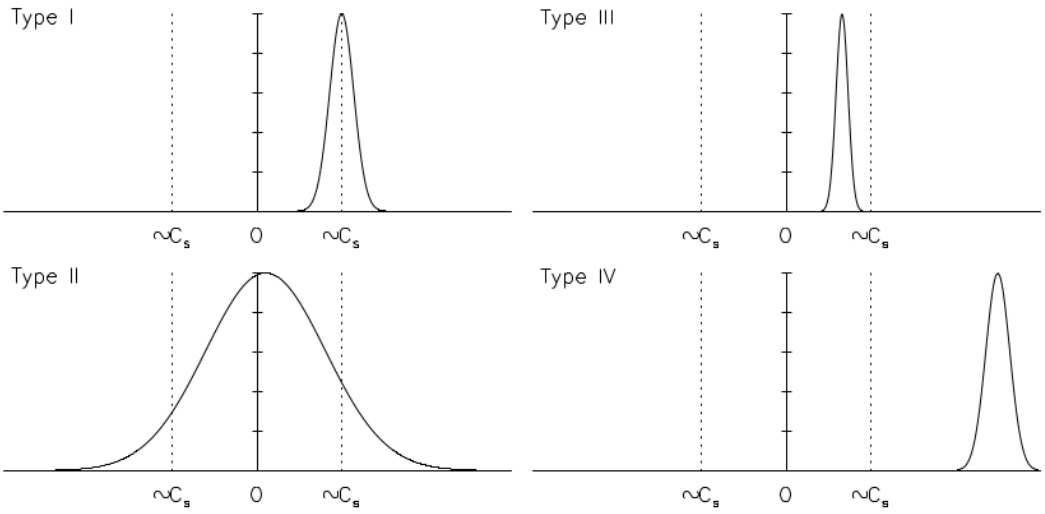

Figure 1.1: Idealized representation of the four types of commonly observed E region coherent radar spectra. C_s, the ion acoustic speed at E region altitudes is ≈ 360 m/s. The spectra have either positive or negative mean velocities, although only the positive velocities are illustrated (Hussey, 1995).

Meteors are detected by their trails and head echoes. As meteors enter the atmosphere, they begin to heat up due to friction. The denser atmosphere generates more friction, heating up the meteor until it typically vaporizes, leaving behind a trail of positive ions and negative electrons (McKinley, 1961). This ionization creates very long (kilometers long) thin (meters wide) parabolic trails along the meteor's trajectory. Scattering off these meteor trails are further classified as *over dense* and *under dense* depending on the density of electrons. The electron density transition point for classification is typically taken as 1×10^{14} m^{-3} (McKinley, 1961). Although the electron density is important for classification of meteor trails, it is the size of the meteor itself which determines the trail's characteristics. Typically, meteors about the size of a grain of sand generate under dense trails and larger meteors with a radius around 5 mm create over dense trails. Meteor trails typically exist on times scale from microseconds to very rarely several seconds. The altitude of these meteor trails is rather predictable. They follow a normal distribution starting at 110 km altitude, sharply peaking around 90 km to 95 km, and ending before 70 km. These altitudes vary slightly depending on season, solar cycle, time of day, and probing frequency, but are always within ± 5 km (McKinley, 1961). Meteor trails have a smaller Doppler shift range (± 150 m/s) than E region instabilities (± 1500 m/s) as the neutral atmosphere constrains them. As the E region instabilities were the primary target, a concession was made and a Doppler resolution corresponding to $\pm \approx 30$ m/s velocity was used, which is potentially too coarse for detailed meteor trail studies. Again, the short lifetime, size, and altitude of the meteor trail targets necessitates a radar with fine spatial resolution, and fine temporal resolution.

The original ICEBEAR instrument was designed to characterize E region instabilities and meteor trails at 100 ms temporal resolution and 1.5 km spatial resolution. This was achieved using a continuous-wave (CW) phase modulation technique. The CW signal necessitated physical isolation between the transmitting antenna array and receiving antenna array. Considering the auroral zone under investigation, the transmitter site was placed 240 km South-West of Saskatoon, SK near Prelate, SK and the receiver site was placed near Saskatoon, SK. This kept the receiver site, where data accumulates, near the operating institution, the University of Saskatchewan. The original ICEBEAR transmitter and receiver antenna arrays were both uniform linear arrays. This design was chosen for its reliability, simplicity, and the designer's past experiences (Huyghebaert, 2019). This design, however, limited the original ICEBEAR instrument to spatially locating targets in only range and azimuth, with some azimuthal ambiguity.

The altitude of E region coherent scatter types is an unanswered question. Recent work by

Chau and St-Maurice (2016) and St-Maurice and Chau (2016) have provided evidence and theoretical explanations for the altitude dependence of the characteristic E region scatter. They proposed that slow narrow (Type 3) radar echoes originate near the bottom of the E region, while fast narrow (Type 4) signatures originate near the top. Between these two extremes, the narrow ion acoustic speed signatures (Type 1) originate at ≈105–110 km altitudes, with the approximately zero Doppler broad signatures (Type 2) originating below this. Given the auroral latitude location of the original ICEBEAR instrument and its impressive performance, it was assessed that ICEBEAR could observe and potentially validate this theorized altitude dependence, provided the receiver antenna array was redesigned. This, along with the desire for meteor trail altitudes, motivated the construction of ICEBEAR-3D, which uses the original ICEBEAR infrastructure, but differs in receiver antenna array configuration and post-processing analysis to achieve 3-dimensional positioning of targets. Although differing physics is involved for E region scatter and meteor trail targets; for the purposes of this thesis, a detailed understanding of these targets is not required. They can be simply understood as radar targets with varying spatial extents, velocities, time scales, and elevations.

Three-dimensional radar target locating requires measurement of range, azimuth, and elevation of the returning echoes. Range is obtained by measuring the time of flight of the transmitted signal. Azimuth angles with the original ICEBEAR instrument are determined by comparing the phase differences between antennas in the linear array of received echoes. Phase differences can only be measured within a 2π boundary. Determining the phase is a convoluted problem when the 2π boundary is exceeded, but necessary to solve to correctly locate targets. The original ICEBEAR uniform linear receiving array caused targets to be incorrectly azimuthally located in some cases. Obtaining elevation angles is done in the same way as azimuth angles, but requires receiving antennas that are orthogonally positioned to an azimuth measuring array.

Measuring elevation angles with horizon pointing radars such as ICEBEAR is inherently more complex than non-horizon pointing radars, as the low elevation angle regime is plagued with multipath ground reflections (Barton, 1974; Kerr, 1951). Past E region observing radars like ICEBEAR that have attempted to acquire elevation angle measurements in the low elevation angle regime have seen inconclusive results (Ierkic et al., 1992; Sahr et al., 1991; Chisham et al., 2021). Often all measurements from 0° (horizon) to $\approx 30^\circ$ were rejected, or a single static constant phase calibration was used with spurious results. This was the case for Glanz (1971) and Clark (1977). Their meteor trail radar interferometers azimuth and

elevation angles were verified by a satellite beacon. They found that a 30° elevation angle cutoff was necessary, as results below 30° were unreliable. Typically, the explanation given for valid targets having unreliable elevation angle measurements at low elevation angles is the unreliability of phase measurements at low elevation angles due to hardware limitations and multipath interference. These somewhat erroneous calibrations and the hardware limitations of past radars created the seemingly unreliable phase measurements at low elevation angles, obfuscating the underlying cause of this long-standing low elevation angle problem. The later part of this thesis is dedicated to elucidating this problem and proposing a solution.

1.1 Objectives

The focus of this thesis was, initially, the redesign of the original ICEBEAR receiver antenna array from a uniform linear array to a new formation which would allow for richer and more accurate data products. The redesign of the receiver antenna array also necessitated the development of a different target acquisition and processing algorithm, which was appreciably more involved and complex than conventional ones. This led to the long standing low elevation issue. The final specific objectives of this thesis were:

1. To determine and implement a method to remove the effects of azimuth aliasing caused by the inherent 2π phase ambiguity.

2. To determine and implement a method of measuring the altitude of terrestrial auroral E region instabilities and meteor trails.

3. To elucidate and solve the underlying problem with elevation angles measured in the low elevation regime when using horizon pointing radar interferometers.

1.2 Outline

The work detailed in the body of this thesis has been published and peer reviewed (Lozinsky et al., 2022); it will be stated in each chapter when published content is used. This thesis is outlined as follows. Chapter 2 starts by describing a hypothetical signal as it propagates

through the ICEBEAR instrument. The signal begins its journey as a binary code sequence in the transmitter computer and ends as a standard low-level cross-correlation data product. Through the journey of this hypothetical signal, the necessary background information required for subsequent chapters is established. Chapter 3 discusses the objectives, constraints, and techniques applied to designing a non-uniform receiver antenna array. Chapter 4 delves into radar imaging and introduces the Suppressed Spherical Wave Harmonic Transform technique. This imaging technique, supported by the excellent phase resolution of ICEBEAR, elucidated the fundamental problem with elevation measurements where they appear much larger than expected in the low elevation regime. This problem is addressed in Chapter 5, and a list of reasonable explanations are purposed and subsequently rejected before a solution is given. The culmination of the array redesign, imaging, and elevation angle interpretation resulted in high quality temporal and spatial resolution ICEBEAR-3D data being collected during meteor showers and active E region periods. Results are presented in Chapter 6, and the veracity of ICEBEAR-3D is discussed. Chapter 7, concludes the work and presents the future work to be done.

2 ICEBEAR Background

The redesign of ICEBEAR to ICEBEAR-3D is receiver side focused. It is principally about the engineering design of radar interferometers. However, to understand how the receiver side of the original ICEBEAR instrument was redesigned for radar interferometry, understanding of the full ICEBEAR system is required. This chapter briefly explains the unchanged portions of ICEBEAR hardware, software, and standard operating mode, as these directly constrained the redesign of the receiver system.

It is convenient to discuss each component of the ICEBEAR radar as it transforms a hypothetical signal from a pseudo-random binary code sequence through to a received cross-correlated voltage data product also known as a visibility. A block diagram depicting the hypothetical signal's propagation path is shown in Figure 2.1. The figure is broken into three core blocks: transmission, reception, and processing. The transmission block encapsulates the process of signal generation, converting it into an analog signal, amplifying it, and transmitting. The handling of a received scattering echoes is described within the reception block. Here, the signal, which is greatly reduced in power since transmission, is amplified and filtered to isolate the signal from out of band noise. The now analog signal is converted into discrete digital voltage quantities and stored on disk. The processing block contains the steps where the signal is processed to create the ICEBEAR-3D Level 1 data product.

ICEBEAR was a bistatic continuous-wave radar that operated at 49.5 MHz (6.06 m wavelength, λ). A bistatic radar, as opposed to a monostatic radar, does not utilize a common antenna for transmission and reception. Typically, for a bistatic radar configuration, the transmitting and receiving antennas are separated by a considerable distance relative to the radar wavelength, as was the case for ICEBEAR. The hypothetical signal thus begins at the transmitter site located near Prelate, SK (50.893°, −109.403°), propagates through the radar hardware and is emitted into the auroral E region. In the E region scattering from plasma structures or meteor trails may occur generating echoes which propagate towards the receiver site located near Saskatoon, SK (52.243°, −106.450°). At the receiver site the signal

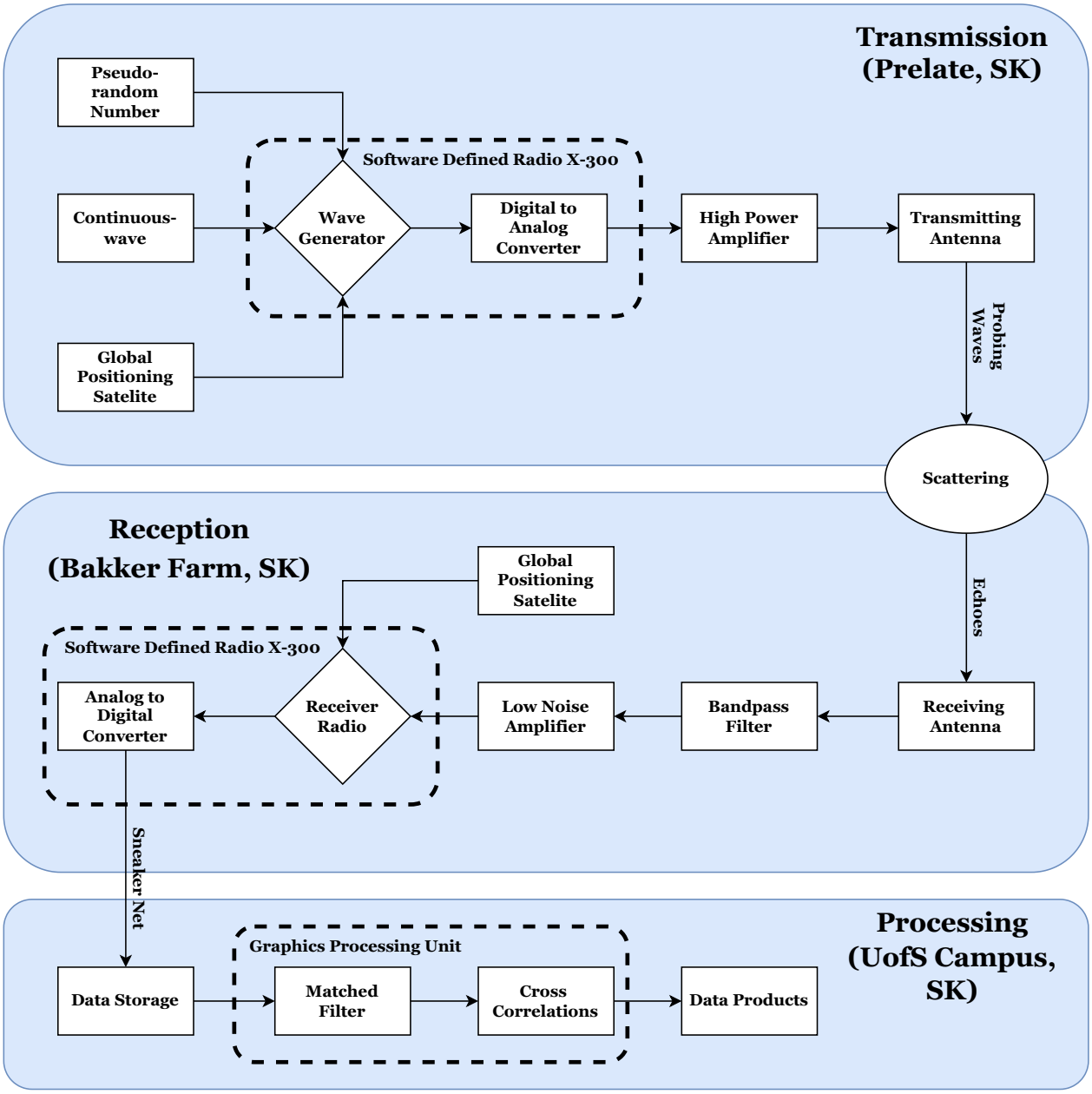

Figure 2.1: A simplified block diagram showing the ICEBEAR radar signal chain. The three blocks core blocks separate the signal chain by physical locations. Not shown are the many operation computers which control the radar and perform data processing.

is collected as a time series of voltage samples and stored on disk before being transported via *sneaker net* to the processing station at the University of Saskatchewan (Huyghebaert, 2019).

2.1 Transmission

The signal begins as a *noise-like* pseudo-random noise (PRN) binary sequence. Each bit of the PRN sequence is represented as a square pulse called a chip, see Figure 2.2. For

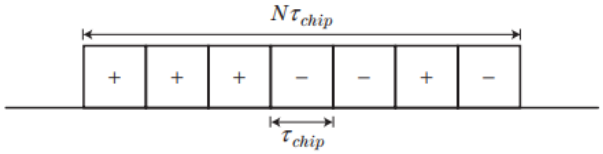

Figure 2.2: A binary coded waveform consisting of chips exhibiting two possible phase states (Richards et al., 2010).

ICEBEAR the length of each chip, τ_c, is 10 μs and the code sequence is made of $N = 10,000$ chips giving a total sequence length of 100 ms. The chip length and the speed of light in vacuum, c, defines the total radio frequency (RF) propagation path length resolution $\Delta\rho_{RF}$

$$\Delta\rho_{RF} = c\tau_c \tag{2.1}$$

for ICEBEAR this is 3.0 km. The total RF propagation path ρ_{RF} is the length of the path the signal takes from the transmitter to the scattering target and back to the receiver. The RF propagation path from the target to the receiver is the slant range ρ. For a monostatic radar the slant range is $\rho = \rho_{RF}/2$. For a bistatic radar this is more complicated and will be discussed in Chapter 5, but typically it is very close to the monostatic solution. Therefore, in general the range resolution, $\Delta\rho$, is 1.5 km. The shorter the chip length the finer the range resolution will be, however, the chip length also determines the signal's spread in frequency as it is inversely proportional to the bandwidth Δf

$$\Delta f = \frac{1}{\tau_c} \tag{2.2}$$

For ICEBEAR, this gives a 100 kHz bandwidth, which lies comfortably within the licensed 160 kHz band allowable by the radio license (Huyghebaert, 2019). The total code length, 100 ms, is also inversely proportional to the Doppler resolution $\Delta\nu$

$$\Delta\nu = \frac{1}{N\tau_c} \tag{2.3}$$

This gives a Doppler resolution of 10 Hz ($\approx$ 30 m/s) for ICEBEAR.

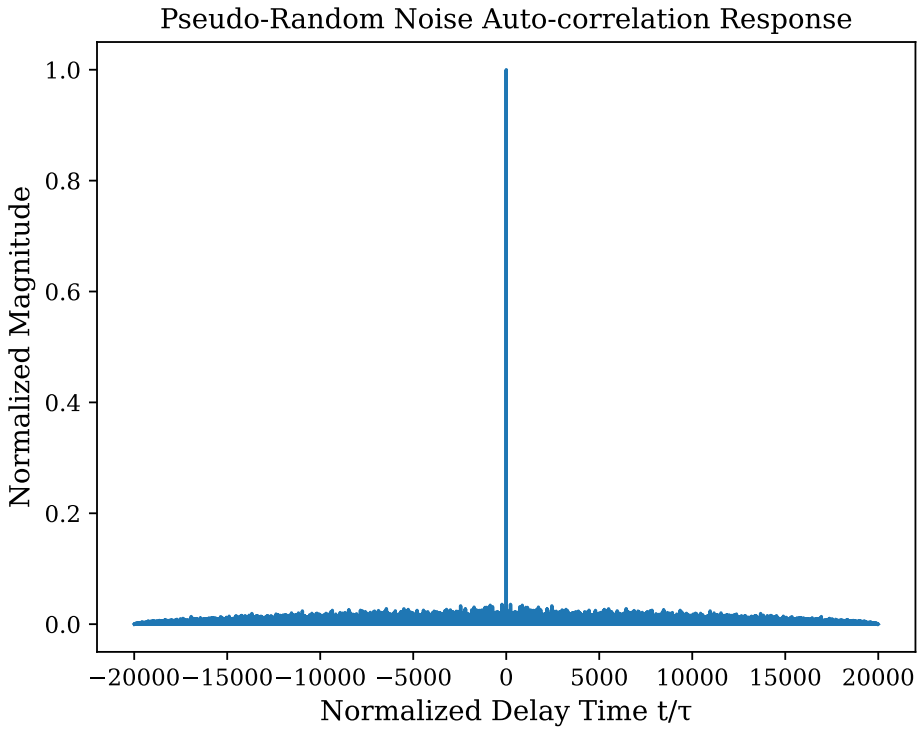

Figure 2.3: Normalized auto-correlation response of the standard ICEBEAR PRN code, showing a −28 dB side lobe suppression. Reproduced from Huyghebaert (2019)

Whereas the chip length relates to the total RF propagation path length resolution, and the code length determines the Doppler resolution, it is the PRN code itself which determines the ambiguity in the measured response. That is to say, it is the choice of bit sequence which determines ambiguity. A sufficient code requires a *thumbtack* like auto-correlation response; discretely peaked with side lobes suppressed and no aliasing (Richards et al., 2010). Codes that have perfect side lobe suppression are called Barker codes. Only seven known barker codes exist, the longest being 13 chips, which is not an adequate length for ICEBEAR, as the code length N is proportional to the energy in the waveform. The PRN code used is 10,000 chips long and is symmetric about the center chip to obtain adequate energy in the waveform (Huyghebaert, 2019). The auto-correlation of the ICEBEAR PRN code produces a peak centered about the normalized time delay center, with side lobes suppressed by $1/N$. Figure 2.3 shows the normalized auto-correlation of the code with side lobe suppression of −28 dB (Huyghebaert, 2019).

The Doppler resolution aliasing point is

$$\frac{1}{2}N\Delta\nu \tag{2.4}$$

and occurs at ±50 kHz. The total RF propagation path length resolution aliasing point is

$$N\Delta\rho \tag{2.5}$$

and occurs at 30,000 km. ICEBEAR targets of interest are expected to have velocities within ±1.5 km/s (±0.5 kHz), and have a total RF propagation distance less than 3,000 km due to aspect conditions, scatter altitude, line of sight, and power loss. Thus, no Doppler or RF propagation path length aliasing is expected to occur.

At this point, the hypothetical signal exists as a 10,000 chip binary signal. Within the transmitting computer, the code is re-sampled from 100 kHz (10,000 bits at 100 ms) to 800 kHz. This allows for an amplitude modulation to be applied which suppresses the side bands of the transmitted signal. The signal is then passed from the transmit computer to an Ettus Instruments X300 software defined radio (SDR) where it is phase-modulated with a 49.5 MHz carrier wave and converted from a purely digital signal to an analog one using a digital to analog converter (DAC). This phase modulation is called Binary Phase Shift Keying (BPSK). ICEBEAR uses global positioning satellites (GPS) for clock synchronization and disciplining of a 10 MHz pulse per-second (PPS) signal. This PPS conditions SDR to ensure that the chip lengths are not skewed and gives an accurate measure of transmit time, which is critical for time of flight measurements that determine range. The fully conditioned signal is then amplified by a custom three stage high-power amplifiers (HPA) designed by Huyghebaert (2019). The amplifier provides 57 dBm gain when operated at 49.5 MHz, and suppresses the second and third side lobe harmonics by at least 26 dB from peak signal power (Huyghebaert et al., 2019).

Now, the signal exists as a waveform which is ready to be transmitted. It is mathematically described by

$$s(t) = A\cos\left(2\pi ft + \psi_n[u(t - n\tau_c) - u(t - (n+1)\tau_c)]\right) \tag{2.6}$$

$$0 \leq t \leq \tau_c, \quad 0 \leq n \leq N-1$$

where A is the amplitude of the signal, $u(t)$ is the unit step function, ψ_n is the phase applied by the n^{th} chip which is either 0 or π for the biphase code used, and f is the carrier wave frequency at 49.5 MHz. As an example, Figure 2.4 shows a baseband signal and the same

baseband signal mixed with the carrier wave to produce the phase encoded waveform. This signal is then transmitted continuously through the transmitter site antenna array.

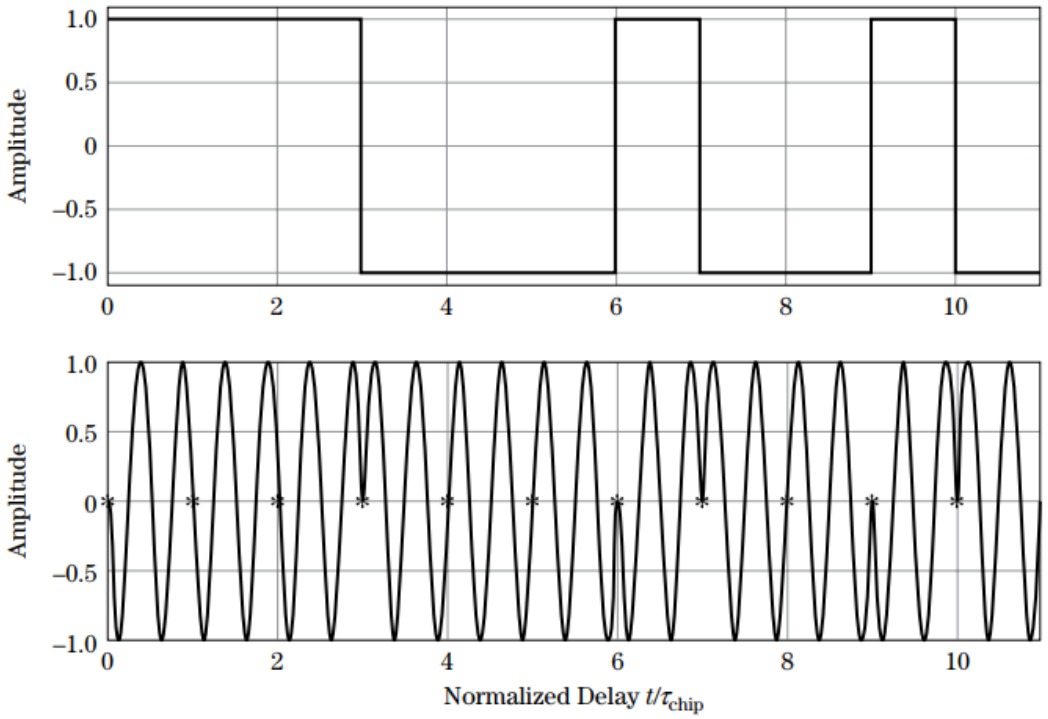

Figure 2.4: An example of a code sequence at baseband (top) and the same baseband signal mixed to produce a phase-modulated signal (bottom) (Richards et al., 2010).

2.2 Antennas and Arrays

An antenna is a transitional device which couples freespace to a transmission line, such as a coaxial cable, or waveguide (Balanis, 2016). One end of the antenna couples to freespace with an impedance of

$$Z_0 = \sqrt{\frac{\mu_0}{\epsilon_0}} = 377\ \Omega \tag{2.7}$$

where $\mu_0 = 12.566 \times 10^{-7}$ H/m is the permeability of free space, and $\epsilon_0 = 8.854 \times 10^{-12}$ F/m is the permittivity of free space. And, the other end to an electrical system, typically with a characteristic impedance of 50 Ω (Balanis, 2016). The characteristic impedance of a transmission line Z is the ratio between the voltage and current amplitudes of a single propagating

wave. The general expression for Z is given in terms of the telegrapher's equation

$$Z = \sqrt{\frac{R + i2\pi fL}{G + i2\pi fC}} \tag{2.8}$$

where f is the frequency, R is the resistance, L is the inductance, G is the conductance, and C is the capacitance (Balanis, 2016). When connecting RF components, impedance matching is required for maximum power transfer, as mismatches cause power to be reflected. Put simply, an antenna is a transducer which converts electrical currents moving in metal conductors into electromagnetic radio waves which propagate through space, or vice versa.

When an antenna transmits a radio wave, such as the hypothetical signal, the power is not radiated uniformly. The style and orientation of the antenna determines the polarization and directivity of the radiated power. Directivity $D(\theta, \phi)$ is the power density in a given direction (θ, ϕ) normalized by the average power density in all directions

$$D(\theta, \phi) = 4\pi r^2 \frac{U(\theta, \phi)}{P_{rad}} \tag{2.9}$$

where r, θ, ϕ are the spherical coordinates range, azimuth, and elevation, at which the directivity is evaluated, $U(\theta, \phi)$ is the power per unit solid angle at that range for some direction, P_{rad} is the total radiated power from the antenna. All antennas have a nonuniform directivity as true isotropic radiating antennas do not exist (the closest approximation is the Hertzian dipole). More complex antennas, such as the Yagi-Uda antennas used with ICEBEAR, are formations made of a collection of Hertzian dipoles. The simplest Yagi-Uda antenna is constructed from two components: a driven element which is essentially a powered Hertzian dipole, and a reflector placed behind the driven element that reflects radiated power from the driven element forward and in-phase. Additionally, one or more directing elements can be placed in front of the driven element to focus the forward power into a narrow beam. The size, spacing, and lengths of the elements all control the final directivity of the signal as well as determine the operating frequency band.

A combination of antennas can be used to create an array. Each antenna in the array contributes, much like each element in a Yagi-Uda antenna, to form a combined array directivity $D(\theta, \phi)_{array}$. Arrays allow for more power to be focused in a direction of interest without needing more powerful amplifiers. Array directivity is the combination of the individual antenna

directivity and the array factor $AF(\theta, \phi)$. The array directivity $D(\theta, \phi)_{array}$ is calculated by

$$D(\theta, \phi)_{array} = |AF(\theta, \phi)|^2 D(\theta, \phi) \tag{2.10}$$

where the array factor given by

$$AF(\theta, \phi) = \sum_{n=0}^{N} \sum_{m=n+1}^{M} a_{mn} \exp\left(-j\vec{k} \cdot \vec{d}_{mn}\right) \tag{2.11}$$

where $\vec{k}$ is the wave vector of an incident wave, $\vec{d}_{mn}$ is the antenna separation vector between the m^{th} and n^{th} antennas also known as a baseline, and a_{mn} is the complex excitation weighting the m^{th} and n^{th} antennas (Balanis, 2016). This formula is used to determine what proportion of the signal's power is radiated in any direction.

Gain is closely related to directivity, however, gain takes into account the efficiency of the antenna. The gain of an antenna in a certain direction is the ratio of the intensity in that direction to the intensity of an equally powered isotropic radiator. The power of the isotropic radiator in any direction is the total power accepted by the antenna divided by 4π. Gain does not take into account losses from impedance and polarization mismatches. Therefore, gain $G(\theta, \phi)$ is simply

$$G(\theta, \phi) = \frac{P_{rad}}{P_{in}} \times D(\theta, \phi) \tag{2.12}$$

where P_{rad} is the radiated power, P_{in} is the input power delivered to the antenna, and $D(\theta, \phi)$ is either the array or antenna directivity. Gain patterns are readily calculated using antenna simulation software. The Numerical Electromagnetic Code (NEC) is software which fully models the gain patterns of antennas and arrays. NEC versions 2.0 and 4.2 are freely available online, however they have limitations when it comes to properly simulating ground planes and segments which penetrate ground planes. The latest version, NEC-5, uses a new numerical method and solves these issues. Gain patterns of ICEBEAR, shown in Figures 2.5 to 2.8 were determined using NEC-5 (Lawrence Livermore National Laboratory, 2020).

The ICEBEAR transmitter array gain pattern is presented in Figure 2.5, it is formed of ten antennas 15 m above the ground uniformly spaced by 6 m (1λ). Each antenna is orientated to point 16° East of North. It was determined after construction that a large transmitter array is less critical for ICEBEAR due to the high sensitivity of the receiver electronics. Additionally, the operating radio license constrains maximum transmitting power, allowing at most for four antennas to operate at once. Thus, the transmitter only utilizes two of

the ten antennas separated by 18.17 m (3λ) to form a very simple array. Each of the two antennas excitation is synchronized to form a standard three lobe pattern with maximum gain direction (boresight) pointing 16° East of North and 6° above the ground, as indicated by the dashed black line in Figure 2.5. The top plot is the azimuth slice for boresight, while the bottom plot is the elevation slice.

By the reciprocity theorem, the above equations governing antenna gain for transmission are identical for reception (Balanis, 2016). The receiver antenna gain pattern is presented in Figure 2.6. The new receiver array utilizes aperture synthesis (discussed in Chapter 4) which combines antenna power entirely digitally, meaning excitation of each antenna is independent. So, it is the antenna gain pattern rather than the array gain pattern which is important. Each receiver antenna is a Cushcraft 612-B Super Boomer Yagi-Uda (see Figure 3.3) located 15 m above the ground and pointed 7° East of North. The dashed black line shows the boresight direction of 6° elevation and 7° East of North. The top plot is the azimuth slice for boresight, while the bottom plot is the elevation slice. The red shaded area shows the field of view where targets of interest under study are expected, this is also the radar imaging field of view (see Chapter 4).

Since ICEBEAR is a bistatic radar, it is the overlap of the receiver and transmitter gain patterns which ultimately determines the geographic location where gain is strongest. Figure 2.7 is the geographic gain transmitter and receiver patterns plotted on a WGS84 Earth model for a 110 km altitude shell. As ICEBEAR assumes that signal propagation is line of sight with very little bending due to refraction, the white areas are where a transmitted signal goes below the horizon. The top part of the figure is the transmitter pattern alone, and the bottom is the receiver pattern alone. The fanning of lobes of the transmitter view matches the azimuth slice of Figure 2.5, and likewise the wide beam of the receiver matches the azimuth slice of Figure 2.6. In each plot at lower latitudes, the lobes split into smaller lobes. These match the higher elevation lobes seen in their respective elevation slice plots.

The full overlapping geographic gain pattern is presented in Figure 2.8. This plot was calculated by creating a grid of latitude, longitude at 0.1° resolution for a constant 110 km altitude shell. For each grid point, the bearing and heading from the transmitter site to the grid point and the bearing and heading from the receiver site to the grid point was calculated on a WGS84 Earth model. Then, using the NEC-5 model, the bearings and headings were rotated with respect to their site's boresight. The NEC-5 models were then used as look-up tables to determine the gain in the direction of every point. The receiver and transmitter

gains were then summed for each point. Assuming there is no geographic area that produces more favorable conditions for echo power, it is apparent from Figure 2.8 where targets would be best detected. Of course, E region scatter has a spatial distribution due to its field-aligned scattering nature, which means there will be a power bias due to the magnetic field of the Earth. Meteor trails, however, would be expected to more closely follow Figure 2.8 as they are uniformly distributed in the geographic region. Provided a suitable scattering target exists to produce an echo, the brightest regions are where the signal will *close the link* between the transmitter antenna array and receiver antennas.

2.3 Reception

After scattering the hypothetical signal is returned as an echo to the receiver antenna array where it is transduced by the receiving antennas and passed through a bandpass filter (BPF) to remove frequencies outside the radar band. By this stage the signal is at a considerably low power, so it is passed through two low noise amplifiers (LNA) adding 56 dB of gain. The analog signal is then passed into the X300 SDR and several steps are handled digitally by its field programmable gate array (FPGA). Each X300 SDR has two separate receiver channels which are connected to separate receiver antenna paths. The SDR samples the signals at 200 Msps with its dual analog to digital converter (ADC), converting the analog signal to digital in-phase and quadrature (IQ) voltage samples. Again, the X300 SDRs are time synchronized and 10 MHz pulse per second disciplined via GPS. The digital signal is digitally mixed with the carrier frequency to obtain the baseband signal, and then lowpass filtered (LPF) to remove artefacts due to sample aliasing and mixing. The IQ samples are then decimated to a data rate of 200 kHz before being passed from the X300 SDR to the receiving site computer. ICEBEAR generates 8 MB/s (28.8 GB/day) of raw IQ voltage sample data during standard operation. This data is stored on hard disk using the Hierarchical Data Format version 5 (HDF5) data format. These HDF5 files are referred to as Level 0 data. The hard drives with Level 0 HDF5 files are physically collected and transferred (*sneaker net*) to a processing computer equipped with a graphics processing unit (GPU) located at the University of Saskatchewan.

System specifications for the signal chain from transmission through reception are summarized in Table 2.1.

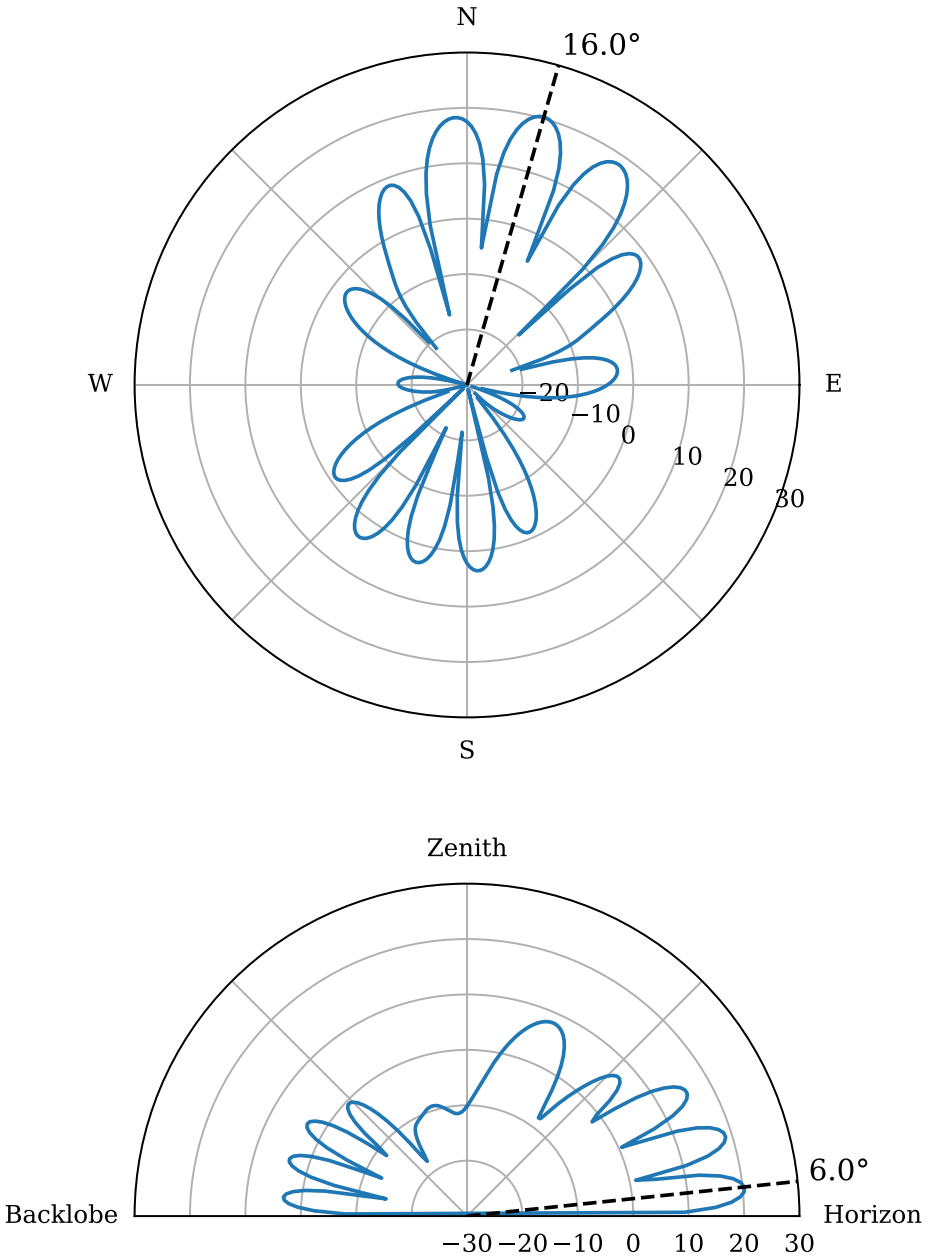

Figure 2.5: Normalized transmitter array gain pattern in dB. (Top) Cross-section of the horizontal gain pattern at the elevation of the maximum vertical gain. (Bottom) Cross-section of the vertical gain pattern at the azimuth of the maximum horizontal gain. The dashed black lines indicate the direction of maximum gain (boresight: 6° elevation, 16° East of North). The pattern is generated with NEC-5 software (Lawrence Livermore National Laboratory, 2020).

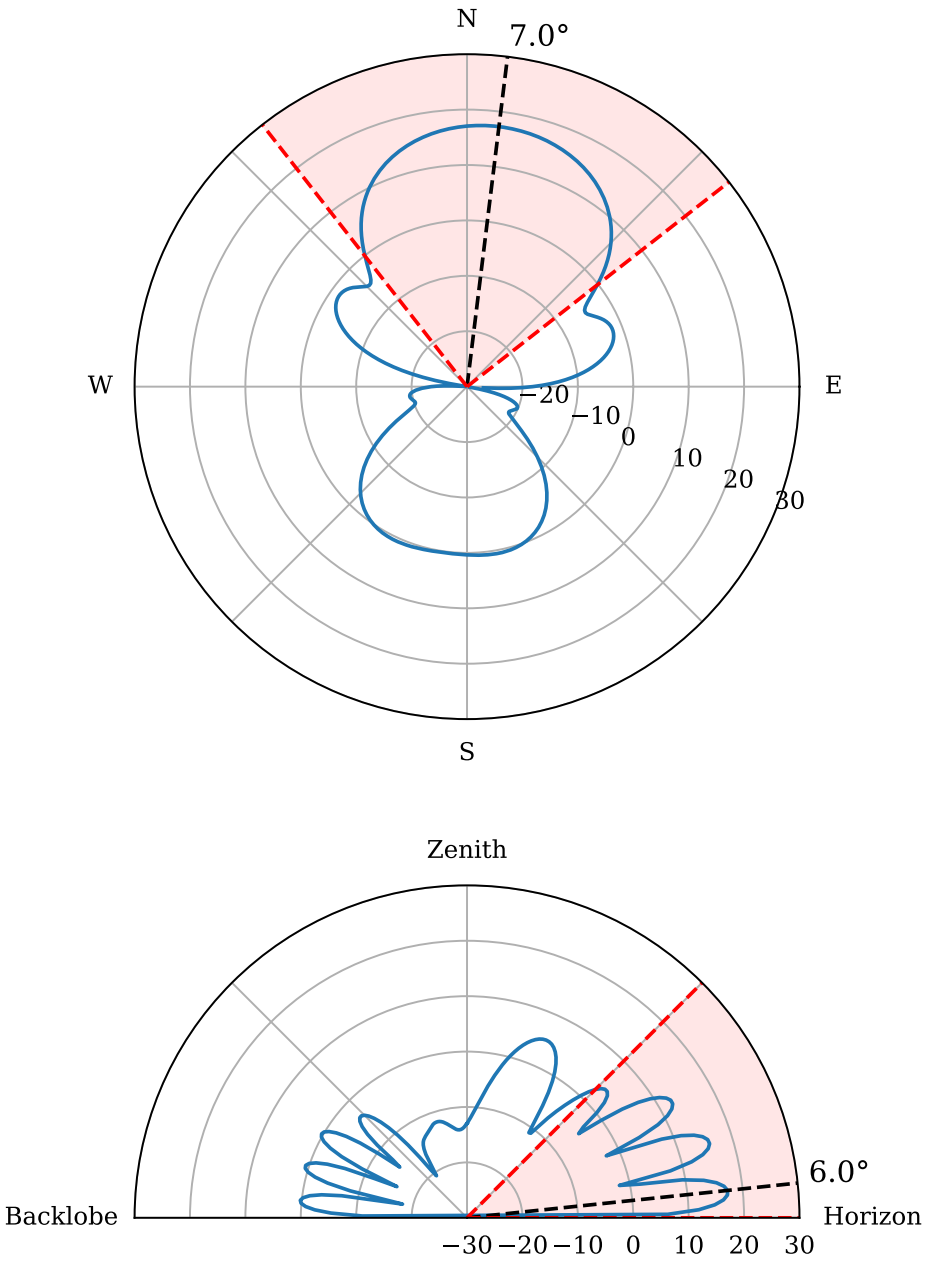

Figure 2.6: Normalized receiver antenna gain pattern in dB. (Top) Cross-section of the horizontal gain pattern at the elevation of the maximum vertical gain. (Bottom) Cross-section of the vertical gain pattern at the azimuth of the maximum horizontal gain. The dashed black lines indicate the direction of maximum gain (boresight: 6° elevation, 7° East of North). The red shaded area shows the imaging field of view. The pattern is generated with NEC-5 software (Lawrence Livermore National Laboratory, 2020).

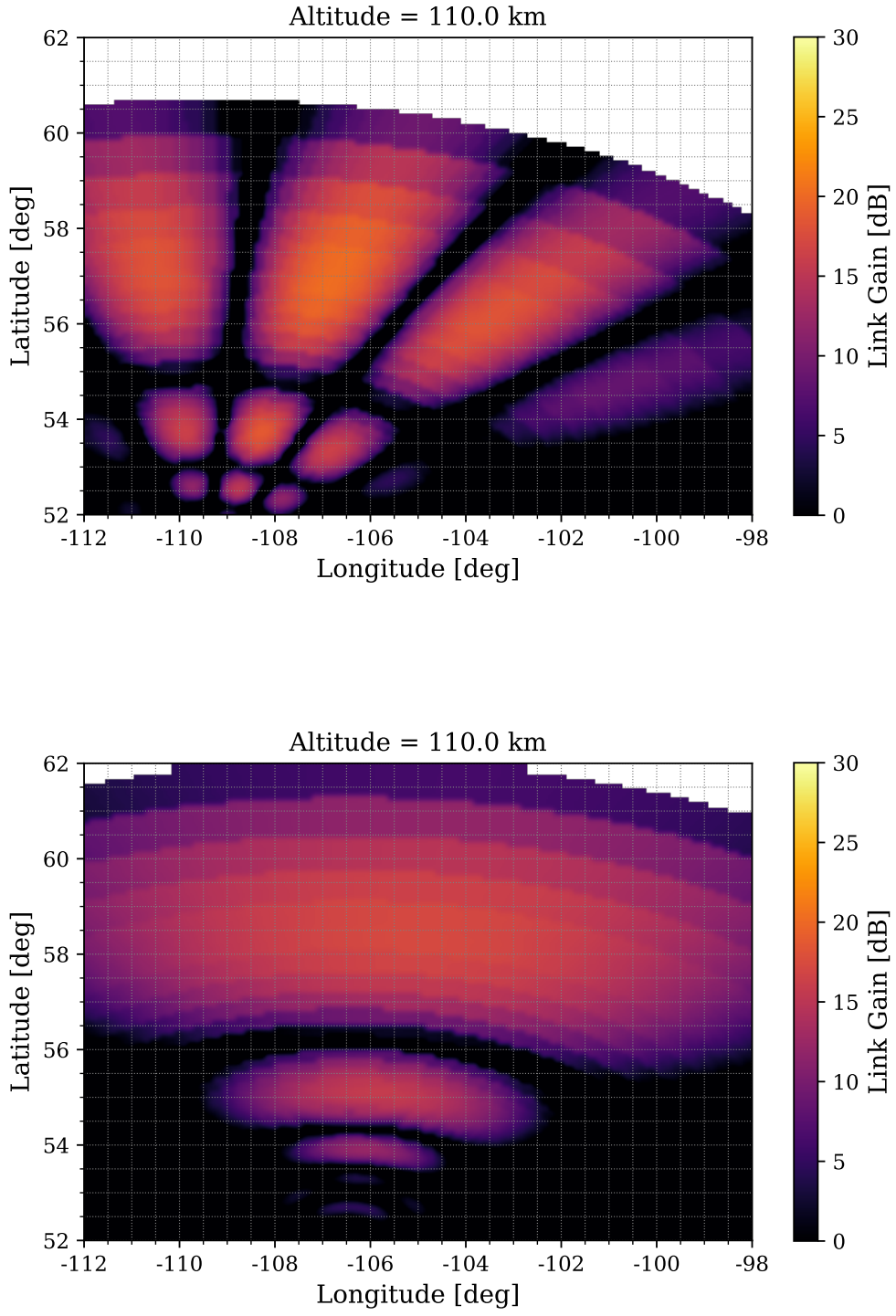

Figure 2.7: (Top) Transmitter array gain pattern, and (Bottom) Receiver antenna gain pattern at 110 km altitude on a WGS84 Earth model. The white area is where the Earth occludes a line of sight link.

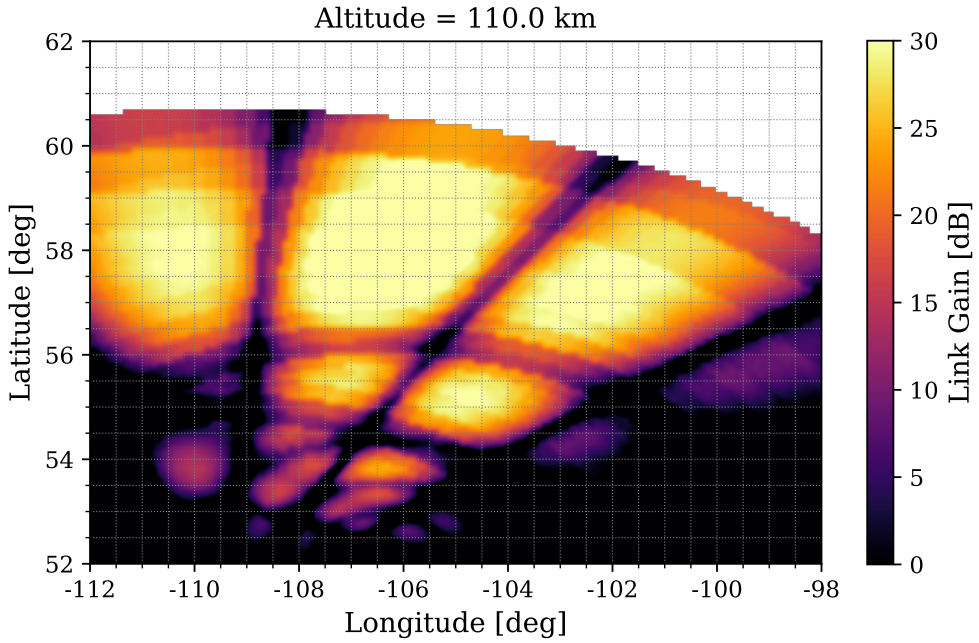

Figure 2.8: Superposition of the transmitter array gain pattern and receiver antenna gain pattern in dB. The link is modeled on a WGS84 Earth model at a constant 110 km altitude. The white area is the region where the Earth occludes a direct line of sight link. The regions show where the bistatic radar has sufficient gain to detect targets.

Table 2.1: System specifications (Huyghebaert, 2019).

Specification @ 49.5 Mhz	**Value**
Receiver location	(52.243°, −106.450°)
Receiver pointing direction	7°East of North
Transmitter location	(50.893°, −109.403°)
Transmitter pointing direction	16°East of North
Peak transmitter output power	300 W
Transmitter array type	Linear (1λ spacing)
Receiver array type	Non-uniform planar
Modulation type	Binary Phase Shift Keying
Chip length	10 μs
Code length	10,000
Range resolution	1.5 km
Range aliasing	30,000 km
Doppler resolution	10 Hz
Doppler aliasing	± 50 kHz
Sample size	32-bit IQ
Data rate for 10 receivers	8 MB/s

2.4 Processing

The hypothetical signal now exists as digital IQ voltage samples, but it remains mixed with noise and is indiscernible. The PRN phase encoded signal needs to be recovered from amongst the noise. This is achieved through matched filtering, which is a form of coherent integration that finds the Doppler shifted received signal $s_{rx}(t)$ amidst the noise by cross-correlating it with the transmitted $s_{tx}(t)$ signal (Huyghebaert, 2019). The cross-correlation will peak at some time delay which corresponds to the time of flight of the transmitted signal, which in turn is related to the target range. Specifically, a matched filter is a special case of linear time-invariant filters where the signal-to-noise ratio (SNR) is maximized for some time delay. The matched filter response m is described by the equation (Hysell, 2018),

$$m(\tau_d, \nu) = \int_{-\infty}^{\infty} s_{rx}(t) s_{tx}^*(t - \tau_d) e^{j2\pi\nu t} dt + \delta \tag{2.13}$$

where τ_d is the time delay, t is time, ν is the Doppler frequency shift at which filtering occurs, $s_{rx}(t)$ is the received baseband signal at time t, $s_{tx}^*(t - \tau_d)$ is the conjugate of the transmitted signal at offset time τ_d, and δ represents the combination of sky noise, system noise and self clutter. The matched filter output $m(\tau_d, \nu)$ will be maximum, where τ_d and ν

corresponds to the scatter target's range and Doppler shift. A true matched filter requires the exact transmitted signal; ICEBEAR does not record the actual transmitted signal, which does differ from the expected signal, as radio electronics are not perfect. Also, a measure of the noise floor is required to remove δ, this is not done with ICEBEAR, instead it is assumed that the mean power of the received signal is equal to the noise power (Huyghebaert, 2019). These two caveats mean ICEBEAR processing does not use a perfect matched filter, but is practically close.

Notice that for $s_{rx} = s_{tx}$, that $\int_{-\infty}^{\infty} s(t)s^*(t-\tau_d)e^{j2\pi\nu t}dt$ is a Fourier transform with respect to ν. Thus, Equation 2.13 can be rewritten as

$$\mathcal{X}(\tau_d, \nu) = \int_{-\infty}^{\infty} \chi(\tau_d, t)e^{j2\pi\nu t}dt + \delta \tag{2.14}$$

where $\chi(\tau_d, t) = s(t)s^*(t-\tau_d)$ and $m(\tau_d, \nu) = \mathcal{X}(\tau_d, \nu) + \delta$. By taking the square $|\mathcal{X}(\tau_d, \nu)|^2$ and assuming the target is at $\tau_d = 0$, $\nu = 0$ this provides the range-Doppler ambiguity function (Hysell, 2018)

$$|\mathcal{X}(\tau_d, \nu)|^2 = \left|\int_{-\infty}^{\infty} s(t)s^*(t-\tau_d)e^{j2\pi\nu t}dt\right|^2 \tag{2.15}$$

Using the ICEBEAR PRN code as the signal, Figure 2.9 shows the ICEBEAR ambiguity function. The response is a zoomed in view of the center, it shows a 1.5 km range and 10 Hz Doppler resolution as expected.

Although Equation 2.13 is continuous, the real world ICEBEAR radar samples discretely. Thus, the matched filter processing which decodes the PRN from the received signal is done differently. First, the signals are decimated in software to 1 kHz to make Fast Fourier Transforms (FFT) quicker when they are later calculated. Then an array of received complex voltage samples $s_{rx}[N+x]$ is taken with length $N+x$, where the [ ] brackets denote indices of the array. For ICEBEAR-3D, $x = 2000$ and is the number of range bins to calculate, and $N = 10,000$ is again the number of chips. Also, take the conjugate of the transmitted signal to get $s^*_{tx}[N]$ with length $N = 10,000$. Then perform the outer product $s_{rx}[N+x]s^*_{tx}[N]$. This produces the decoded voltages as a function of the effective range and time; the resulting matrix has the shape of total RF path length bins by time. An FFT is then calculated across each RF total RF path length row, giving the range-Doppler-intensity (RDI) spectrum $\mathbf{S}[\rho_{RF}, \nu]$, which has the shape of total RF path length bins (2000) by Doppler bins (100), for a total of 200,000 bins every 1 s. This is then done for each antenna for every 100 ms scan. Ten scans are then averaged together to produce a 1 s time resolution RDI spectrum.

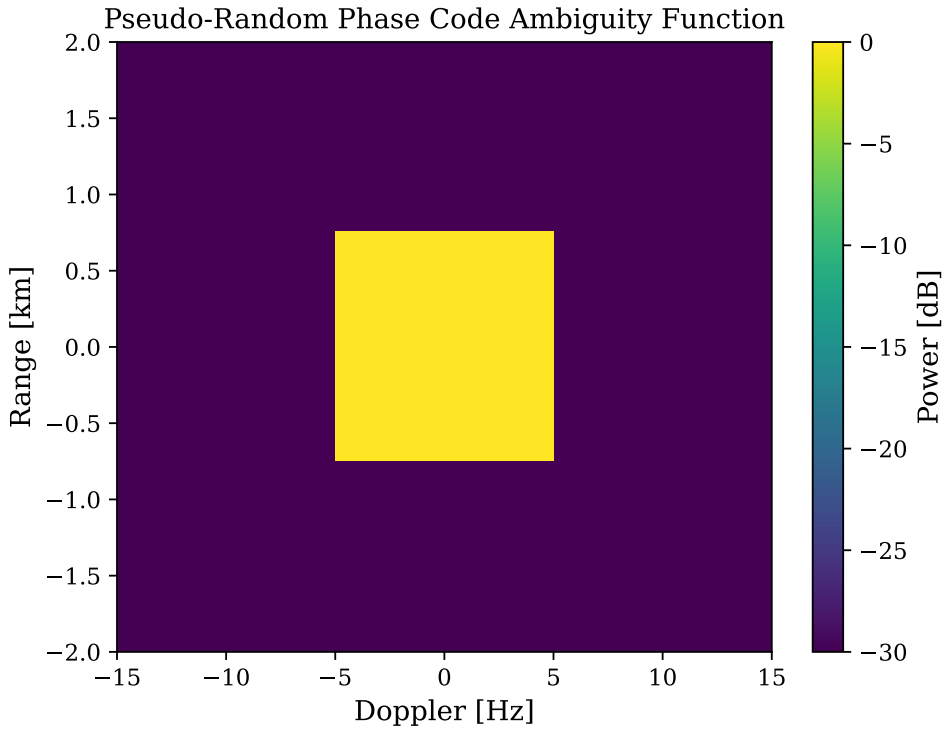

Figure 2.9: A zoomed in view showing the 28 dB isolation between the peak power and the self-clutter. Illustrating the thumbtack response in rang-Doppler space (Huyghebaert, 2019).

The RDI spectrums are then cross-correlated between each antenna and auto-correlated at each 1 s time cadence, generating the cross-spectra and spectra, respectively. The cross-spectra and spectra are also called — visibilities — and form the fundamental value of the Level 1 ICEBEAR data product. Visibility values are the final form of the hypothetical signal, and for a 1 s period is calculated by

$$\mathbf{V}_{mn}[\rho_{RF}, \nu] = \mathbf{S}_m[\rho_{RF}, \nu]\mathbf{S}_n^*[\rho_{RF}, \nu] \tag{2.16}$$

where the visibility quantity for the m^{th} and n^{th} antenna pair at RF path length ρ_{RF} and Doppler shift ν is $V_{mn}[\rho_{RF}, \nu]$. The resulting visibilities are complex values that hold the time difference of arrival of the received signal for each antenna pair, which are used to compute angles of arrival and coherence lengths. Classically, ICEBEAR instrument's uniform linear receiver antenna array this was done using the basic interferometry equation, discussed in Chapter 3. The design of the ICEBEAR-3D receiver antenna array is discussed next. This is where ICEBEAR and ICEBEAR-3D become significantly different.

3 Array Design

Sections 3.1, 3.2, and 3.3 of this chapter contains in part works directly from my contributions in Lozinsky et al. (2022).[1]

Receiver array design is considered more of an art than a science amongst experts. The explosive nature of computing possible receiver array configurations for a given specification being functionally impossible, the designer often needs to rely upon their best judgement to narrow the design scope. The design of sparse receiver arrays is inherently similar to the famous *travelling salesman* problem where instead of minimizing the distance travelled by choosing an optimal route, the sparse receiver array designer is optimizing where the cities (or antennas in this case) are placed (Keto, 1997). There are no known analytical solution, only heuristic approaches. This chapter describes the procedure used to design the ICEBEAR-3D receiver antenna array. The discussion begins by outlining the design considerations for the receiver antenna array — strictly the requirements needed to upgrade the ICEBEAR system as outlined in Chapter 2 to overcome its limitation. Namely, the critical design function, obtaining high resolution elevation angles of targets at 49.5 MHz using low viewing angles, but also removing angle of arrival aliasing, and increasing the instrument's phase error tolerance. After the design considerations are laid out, the design methodology, which is a combination of the Jacobs-Ralston phase error minimization technique and a custom *Random-walk Annealing* stochastic optimization algorithm, is explained. Using the described methodology, a novel sparse receiver antenna array design is given for aperture synthesis imaging (see Chapter 4).

[1] Lozinsky, A., Hussey, G., McWilliams, K., Huyghebaert, D., and Galeschuk, D. (2022). ICEBEAR-3D: A Low Elevation Imaging Radar Using a Non-Uniform Coplanar Receiver Array for E Region Observations, *Radio Science*, 57(3). DOI: 10.1029/2021RS007358

3.1 Design Considerations

The receiver antenna array redesign is governed by several considerations, which are drawn from the limitations of the original ICEBEAR uniform linear receiver antenna array. Each of the design objectives and constraints applied to the ICEBEAR-3D receiver antenna array reconfiguration are discussed.

3.1.1 Elevation Angles of Arrival

The angle of arrival η of a signal of wavelength λ in the far field can be determined by measuring the phase difference ψ between two isotropic antennas separated by some distance d (Thompson, Moran, & Swenson, 2001). The basic geometry for this elementary interferometer is shown in Figure 4.1 and is analogous to the Young's two-slit interferometer geometry. The details of basic radio interferometry are given in detail in Section 4.1, but the basic governing equation is also given here for convenience

$$\psi = \frac{2\pi}{\lambda} d \cos \eta \tag{3.1}$$

Angles of arrival measured with such an interferometer are ambiguous if the separation distance d is greater than $\lambda/2$. This due to the inherent $n2\pi$ ambiguity that comes with measuring phase using real world instruments. The equation becomes

$$\psi = \frac{2\pi}{\lambda} d \cos \eta + n2\pi \tag{3.2}$$

where the $n2\pi$ ambiguity is responsible for aliasing when determining the angle of arrival η. All ambiguous angles of arrival derived using this equation will lie in the plane described by the antenna separation vector or baseline $\vec{d}$. For any collinear array, such as the original uniform linear ICEBEAR receiver array, this restricts the angle of arrival measurements to one dimension projected about the collinear axis. ICEBEAR-3D required non-collinear baselines.

The direct solution to obtaining elevation angles of arrival is to construct a tall tower and place antennas at various heights. However, elevation angles determined in this way are subject to increased complexity due to multipath effects differing greatly for antennas at

different heights on the tower. This complexity is the result of the cross terms in the cross-correlation between two antennas no longer being minimal, as the reflection path lengths cannot be considered equal. The effects of direct and reflected signal paths on the cross-correlation is a purely geometric relationship. Given a horizontally polarized plane wave arriving at two antennas with baseline $\vec{d}$, then the complex voltages are

$$S_1 = Ae^{j(k_0\rho_{d1})} + AR_1e^{j(k_0\rho_{r1}+\pi)} \tag{3.3}$$

$$S_2 = Ae^{j(k_0\rho_{d2})} + AR_2e^{j(k_0\rho_{r2}+\pi)}$$

where ρ_{d1} and ρ_{d2} are the direct signal path lengths to antenna 1 and 2, likewise ρ_{r1} and ρ_{r2} are the reflected signal path lengths, R_1 and R_2 and the complex ground reflection coefficients for the signal paths, A is the signal amplitude, and $k_0 = 2\pi/\lambda$ is the wavenumber. The additional π phase shift occurs due to the refection of a horizontally polarized wave (Boithias, 1987). The cross-correlation is

$$S_1S_2^* = (Ae^{j(k_0\rho_{d1})} + AR_1e^{j(k_0\rho_{r1}+\pi)})(Ae^{-j(k_0\rho_{d2})} + AR_2e^{-j(k_0\rho_{r2}+\pi)}) \tag{3.4}$$

$$S_1S_2^* = |A|^2(e^{j(k_0[\rho_{d1}-\rho_{d2}])} + R_2e^{j(k_0[\rho_{d1}-\rho_{r2}]-\pi)} + R_1e^{j(k_0[\rho_{r1}-\rho_{d2}]+\pi)} + R_1R_2e^{j(k_0[\rho_{r1}-\rho_{r2}])})$$

In the case where the towers are all of equal height and the ground reflection conditions can be considered similar at the reflection points then the following assumptions can be made,

$$\rho_{d1} - \rho_{d2} \approx \rho_{r1} - \rho_{r2} = \Delta \tag{3.5}$$

$$\rho_{d1} - \rho_{r1} \approx \rho_{d2} - \rho_{r2}$$

$$R_1 \approx R_2 = R$$

Then equation 3.4 simplifies to,

$$S_1S_2^* = |A|^2(e^{jk_0\Delta} + R(e^{j(k_0[\rho_{d1}-\rho_{r2}]-\pi)} + e^{j(k_0[\rho_{r1}-\rho_{d2}]+\pi)}) + R^2e^{jk_0\Delta})$$

$$S_1S_2^* = |A|^2e^{jk_0\Delta}(1+R^2) + |A|^2R(e^{j(k_0[\rho_{d1}-\rho_{r2}]-\pi)} + e^{j(k_0[\rho_{r1}-\rho_{d2}]+\pi)}) \tag{3.6}$$

For low elevation angles of arrival the reflection angle of incidence $\eta\prime$, also known as grazing angle, is very small. The reflection coefficient R is related to grazing angle by,

$$R = \frac{\sin\eta\prime - \sqrt{C}}{\sin\eta\prime + \sqrt{C}} \tag{3.7}$$

where C is a complex function dependent on polarization and frequency (Boithias, 1987). For ICEBEAR which is horizontally polarized C is,

$$C = \epsilon - \cos\eta\prime^2 - j60\sigma\lambda \tag{3.8}$$

where σ is the conductivity and ϵ is the relative permittivity (Boithias, 1987). In most cases on Earth, ϵ and σ depend almost entirely on the surface humidity. For all practical surface conditions as $\eta\prime$ becomes very small the magnitude of R approaches -1 (Boithias, 1987). Since ICEBEAR operates almost entirely in the low elevation regime (horizon to 20°) Equations 3.6 is simplified,

$$S_1 S_2^* = 2|A|^2 e^{jk_0\Delta} - |A|^2(e^{j(k_0[\rho_{d1}-\rho_{r2}]-\pi)} + e^{j(k_0[\rho_{r1}-\rho_{d2}]+\pi)}) \tag{3.9}$$

Under these assumptions, the remaining cross terms can be neglected as they contribute very little, often on the order of system noise, resulting in

$$S_1 S_2^* = 2|A|^2 e^{jk_0\Delta} \tag{3.10}$$

Thus, Equation 3.10 is equivalent to the result of the cross-correlation between two antennas in freespace except with double the power due to the exploitation of the reflected multipath signal. This effect is known as a *sea interferometer* or *Lloyd's mirror* where a pseudo baseline is generated via the antenna and a virtual image antenna below the reflection plane. However, hidden here is the phase portion of $R = -1 = 1e^{j\pi}$ which becomes π at small grazing angles, which again inverts the reflected signals phase generating an interferometer fringe pattern 180° out of phase from typical interferometers. Antennas placed at different heights will not benefit from this effect equally, complicating the acquisition of elevation angles at low elevation angles. Additionally, a tower sufficiently tall enough to have adequately long baselines for Very High Frequency (VHF) radars are prohibitively expensive to construct and maintain.

The simplest method to resolve elevation angles is to construct a set of baselines in a plane across flat ground with similar ground conditions in all directions. This method is subject to uncertainties inherent to planar radars, which primarily is having no height displaced antennas to resolve the above/below ground ambiguity. However, it does benefit from the fact that if the maximum baseline is much less than the radius of the Earth and the wavelength is larger than small scale topological changes, there is no significant ground reflection multipath difference between each antenna. In order to acquire elevation angles of arrival,

the ICEBEAR-3D design needed to be a planar array with baselines for elevation placed North-South along the expected angle of arrival direction.

3.1.2 Removal of Angle of Arrival Ambiguities

The determination of angles of arrival using Equation 3.2 requires the correct selection of n to resolve the ambiguity; otherwise, many indeterminate angles of arrival solutions exist. The top plot of Figure 3.1 demonstrates the fringe patterns for a 1λ and 2λ baseline interferometer with the expected angle of arrival at 50°. There exists many ambiguous solutions due to the $n2\pi$ ambiguity. Combining the angle of arrival solutions generated from multiple unique baselines eliminates potential solutions; repeated baselines only reinforce the various solutions. The combination of enough unique baselines will unambiguously resolve the angle of arrival, except for the case where the unique baselines are spatial multiples of one another. In this case, there will always be an angle of arrival solutions at spatially harmonic intervals. These other solutions can then be incorrectly selected, resulting in angle of arrival aliasing. The middle and bottom plots of Figure 3.1 are the normalized summation for a 10 baseline fringe or interference pattern, where the expected angle of arrival solution is 50°. The middle plot corresponds to a uniformly 1λ spaced antenna array with 10 antennas. The solution is ambiguous as the baselines are spatially harmonic, with only 9 unique baselines and 36 redundant (exactly the same) baselines. However, the maximum amount of unique baselines given n antennas is $n(n-1)/2$. The bottom figure uses all unique baselines at non-integer spacing to eliminate spatially harmonic solutions from emerging. In the bottom plot only one solution is found.

The original ICEBEAR receiver antenna array had angle of arrival aliasing as it was limited by its uniformly 1λ spaced 10 antennas linear array. The uniform spacing limited the number of unique baselines possible to 9. In order to remove angle of arrival aliasing, the ICEBEAR-3D design required the condition that all baselines are unique to maximize the available spatial information and that not all baselines be spatial multiples of one another. This is most easily achieved by selecting non-integer λ spaced baselines.

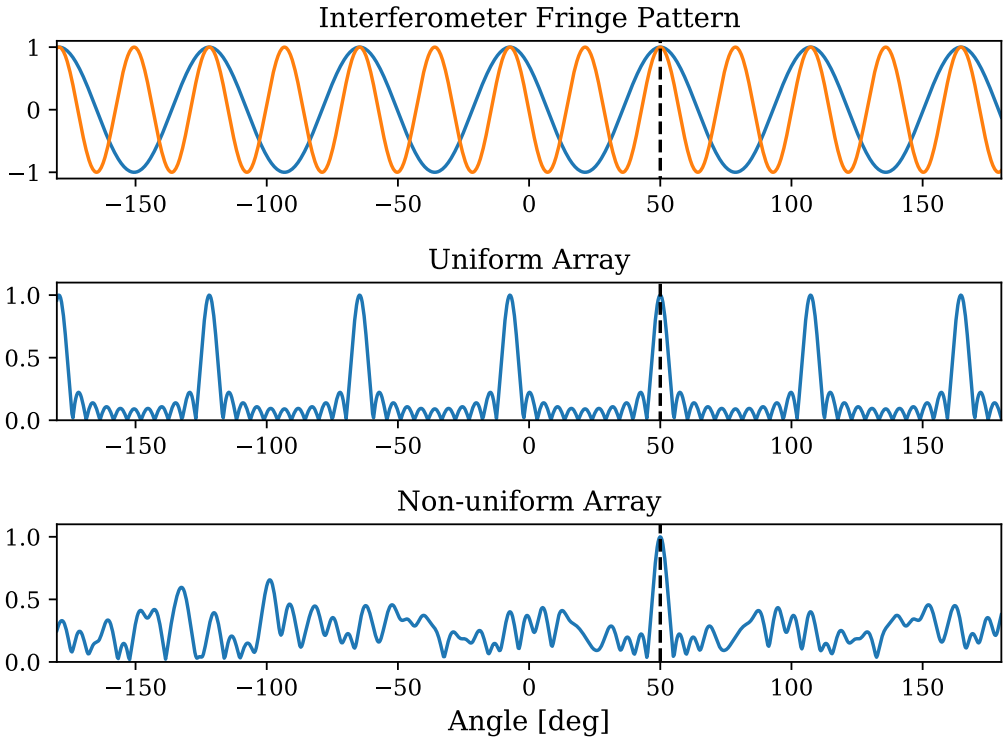

Figure 3.1: Interferometer fringe patterns for various baselines of a target with a 50° angle of arrival. (Top) The fringe patterns for a 1λ and 2λ baseline interferometer. The middle and bottom plot shows a 10 baseline interference pattern. (Middle) The interference pattern from a uniformly spaced antenna array giving ambiguous angle of arrival solutions. (Bottom) The interference pattern from a non-integer non-uniformly spaced antenna array resulting in one angle of arrival solution.

3.1.3 Phase Error Minimization

Phase differences measured at a fine resolution are required for accurate angle of arrival measurements. This is especially true for low elevation angle measurements as phase wrapping occurs more rapidly due to longer projected baselines, see Equation 3.2. Errors in phase measurements dramatically affect angle of arrival measurements (Jones et al., 1998). Aperture synthesis combines numerous baselines allowing for small stochastic errors to be suppressed, while large systematic phase errors are offset with calibrations. Phase errors that fluctuate over a range greater than the phase measurement accuracy between sampling, however, cause random variations in measured angles of arrival. These errors are typically caused by physical issues such as clock drift, poor cable connections, wind loads, and temperature changes.

These fluctuating phase errors are suppressed by designing the receiver antenna array to be phase error tolerant. This is done by choosing a pattern of antenna baselines that optimize for resolving the $n2\pi$ ambiguity present in Equation 3.2. Therefore, the ICEBEAR-3D design needed to be phase tolerant so that phase error would not be greater than the estimated X300 SDR's measurement phase error of $\approx 1.0°$ or cause an angle of arrival error greater than $0.1°$.

3.1.4 Maximize Angular Resolution

Angle of arrival resolution is inversely proportional to the length of the longest baseline for a given direction $\approx \lambda/d$. Selecting the maximum baseline length possible in the East-West and North-South direction is required for fine angular resolution. These maximum baseline lengths, however, cannot be greater than the coherence length of the signals scattered from the target or the interferometric fringe patterns will have no discernible amplitude. Fine targets like meteor trails have longer coherence lengths than broad targets like E region scatter. Unfortunately, the maximum coherence length of E region targets is unknown. Coherence and coherence length are discussed in more detail in Section 4.2. The longest ICEBEAR baseline was only 9λ, but land at the receiver site is available for much longer baselines. The ICEBEAR-3D design needed to select the maximum baseline lengths available to improve the angular resolution of the radar.

3.1.5 Available Land

Given the outlined objectives, many adequate array solutions were available. However, several constraints severely limited the design solution space, mainly restrictions on resources and land. To ensure time-synchronous measurement, the total electrical length of the cables to each antenna was kept equal at 600 m. Nominally, due to cable routing, this limited the radius of possible antenna placements from the radio shack to 300 m. Antenna placements were further restricted within this 300 m radius by physical barriers such as trees, shrubs, watered areas, and a co-located apiary. The radar shed, along with several other space physics experiments, also restricted the available land. The property was also adjacent to arable farmland, which could not have access obstructed. The remaining area that was available for the design is illustrated in the left image of Figure 3.2, shown as the black shaded regions.

Figure 3.2: (Left) ICEBEAR Receiver site North East of Saskatoon showing areas where antennas are not obstructed by trees, water, buildings, or other experiments. (Right) The final layout of the receiver antenna array, annotated to show antenna numbers, buried cables, and suspended cables. Image acquired from Google Maps, 2020.

3.1.6 Antennas and Radios Available

The antennas available were 12 Cushcraft 612-B Super Boomer Yagi-Uda's, shown in Figure 3.3, mounted on Golden Nugget 18" towers at a height of 15 m (Huyghebaert, 2019). At $\approx$ 50 MHz, the Cushcraft antennas have a front-to-back ratio of 30 dB, a forward gain of 14 dB, and 3 dB azimuthal beamwidth of 40°. The antennas have a 10.3 m long by

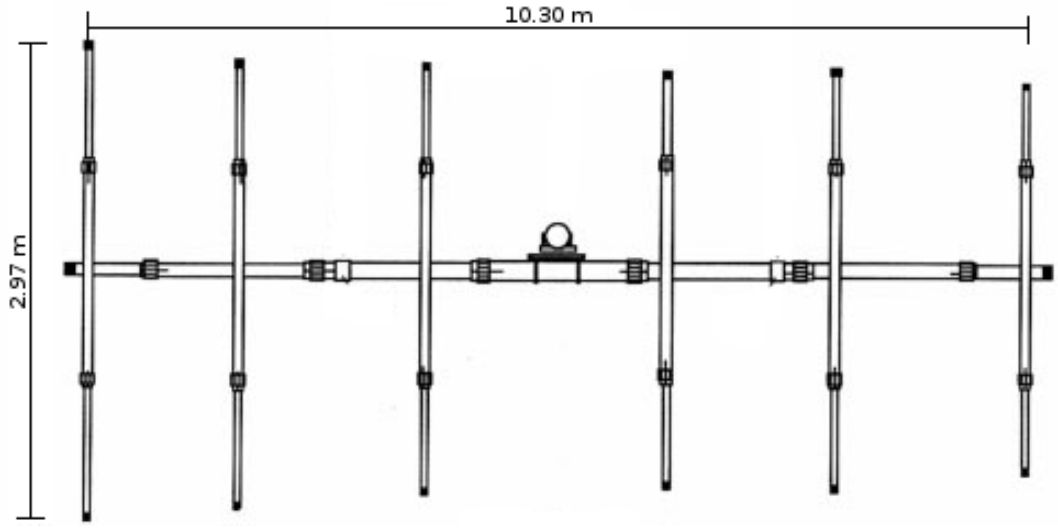

Figure 3.3: Cushcraft 612-B Super Boomer Yagi-Uda's antenna manufacturer drawings. The antenna is 10.3 m long by 3.0 m wide. At $\approx$ 50 MHz, has a front-to-back ratio of 30 dB, a forward gain of 14 dBd, and 3 dB beamwidth of 40°.

3.0 m wide footprint. Antenna towers must be placed at least 12 m apart along the long axis and 6 m apart along the short axis so that the antenna elements do not collide during high winds. Furthermore, the minimum antenna separation distance must be no shorter than 1.5λ or 9 m. This is due to phase errors caused by mutual coupling at antenna separation distances less than 1.5λ, which in turn leads to an erroneous effect on angle of arrival measurements (Jones et al., 1998). The mutual coupling effect on angle of arrival is worse in a collinear configuration (antennas placed side-by-side) than an aligned configuration (antennas placed front-to-back), as the reflecting element of the Yagi-Uda's help to isolate each antenna. However, at least one baseline in the East-West direction was requested to be exactly 1.5λ so that ICEBEAR-3D would be able to do a comparison of azimuthal spatial coherence of meteor trails with the original ICEBEAR. Five X300 SDR transceivers housed in the radar shed were available, each of which could digitize the signals for two antennas, allowing for 10 total channels. This limited the number of antennas available for the design to 10.

3.2 Design Methodology

The optimal design of receiver antenna arrays is not directly determinable since the cross-correlation function is not invertible. No method exists by which an exactly specified brightness response (discussed in Chapter 4) can be created analytically. The use of numerical methods is likewise difficult, as the number of possible antenna configurations within a given space is explosively exponential with increasing number of antennas. Thus, given a set of brightness response requirements such as resolution, signal-to-noise ratio, and sampling accuracy, a heuristic design approach must be used. The heuristic approach applied to designing the ICEBEAR-3D receiver array reconfiguration was a combination of the Jacobs-Ralston procedural phase error minimization antenna location selection method and, Random-walk, a stochastic optimization method. Given the design objectives and constraints above, this method focused on maximizing available space to obtain the highest spatial resolution possible while simultaneously maximizing phase error tolerance. The first subsection describes placing the outermost antennas of the array. This first step minimizes the solution space by reducing the number of antennas to consider by four. Next, the Jacobs-Ralston technique is described and applied to select the inner antenna locations along the principle axes so that the array is tolerant of phase errors. The technique does not perfectly place every antenna, as space for antennas becomes tight. Lastly, the Random-walk Annealing technique is defined and then used as it optimizes the uniformity of the visibility sampling function (described in Section 4.2). During all design stages, no baselines under 1.5λ were placed, and all baselines were unique to remove aliasing. As often as possible, antenna positions of the original array and cable trays were used to reduce construction costs.

3.2.1 Maximum Baselines for a T-Shaped Array

The available land shown in Figure 3.2 lends itself naturally to a T-shaped interferometer configuration. The first antennas were placed to maximize the angular resolution of the receiver antenna array. Antenna 0 remained in the same location as the previous linear array and is used as the origin of the local antenna array coordinate system. For the maximum East-West baseline, an antenna was placed as far East as available land allowed along the original ICEBEAR receiver array axis. This maintains the same 7° East of North boresight. The Jacobs-Ralston approach, which is explained next, was then used to determine the location along the East-West axis of the antenna array that would be the intersection of the

two axes in the T array. The longest North-South baseline was found by placing an antenna as far south as possible, aligned perpendicular to the East-West baseline and collinear with the intersection antenna. Maintaining antenna 0 as the origin, $(0.0, 0.0)\lambda$, then antenna 9 was placed $(16.15, 0.0)\lambda$ away (furthest to the East along the East-West axis of the T), antenna 7 was unmoved using its existing position at $(9.0, 0.0)\lambda$, and antenna 5 was placed $(9.0, -34.0,)\lambda$ (furthest South along the North-South axis of the T). These four antennas are shown in Figure 3.2 as Antennas 0, 9, 7, and 5 respectively. Note that the antenna numbers indicate bulkhead order at the radio shack, not the design selection order.

3.2.2 Jacobs-Ralston Phase Error Minimization Technique

The next four antennas, 1, 3, 4, 8, and the intersection antenna 7 had their position's selected using an iterative phase error minimization technique presented in Jacobs and Ralston (1981). This technique was designed as a solution to the $n2\pi$ ambiguity resolution problem, but has the additional unintended benefit of creating aperture synthesis receiver antenna arrays that are highly tolerant of phase errors. Given any pair of antennas sufficiently spaced by a distance d, the Jacobs-Ralston technique locates multiple positions along d that a third antenna should be placed such that it maximizes the likelihood that the correct $n2\pi$ ambiguity is selected.

The Jacobs-Ralston technique begins with analysis of three arbitrary antennas: A_1, A_2 and A_3. If A_1 and A_2 are separated by some distance d_{12} and A_3 is placed between them then three baselines are created. Assuming a planar wave arriving at the array, then from Equation 3.1, there is a phase difference for each baseline: ψ_{12}, ψ_{13}, and ψ_{23}. Figure 3.4 is a graphical representation of the three antennas and the three unique baselines generated. Each of the phase differences ψ_{mn} from baselines d_{mn} that is greater than $\lambda/2$ will include an ambiguous $n2\pi$ term as shown by Equation 3.2. The minimum baseline length d_{mn} for the ICEBEAR-3D design was $3\lambda/2$. Therefore, the true phase differences, ψ'_{mn}, are written as

$$\psi'_{12} = \psi_{12} + n_{12}2\pi = \frac{2\pi}{\lambda} d_{12} \cos\eta + n_{12}2\pi \tag{3.11}$$

$$\psi'_{13} = \psi_{13} + n_{13}2\pi = \frac{2\pi}{\lambda} d_{13} \cos\eta + n_{13}2\pi \tag{3.12}$$

$$\psi'_{23} = \psi_{23} + n_{23}2\pi = \frac{2\pi}{\lambda} d_{23} \cos\eta + n_{23}2\pi \tag{3.13}$$

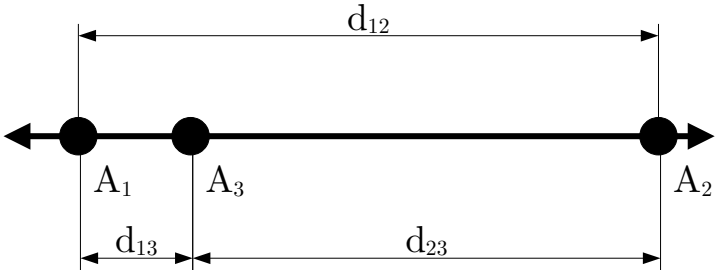

Figure 3.4: All baselines generated from the combination of three antennas, A_1, A_2, and A_3.

Since ψ_{mn} is measured between $-\pi \leq \psi_{mn} \leq \pi$ then n_{mn} are integers limited by

$$\frac{\psi'_{mn}}{2\pi} = \frac{2\pi d_{mn}}{2\pi\lambda}\cos\eta_{max} + \frac{n_{mn}2\pi}{2\pi}$$

$$n_{mn} = -\frac{d_{mn}}{\lambda}\cos\eta_{min} \pm \frac{1}{2}$$

$$|n_{mn}| \leq \frac{d_{mn}}{\lambda}\cos\eta_{min} + \frac{1}{2} \tag{3.14}$$

where the lowest elevation angle η_{min} is 0 radians for ICEBEAR-3D as targets are viewed at angles down to the horizon. Then after choosing the minimum elevation angle and normalizing by 2π, Equations 3.11, 3.12, and 3.13 become

$$\frac{\psi'_{12}}{2\pi} - n_{12} = \frac{d_{12}}{\lambda} \tag{3.15}$$

$$\frac{\psi'_{13}}{2\pi} - n_{13} = \frac{d_{13}}{\lambda} \tag{3.16}$$

$$\frac{\psi'_{23}}{2\pi} - n_{23} = \frac{d_{23}}{\lambda} \tag{3.17}$$

Combining Equation 3.15 and 3.16 and solving for ψ'_{12}

$$\frac{\psi'_{12}}{2\pi d_{12}} - \frac{n_{12}}{d_{12}} = \frac{\psi'_{13}}{2\pi d_{13}} - \frac{n_{13}}{d_{13}}$$

$$d_{13}\frac{\psi'_{12}}{2\pi} - d_{13}n_{12} = d_{12}\frac{\psi'_{13}}{2\pi} - d_{12}n_{13}$$

$$d_{12}n_{13} - d_{13}n_{12} = d_{12}\frac{\psi'_{13}}{2\pi} - d_{13}\frac{\psi'_{12}}{2\pi} \tag{3.18}$$

and since ψ'_{mn} is limited to $\pm 1/2$ this relationship is limited by

$$|d_{12}n_{13} - d_{13}n_{12}| \leq \frac{1}{2}(d_{12} + d_{13}) \tag{3.19}$$

Thus, for any choice of n_{12} there are a limited number of options for n_{13}. Given all possible phase measurements for a pair of baselines, a ψ'_{12} by ψ'_{13} phase by phase space limited to $\pm 1/2$ is definable. An example of this phase by phase space is shown in Figure 3.5. A set

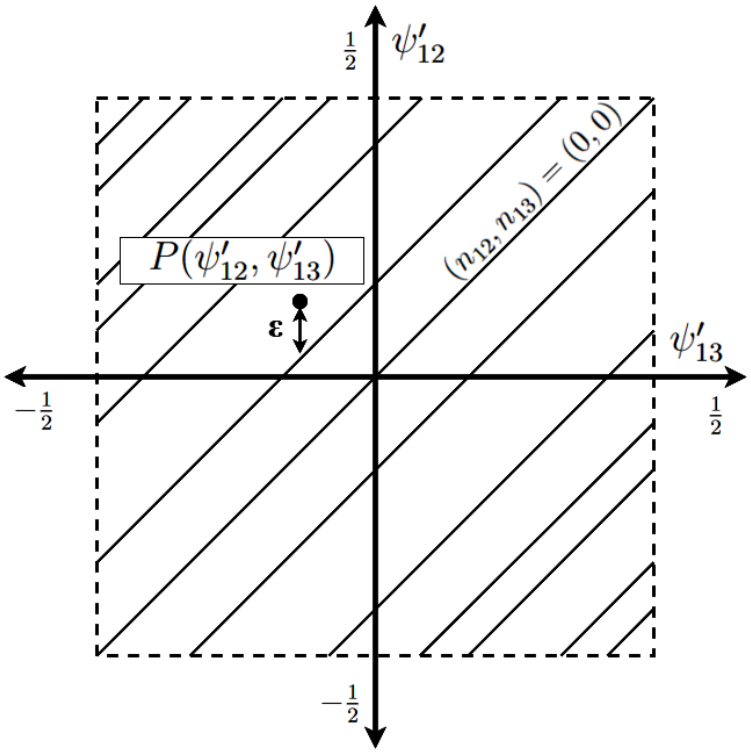

Figure 3.5: Sample phase space generated by ψ'_{12} and ψ'_{13} with $\pm 1/2$ limits showing constant n ambiguity lines, n-lines, and an example point $P(\psi'_{12}, \psi'_{13})$ with error ε (Jacobs & Ralston, 1981) from the nearest n-line.

of phase measurements in this space is defined by a point $P(\psi'_{12}, \psi'_{13})$. Each pair of n_{12} and n_{13} creates diagonal lines within the phase by phase space. These lines of constant phase are called *n-lines*. In the absence of any phase measurement error the point $P(\psi'_{12}, \psi'_{13})$ aligns with one of the n-lines allowing for perfect determination of the ambiguity n_{12} and n_{13}. However, real phase values will always have inherent noise, and as such these points, $P(\psi_{12}, \psi_{13})$, will not lay on an n-line. The process of selecting the correct $n2\pi$ ambiguity is as

simple as selecting the n-line that is closest to $P(\psi_{12}, \psi_{13})$ where the difference is the error ε. Although simple in nature, actually determining which constant n-line is closest is non-trivial when they are narrowly separated. Phase errors which rapidly fluctuate further complicate this selection process as they cause $P(\psi_{12}, \psi_{13})$ to drift across the midpoint between two n-lines. Maximizing the spacing between adjacent n-lines increases the statistical likelihood of selecting which n-line $P(\psi'_{12}, \psi'_{13})$ is closest. This both resolves ambiguities and allows for more phase tolerance as larger phase errors must occur before $P(\psi'_{12}, \psi'_{13})$ crosses a midpoint between n-lines.

The procedure to finding the optimal placement for the third antenna, A_3, is determined by sliding the third antenna between the pair, A_1 and A_2, so that d_{13} goes from the minimum allowable separation distance to $d_{12}/2$. At each step the separation distance between each pair of adjacent n-lines is determined, and the minimum separation distance of these pairs is recorded. These values are then plotted against the baseline distance d_{13}, see Figure 3.6.

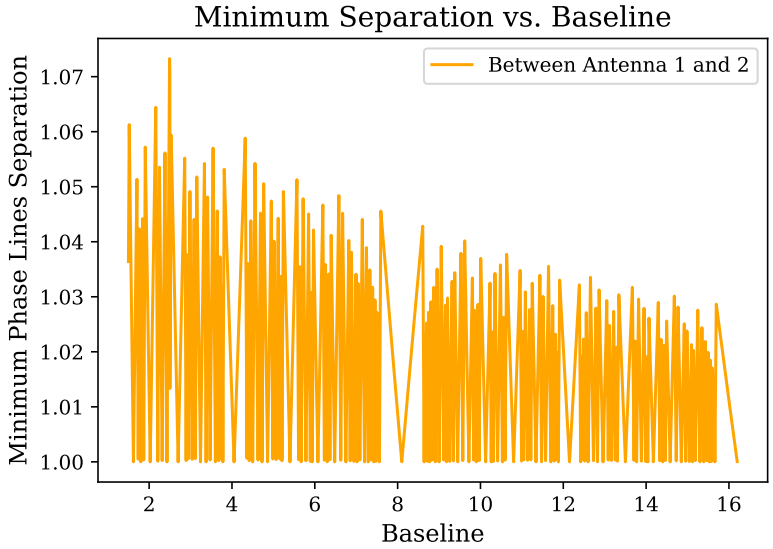

Figure 3.6: Minimum phase line separation (minimum n-line separation) versus baseline distance of the first and second antennas. This is used to select the position for a third. In the design of ICEBEAR-3D this plot was used for selecting the locations of antennas 1, 3, and 7.

The maxima of this function are the phase error minimum locations. The function tends to have many maxima and minima which oscillate. The function produces a sawtooth like pattern. This is due to the minimum separation distance increasing as baseline distance

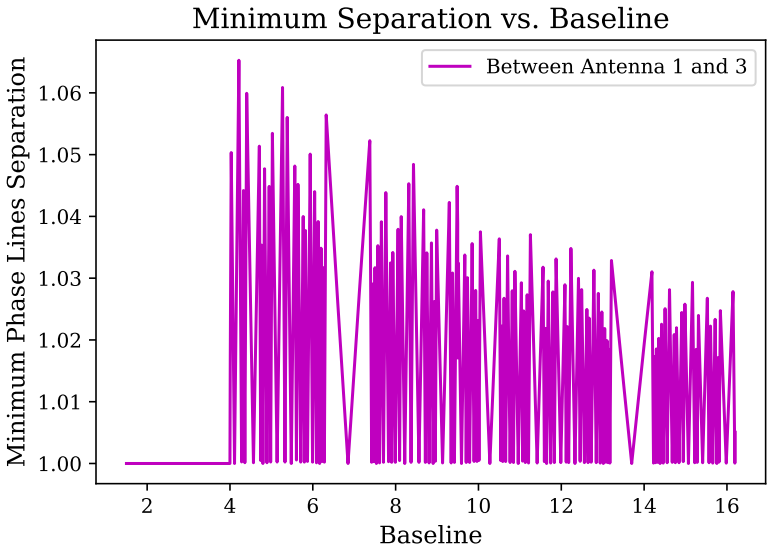

Figure 3.7: Minimum phase line separation (minimum n-line separation) versus baseline distance of the first and third antennas. This is used in part, along with the previous first and second plot, to select the position for a fourth antenna. In the design of ICEBEAR-3D this plot was used for selecting the locations of antennas 3, and 7.

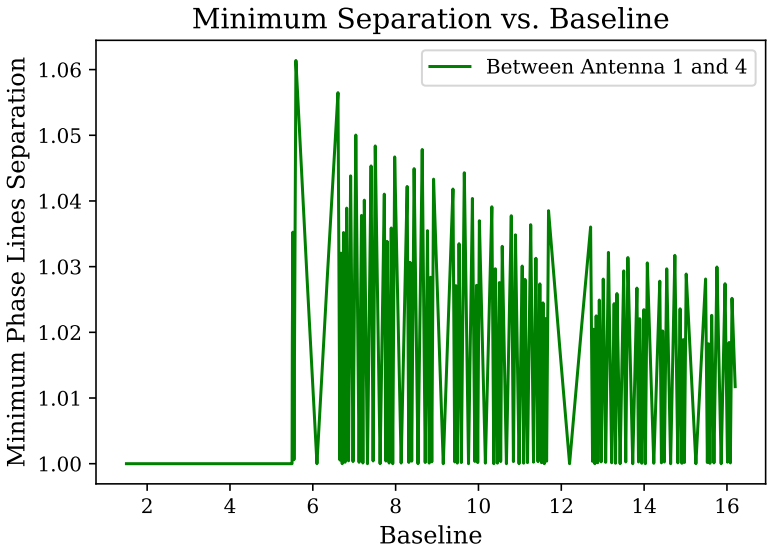

Figure 3.8: Minimum phase line separation (minimum n-line separation) versus baseline distance of the first and fourth antennas. This is used in part with the previous plots to select the position for a fifth antenna. In the design of ICEBEAR-3D this plot was used for selecting the locations of antenna 7.

increases until a point where adjacent n-lines get closer to their opposite partners. Slight shifts in antenna position due to wind or any other effects that cause fluctuating phase errors between calibration cycles is tolerated by selecting the antenna positions in regions with the widest peaks. With this in mind, the antenna location chosen must simultaneously maintain all unique baseline vectors, be within the acceptable land area, and be optimal for both baselines d_{12} and d_{13}. This process is then continued for a fourth antenna, and so on until all antennas are selected along an axis. The location selected for each subsequent antenna must correspond to a wide maximum of minimum n-line separation for all possible baseline pairing. Given only six antenna location needed to be selected by this process, it was performed manually.

The locations of ICEBEAR-3D antennas 1, 3, and 7 were selected in this manner for the East-West axis. Antennas 4 and 8 were located likewise for the North-South axis. Figures 3.6 through 3.8 are the minimum separation distance versus baseline distance plots for selecting Antenna 1, 3, and 7 locations. Antenna 7 was selected at 9λ from Antenna 0, which is not the optimal location. However, this location aligned with an already existing antenna and produced the longest possible North-South baseline. The averaged baselines result is shown in Figure 3.9 and zoomed in on Figure 3.10. The location for Antenna 7 although not optimal is the best for the land area available and was minimally varying over $\pm 0.08\lambda$ (± 0.5 m) baseline distance. The code for the algorithm is given in Appendix A.

3.2.3 Random-walk Annealing Technique

Although the Jacobs-Ralston approach could be expanded to evaluate phase error separation minimization in 2-dimensions allowing placement within a plane rather than an axis, such an exhaustive approach was deemed unnecessary. The primary purpose of the remaining two antennas was suppressing artefacts (the dirty beam of the sampling function convolved with the true brightness distribution discussed in Chapter 4) in brightness maps. This was achieved by maximizing the uniformity and coverage of the visibility sampling space as recommended by Keto (1997), which reduces artefacts inherent to sparse arrays in the final image. The remaining two antennas were located off-axis by using a rudimentary custom stochastic method loosely based on simulated annealing affectionately referred to as *Random-walk Annealing*.

The method perturbates the location of each antenna of interest within a bounded region.

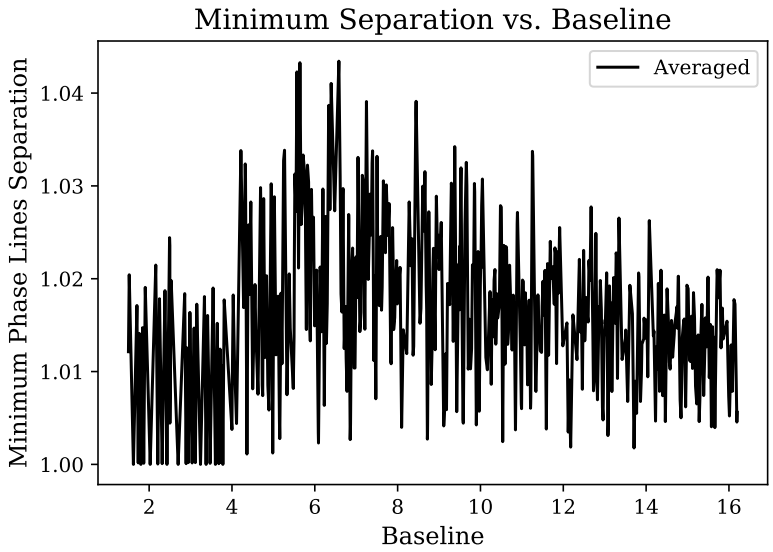

Figure 3.9: The average of minimum n-line separation functions for combinations; first and second, first and third, first and fourth, and third and fourth. This is used for selecting the position of a fifth antenna along d_{12}. In the design of ICEBEAR-3D this plot was used for selecting the location of antenna 7.

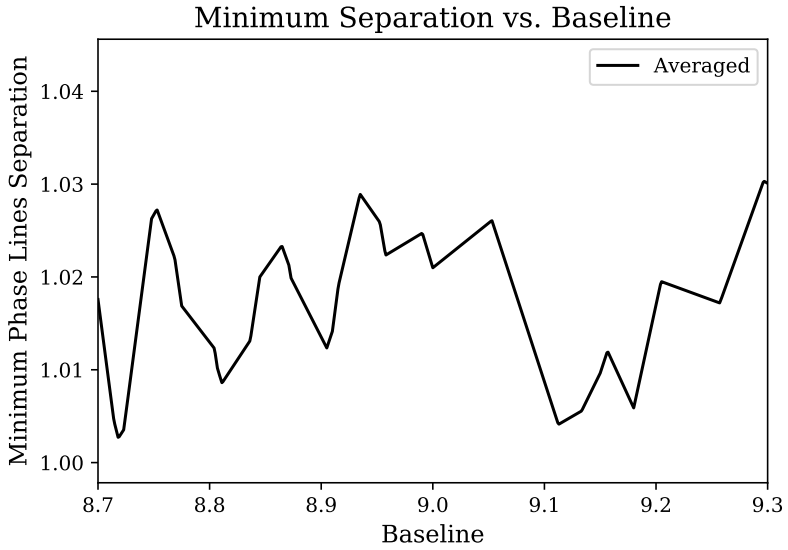

Figure 3.10: A zoomed in view of Figure 3.9 showing the region around the 9λ baseline distance selected for Antenna 7. The baseline selected is not an optimal peak, but is wide, not greatly varying over $\pm 0.08\lambda$ (± 0.5 m).

The distance of each antenna perturbation is individually weighted by w_q. The perturbations continue until the following conditions are met: all baselines are unique, all antennas are spaced greater than 1.5λ, and the sampling space meets the condition of uniformity. Uniformity here meaning no point corresponding to an antenna of interest within the sampling space being within 1 λ radius of another. With each iteration, the antennas of interest which do not meet the aforementioned conditions are allowed to perturb a greater distance by increasing w_q by the elasticity factor e_q. Antennas that do meet the aforementioned conditions have their w_q decreased by the dampening factor d_q. The selection of e_q and d_q control the rate at which the antenna locations stabilize. The algorithm written in Python is given in Appendix B. The following is the pseudocode for the Random-walk Annealing algorithm

```
# conditions is a boolean array with length the number of antennas
# positions are antenna (x, y) locations
# weights are per antenna
while any conditions are true:
    positions = (random within boundary from
                    (positions - weights) to (positions + weights))
    baselines = separation distance between each positions combination
    for each position in positions:
        if position within minimum antenna spacing of another position:
            condition = False
        for each baseline in baselines made from position:
            if baseline not unique:
                condition = False
            if baseline <= uniformity minimum separation:
                condition = False
        if condition is False:
            weight *=  elasticity
        else
            weights *= dampening
return positions
```

The remaining two antennas positions were determined by running the Random-walk Annealing code 1000 times, as this simple method does not ensure the solution is a global minimum. The elastic and dampening factors were selected by a process of trial and error until values that produced good results in a reasonable time were found, these values were $e_q = 2$ and $d_q = 0.1$. All other antennas were made unmovable. Each simulation was allowed to iterate until a stable solution was found. Evaluation of each simulation was done by comparing the dirty beams, also called the point-spread function in optics, produced to each other. The selected simulation's dirty beam is shown in the third panel of Figure 3.11. An ideal dirty beam has a very narrow main lobe, and the largest amplitude difference between the two highest lobes also known as the side-lobe level. The designer must strike a balance between these

two criteria as real world constraints do not allow for a perfect solution. Often one criteria can be favored over another depending on the use case. For ICEBEAR-3D, the side-lobe level cutoff was set to -5 dB and the 3 dB elevation lobe width to 1°. Several simulations passed these criteria, all of which were equally acceptable. The final choice was the one that allowed for the least expensive cable tray construction. Although, Random-walk Annealing is not very sophisticated, it was able to resolve the design problem. It placed antenna 2 at $(12.2, -16.5)\lambda$ and antenna 6 at $(7.0, -29.3)\lambda$ finishing the design.

3.3 Final Array Design

The final ICEBEAR-3D design reconfigured the antennas into a non-uniform sparse coplanar T-shaped array optimized for robust phase tolerance. Although the receiver antenna array configuration has changed, processing of the raw IQ samples remains the same as discussed in Chapter 2. The final design is shown on the right of Figure 3.2. The exact antenna locations as-built do not exactly match the design specification. Observe that antenna 8 is located slightly off-axis due to unforeseen obstructions during construction, blocking the original location. The shifted location has minor effects on the overall capabilities. Figure 3.11 summarizes the as-built locations of each antenna in local coordinates measured from antenna 0 and shows the coverage of the visibility sampling space, which will be discussed in Section 4.2, as well as the dirty beam. The array being T-shaped with an asymmetrical visibility sampling space and different maximal baselines in the North-South versus East-West means the array does not have exactly the same resolution in all directions. Table 3.1 is a list of the final as-built antenna positions. Although sparse in some sections, the redesigned receiver antenna array is one of the possible designs with the most uniformly filled visibility sampling spaces possible.

The receiver antenna redesign was created within all the constraints. Verifying that the design met the phase tolerance objective was determined by intentionally introducing error in the recorded as-built antenna positions to displace the measured angle of arrivals until a difference from the correct angle of arrival of 0.1° was found. This occurs when an antenna is displaced by about 25 cm, which corresponds to a phase error of 14.86°, well above the measured X300 SDR's measurement phase error of $\approx 1.0^\circ$. The expectation is that the displacement of antennas due to wind shear, combined with phase drifts between calibration periods, will not be more than 14.86°. In any case, the synthesis of a larger aperture by the

Table 3.1: The final design antenna positions in local coordinates measured from antenna 0 in units of meters.

Num	x(m)	x(λ)	y(m)	y(λ)	z(m)	z(λ)
0	0.00	0.0	0.00	0.0	0.00	0.00
1	15.10	2.5	0.00	0.0	0.09	0.01
2	73.80	12.2	-99.90	16.4	0.35	0.06
3	24.20	4.0	0.00	0.0	0.22	0.04
4	54.50	9.0	-94.50	15.6	0.68	0.11
5	54.50	9.0	-205.90	34.0	-0.06	0.01
6	42.40	7.0	-177.20	29.3	-1.07	0.18
7	54.50	9.0	0.00	0.0	-0.75	0.12
8	44.20	7.3	-27.30	4.5	-0.53	0.09
9	96.90	9.0	0.00	0.0	-0.41	0.07

combination of antennas suppresses stochastic phase error effects. Aperture synthesis and radar imaging is discussed next in Chapter 4. The verification of elevation angles as well as the challenges of a low elevation horizon facing planar array will be discussed in Chapter 5.

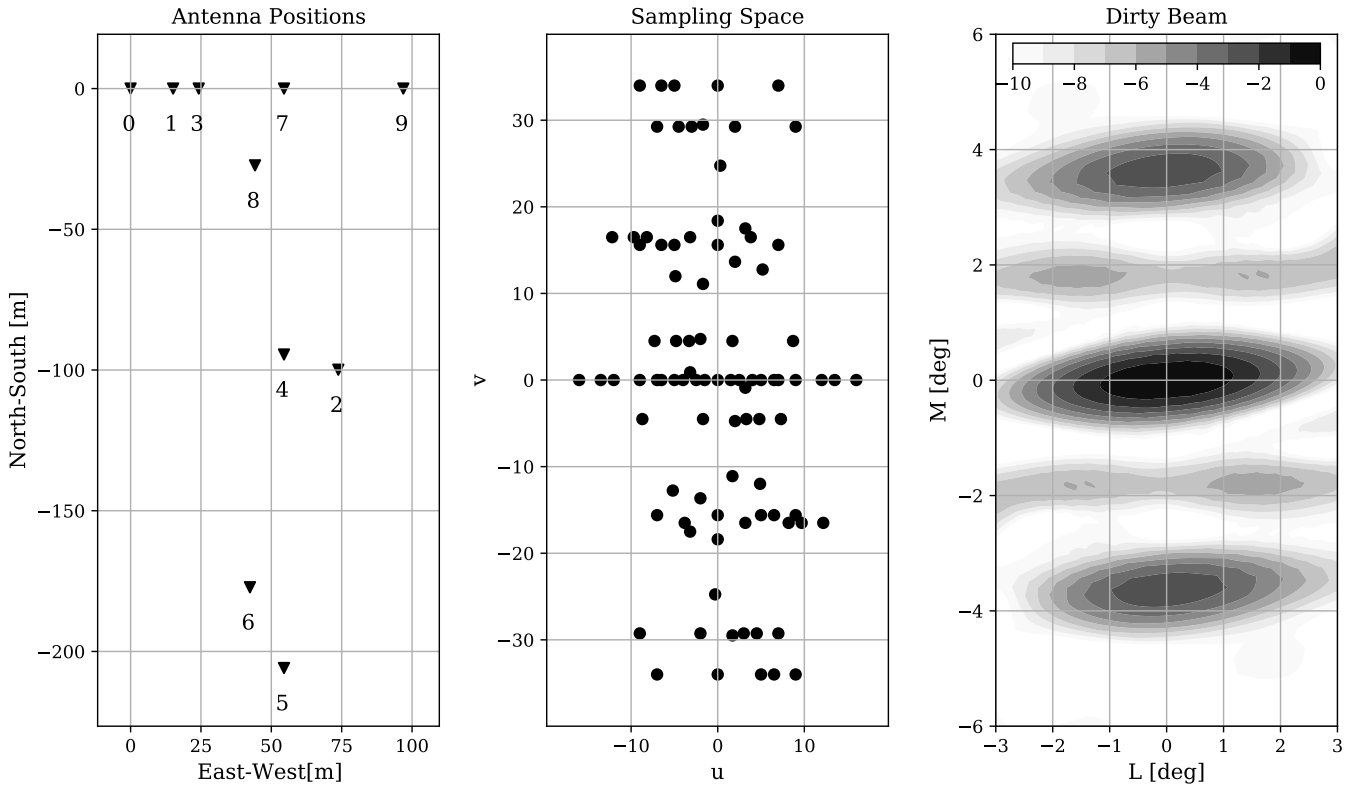

Figure 3.11: (Left) Receiver antenna positions relative to antenna 0. (Center) The sampling space, showing the spatial frequency coverage in the u,v plane. (Right) A contour plot of the final array design dirty beam given in direction cosines with power in decibels.

4 Radar Imaging

Sections 4.4, 4.5, and 4.6 of this chapter contains in part works directly from my contributions in Lozinsky et al. (2022).[1]

Radar imaging is the process by which a radar illuminates a target, then uses the returned light to create a picture of the target at the radar's operating frequencies. The two most common types of imaging radars are; Synthetic Aperture Radar (SAR) which produces two-dimensional images by sampling a target from a series of positions using real apertures; and Inverse Synthetic Aperture Radar (ISAR) which produces two-dimensional or three-dimensional images by sampling a moving target from a single stationary real aperture. This can be thought of as either moving your radar about a target or moving a non-changing target around a radar. ICEBEAR-3D targets both move quickly and change rapidly, making neither method suitable. However, general radio interferometry theory is suitable.

Radio interferometry has been largely developed and advanced by the radio astronomy community for the observation of distant celestial objects. The first radio interferometer, however, was a radar application using an antenna mounted on a sea-cliff overlooking the ocean, known as the sea-interferometer (Sullivan, 1991). This radar would detect interferometric patterns in its echoes and was capable of tracking aircraft arriving over the horizon when the sea surface was calm. The interferometric patterns were generated by the constructive and destructive interference between the real antenna and the imaginary reflection antenna below the sea-surface reflection plane. The Australian team who developed the sea-interferometer first used it to detect aircraft coming over the horizon during the post World War II period, but was quickly redirected towards astronomical observation. The instrument eventually led to the discovery that sunspots emit strong radio waves and the measurement of how spatially narrow emissions from Cygnus A truly are (Sullivan, 1991). Radio interferometry techniques

[1]Lozinsky, A., Hussey, G., McWilliams, K., Huyghebaert, D., and Galeschuk, D. (2022). ICEBEAR-3D: A Low Elevation Imaging Radar Using a Non-Uniform Coplanar Receiver Array for E Region Observations, *Radio Science*, 57(3). DOI: 10.1029/2021RS007358

have advanced within the radio astronomy field, ultimately leading to Very Long Baseline Interferometry (VLBI), a technique used to image black holes. There are two classes of radio interferometer: additive and multiplicative. Additive interferometry is just another name for beam forming, which is the process by which signals from spaced antennas are added together prior to detecting a target. In multiplicative interferometry, the signals from spaced antennas are multiplied together to form images. In lay terms, beam forming is like shining a flashlight into a dark room then determining if the target was inside the beam of light or not, whereas imaging is like turning on the lights in the room then looking for the target. ICEBEAR-3D is concerned with multiplicative interferometry, specifically, the application of Synthesis Aperture Imaging (SAI) for radars. SAI broadly speaking is the process by which a set of sparsely placed antennas are combined virtually to form a much larger imperfect aperture. Incident waveforms received by a synthesized aperture are computed into images at the instrument's frequency band by way of the Fourier transform relationship. The design of such sparse arrays for SAI was previously discussed in Chapter 3.

This chapter describes SAI and radar imaging as it applies to ionospheric radars. Specifically, this chapter focuses on radar imaging foundations and techniques as they apply to ICEBEAR-3D. This is done by building upon the interferometer basics presented in Chapter 3. The discussion is guided by an explanation of the principle terms, Visibility and Brightness, and how they are inexorably tied together by the van Cittert-Zernike theorem (vCZ). The discussion will then lead to the limitations of the vCZ as a direct imaging algorithm for low elevation imaging radars and how the Spherical Wave Harmonic Transform (SWHT) is much better suited. From there the discussion will focus on the SWHT technique, how it performs, how it was made significantly faster, and how the SWHT was modified into the Suppressed-SWHT in order to unambiguously resolve target angles of arrival.

4.1 Radio Interferometry

In principle, radio interferometry is no different from optical interferometry, except that the electromagnetic wavelengths are significantly longer. One may consider a radio interferometer made of two antennas separated by some distance receiving an electromagnetic plane wave from a point source as a Young's two-slit experiment, where the antennas are the slits (Thompson et al., 2001). Take for example a far-field plane wave incident upon a planar interferometer, as seen in Figure 4.1.

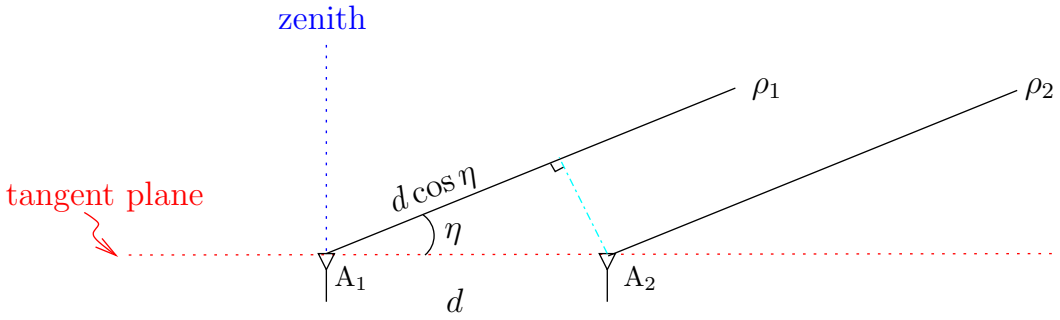

Figure 4.1: Young's two-slit geometry for angle of arrival elevation angle η. The waves on paths ρ_1 and ρ_2 are from the same source and satisfy the Young's two-slit condition $\rho_1, \rho_2 \gg d$. The wave on path ρ_1 to antenna A_1 travels a distance $d\cos\eta$ further than the wave on path ρ_2 to antenna A_2, which corresponds to a phase difference of $\psi = 2\pi\frac{d}{\lambda}\cos\eta$ as given by Equation 4.4.

The plane wave will arrive at the two antennas with some geometric time delay τ_g

$$\tau_g = \frac{d}{c}\cos\eta \tag{4.1}$$

where d is the antenna separation distance (two-slit separation distance), c is the speed of light in a vacuum, and η is the source direction of the signal, or angle of arrival. The interferometer's response generates a fringe pattern with respect to the geometric delay

$$F = \cos\left(\frac{2\pi d}{\lambda}\cos\eta\right) \tag{4.2}$$

where λ is the wavelength and the fringe spacing is given by,

$$\Delta\eta = \lambda/d \tag{4.3}$$

which also defines the angular resolution of the interferometer. In the case of an interferometer with multiple antennas, the largest separation distance d defines the angular resolution. The angle of arrival η of the signal can be determined by measuring the phase difference ψ between the two antennas, separated by distance d (Thompson et al., 2001).

$$\psi = \frac{2\pi}{\lambda}d\cos\eta \tag{4.4}$$

$$\psi = k_0 d\cos\eta$$

where $k_0 = 2\pi/\lambda$ is the wavenumber. Angles of arrival measured with such an interferometer

are ambiguous if the separation distance d is greater than $\lambda/2$ due to the inherent $n2\pi$ phase sampling ambiguity

$$\psi\prime = \frac{2\pi}{\lambda} d\cos\eta + n2\pi \tag{4.5}$$

This $n2\pi$ ambiguity is responsible for the fringes in optics, which are referred to as grating lobes in radio applications. With the use of a sufficiently large ensemble of interferometer pairs, this ambiguity is removed, provided the baseline of each pair is both unique and not a factor of any other pair. This is the same process described in Figure 3.1 from Chapter 3 where unique samples break down ambiguities.

Generalizing this formula to account for the antennas in 3D space gives

$$\psi\prime = 2\pi\vec{b}\cdot\vec{k} + n2\pi \tag{4.6}$$

where $\vec{k}$ is the incident wavevector, and $\vec{b}$ is the wavelength normalized antenna separation vector or baseline $\vec{b} = \vec{d}/\lambda$. Where explicitly, the components $\vec{b} = (u, v, w)$ are found from the antenna's locations local coordinates x, y, z as

$$u = \frac{x_1 - x_2}{\lambda}, v = \frac{y_1 - y_2}{\lambda}, w = \frac{z_1 - z_2}{\lambda} \tag{4.7}$$

These wavelength normalized spacing coordinates u, v, w are also the spatial frequencies. They define the sampling function in the visibilty domain used for synthesis aperture imaging. In application, the phase ψ, which is related to τ_g, is the phase component of the complex visibility V, and is used to solve for the angles of arrival of the incident waveform. This process of combining multiple interferometer baselines is aperture synthesis, it is the process of converting visibility into brightness.

4.2 Visibility and Brightness

The term visibility, also known as interferometric visibility, interference visibility, or fringe visibility, originates from optical interferometry with the Michelson interferometer. It is a mathematical representation of the fringe pattern formed by an interferometer. The definition of fringe visibility is the ratio between the amplitude of the interference pattern to the sum

of the powers of the individual waves (Thompson et al., 2001)

$$V = \frac{intensity\ of\ maxima - intensity\ of\ minima}{intensity\ of\ maxima + intensity\ of\ minima} \tag{4.8}$$

This is a purely real quantity that is normalized to unity. In radio interferometry complex visibility is used, which was defined by Bracewell (1958) to account for phase allowing imaging of asymmetric and complicated sources. Complex visibility represents a portion of the Fourier transform of an observed signal with respect to the baseline direction defined by the spaced receiving antennas.

This statement is often a point of confusion, to be abundantly clear visibility is measured with respect to a wavelength and spatial frequency. For an incident waveform with wavenumber $k_0 = 2\pi/\lambda$ a visibility is the complex value sampled at a spatial frequency defined by the baseline $\vec{b}$. The baselines are the spatial frequencies the incident signal is sampled at, a map of this sampling function point in the visibility domain for ICEBEAR-3D is shown in the center plot of Figure 3.11. Each point is located at some (u, v) point calculated by wavelength normalized separation vector, or conjugate vector, between the antenna pair (m, n), except the point at $(u = 0, v = 0)$ which is the 0^{th} baseline formed by an antenna with itself. A visibility for an antenna pair (m, n) is written as

$$V_{mn}(u_{mn}, v_{mn}, w_{mn}, k_0) \tag{4.9}$$

Since in imaging it is the baseline vectors $\vec{b}$ that are important rather than the antennas it is convenient to index the visibilities by the i^{th} baseline (antenna pair)

$$V_i(\vec{b}_i, k_0) \tag{4.10}$$

The ensemble of visibilities for a synthesized aperture, as discussed in Chapter 2, are made of the cross-correlations between every antenna pair and at least one autocorrelation (the value at $u, v, w = (0, 0, 0)$). Each visibility in the ensemble has a complex numerical value at a given coordinate.

Visibilities as given in Chapter 2 were defined by Equation 2.16. The result of that computation was the visibility quantities for 1 s in time at a specific Doppler frequency, range, and for a specific antenna pair. This means for each and every range-Doppler bin every 1 s there are 91 visibility values. The 91 visibility values includes all 45 unique pairs ($n(n-1)/2$ where $n = 10$ for ICEBEAR-3D), their conjugate pairs, and one antenna auto-correlated.

Visibilites for a single range-Doppler bin are represented by

$$V_i(\vec{b}_i, k_0) = S_m(\vec{b}_i, k_0) S_n^*(\vec{b}_i, k_0) \tag{4.11}$$

Where S is the range-Doppler-intensity spectra from Chapter 2 at a specific range and Doppler indices.

The Weiner-Khinchin theorem states that the Fourier transform of the square of a signal is equal to the autocorrelation of that signal (Thompson et al., 2001). For the case with two different signals, the Cross-Correlation theorem states that the Fourier transform of the product of the first signal and the conjugate of the second is equal to the cross-correlation of two signals (Thompson et al., 2001). The power density spectrum, or simply the power spectrum of a waveform, is measured by the cross-correlation of signals from spaced antennas. In other words, the power spectrum of an incident waveform is the Fourier transform of the visibility. This is called brightness.

Two-dimensional brightness maps are images at the radar frequency. The term brightness is used rather than intensity, as brightness includes the antenna receiving array frequency response and intensity is purely the energy in the incident wave. The Fourier transform that relates brightness and visibility is the van Cittert-Zernike theorem.

4.3 Van Cittert-Zernike Theorem

Conventional synthesis aperture radar imaging algorithms used in ionospheric physics applications are often modifications or variations of radio astronomy methods (Hysell, 2018). The basis of all of them being the van Cittert-Zernike theorem. The theory states that there is a 2D Cartesian Fourier transform pair between the visibility and brightness assuming the target source is incoherent, in the far-field, and the whole source lies in a single plane (van Cittert, 1934; Zernike, 1938). The theorem is stated as

$$V(u,v,w) = \int_{-\infty}^{\infty}\int_{-\infty}^{\infty} \frac{B(L,M)}{\sqrt{1-L^2-M^2}} \exp\left[j2\pi\left(uL + vM + w\left(\sqrt{1-L^2-M^2}-1\right)\right)\right] dLdM \tag{4.12}$$

where $V(u,v,w)$ is the visibility at baseline (u,v,w), $B(L,M)$ is the brightness projected from the celestial sphere to the direction cosine plane (L,M). Figure 4.2 describes the

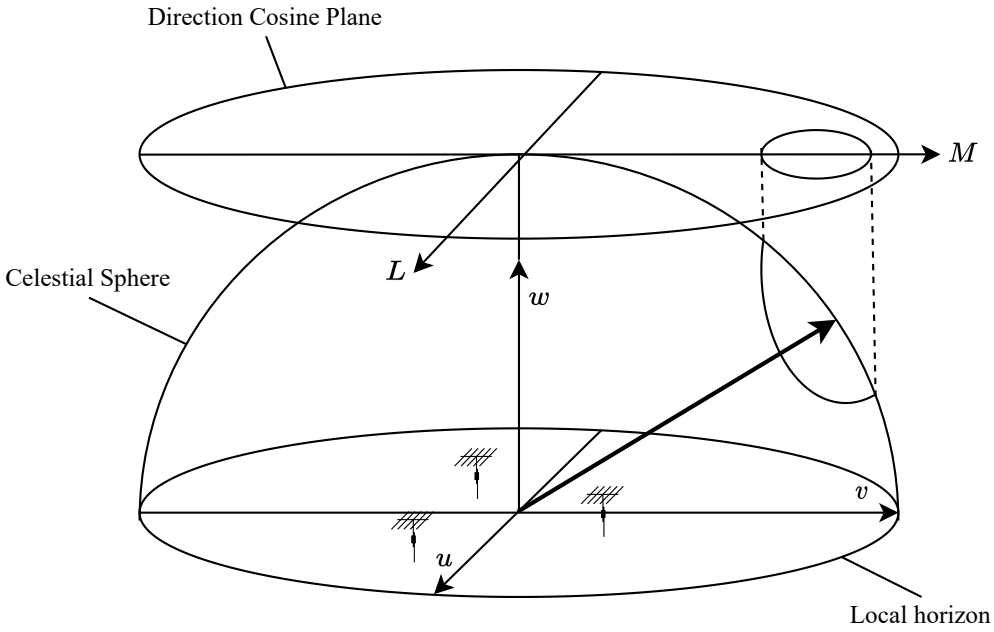

Figure 4.2: An extended target located at some point on the imaging celestial sphere, the equator coincides with the local horizon, being projected to the direction cosines (L, M) plane. The target is distorted by the projection in both azimuth and elevation. This distortion is exasperated as the elevation angle reaches the horizon. This is the standard configuration for the derivation of the van Cittert-Zernike theorem.

geometry for the vCZ. The direction cosines L and M are defined as

$$L = \cos\theta \sin\phi, \quad M = \sin\theta \sin\phi \tag{4.13}$$

and the final direction cosine is defined in terms of L and M as $\sqrt{1 - L^2 - M^2}$. Equation 4.12 does not have the form of a Fourier transform due to the w term. Assuming targets are viewed over a small angle at zenith where $L \ll 1$ and $M \ll 1$ and the receiving antennas lie in a plane such that $w = 0$ everywhere, then $w(\sqrt{1 - L^2 - M^2} - 1)$ reduces to 0. This is the most common case for radio astronomy where the vCZ is used. The vCZ then reduces to

$$V(u, v) = \int_{-\infty}^{\infty} \int_{-\infty}^{\infty} B(L, M) \exp(j2\pi(uL + vM)) dL dM \tag{4.14}$$

where the normalization term $1/\sqrt{1 - L^2 - M^2}$ has been absorbed by $B(L, M)$ as it becomes constant approaching 1 for small zenith angles. A small correction to $B(L, M)$ is needed when

the targets being imaged are larger than the receiving antenna beam; this was not the case for ICEBEAR-3D as targets were not expected to be over 60° spatially extended. Equation 4.14 now has the form of a 2D Fourier transform.

Given that the inverse of Equation 4.14 is well known, the problem becomes estimating the brightness given a discrete set of sparsely sampled visibilities. In the ideal case, the true brightness map $B(L, M)$ would be perfectly constructed from the Fourier transform of the ideal visibility function, $V(u, v)$ which would fully samples all spatial frequencies. However, in the real world this is never the case. Rather, the sampling function $F(u, v)$, which is defined mostly by the receiver antenna array configurations, determines where $V(u, v)$ is sampled and subsequently undersampled. The actual measurements made by the radar is $V(u, v)F(u, v)$. The Fourier transform of $F(u, v)$ is the dirty beam $G(L, M)$. The resulting images are $B(L, M) * G(L, M)$. All images produced with sparse arrays are the true image convolved with the dirty beam. The design of the receiver antenna array in Chapter 3 was concerned with shaping this dirty beam. The dirty beam for ICEBEAR-3D is shown in the right plot of Figure 3.11, it has a prominent asymmetrical main lobe and less powerful adjacent side lobes. The convolution of the dirty beam with the real image causes targets to appear to bleed together or ripple outwards.

Removing the dirty beam is not as simple as deconvoling it from the images, as the true dirty beam is hard to determine. It is a combination of the radar receiver array layout, ground reflections, system noise temperature, and many other variables. A strategy used to determine the dirty beam of a system is to use a known point-like calibration source and deconvolve the known brightness response that source would make, leaving the exact dirty beam (Thompson et al., 2001). There is no such calibration source available for ICEBEAR-3D, although there has been some success using Cygnus-A for calibration (Galeschuk, 2021). Essentially every method which attempts to deconvolve the dirty beam from images has the form of a linear inverse problem. They attempt to solve the inverse problem of the vCZ theorem when the visibility domain is sparsely and irregularly sampled. The two most popular methods are CLEAN and Max-entropy (Thompson et al., 2001). These methods have been successful in the ionospheric radar imaging field, but are ill-suited as they assume targets are point sources, which is a fair assumption for meteor trails, but not for plasma instabilities of the E-region which are extended source targets. These methods are also computationally intensive by their nature. ICEBEAR-3D avoids using any deconvolution method, as they are unnecessary to obtain the required angle of arrival accuracy.

The issue with assuming the w term is 0 is that it fundamentally limits the imaging radar to narrow fields of view and zenith facing elevation angles. As at lower elevation angles, say near the horizon, targets are projected to the imaging plane normal to the zenith direction, which causes distortions that exasperate the already complex nature of low elevation angle detection. Figure 4.2 shows how a target at low elevation is distorted when projected unto the direction cosine plane. This distortion cause an error in target elevation and azimuth angle of arrival. This error worsens as the elevation angle lowers. In the top of Figure 4.3, the antennas lie in a plane and the direction cosine plane is tangential to the zenith. A target arriving between elevation angles θ_2 and θ_1 has some vertical spatial extent. Assuming the arc length on the celestial sphere is small, the change in the vertical extent of the target is found by

$$L_2 - L_1 = (\theta_1 - \theta_2) \sin \theta_2 \tag{4.15}$$

where the radius of the celestial sphere and maximum direction cosine L is unitary. As the target lowers towards the horizon $\sin \theta_2$ approaches 0, making the target projected into the direction cosine plane vanish. Azimuthally, the target smears around the projected direction cosine plane perimeter. This make target locating extremely difficult.

The solution, one may think, would be to redefine the direction cosine plane to be tangential to the horizon, as shown in the bottom of Figure 4.3. This changes the antennas from lying in the u, v plane to the u, w plane. However, this new basis then inherits the w problem previously discussed. As, in this right-handed reference system, the antennas are now in the same u, w plane with constant v, but now the w positions are not constant, and cannot be neglected. Methods exist that attempt to resolve the w problem by regriding the baselines into w layers and solving using the standard vCZ for each layer before recombination. These are called w-projection and w-stacking (Cornwell & Perley, 1992; Offringa et al., 2014). Regardless, for ICEBEAR-3D this solution fails as having only 10 antennas provides to few baselines per w-layer. Additionally, there are non-negligible errors which come with regridding. ICEBEAR-3D has high phase error tolerance for an instrument of its kind at $\pm 1°$, but the spatial frequencies are sampled irregularly. Regridding the visibility samples from their (u, v, w) position to a regularized (u, v, w) grid induces artificial quantization error. Artificial phase errors are especially concerning for ICEBEAR-3D as it operates entirely in the low-elevation regime, where small phase differences correspond to large elevation differences. Regridding is not acceptable, as the auroral E region needs to be measured from low elevation angles to achieve perpendicularity of the radar wave with the magnetic field for scattering.

In most cases, ionospheric E region targets are spatially extended sources that need to be

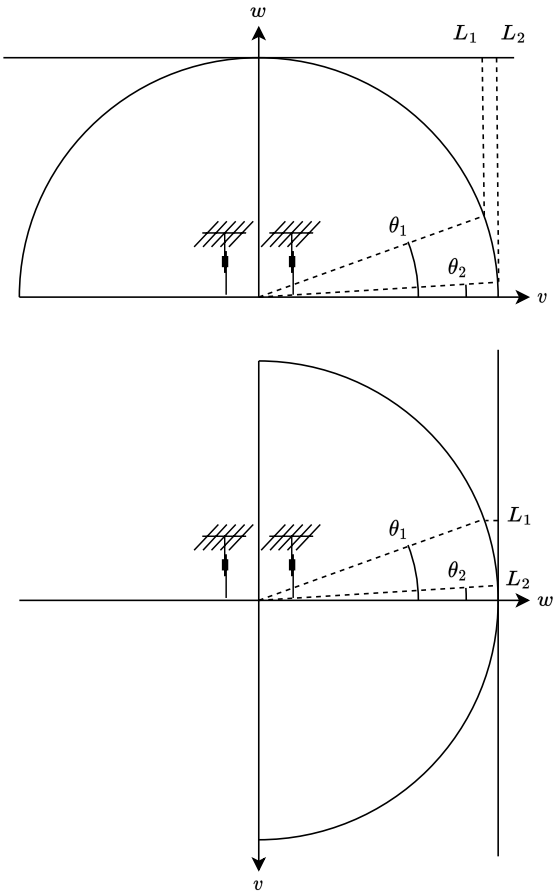

Figure 4.3: (Top) A cross-sectional view of the celestial sphere and direction cosine plane. (Bottom) A cross-sectional view with the phase reference direction mathematical orientated along the horizon, resulting in w plane offset. In both views an extended target subtended by angles θ_1 and θ_2 is show projected to the direction cosine (L, M) plane. In the top figure, there is significant distortion. In the bottom figure, the distortion is minimal as the projection a small angle from the phase reference direction.

measured over wide fields of view ±45°. The maximum field of view available when imaging with the vCZ at low elevations is restricted by the instrument's phase tolerance and longest baseline

$$\delta\psi = \pi\frac{\theta_{fov}^2}{4}b_{max} \tag{4.16}$$

where $\delta\psi$ is the instrument phase tolerance, θ_{fov} is the angular field of view, and b_{max} is the longest baseline length. Subbing in ICEBEAR-3D terms $\delta\psi = 1°$ and $b_{max} = 34\lambda$ gives a maximum angular field of view of 1.46°, which is far too narrow compared to the extended targets associated with E region scatter. In experimentation with regridding it was found that target angles of arrival would become unpredictable as the extent of the target increased. Strategies such as mosaicing are able to create wide field of view images by moving a smaller field of view about the sky and stitching the resulting images together. This is not an effective solution for ICEBEAR-3D, as the targets change rapidly over the whole field of view.

ICEBEAR-3D has a very wide field of view requirement, thus the normalization term, $1/\sqrt{1-L^2-M^2}$, cannot be considered constant. Nor can the w terms be neglected entirely, as the array is not perfectly planar due to ground height difference. E region scatter instabilities are volumetric and cannot be considered as coming from a single plane, which is another assumptions the vCZ makes. ICEBEAR-3D images targets at low elevation angles which produces large errors when using the direction cosines since they range from -1 to $+1$, and these targets evaluate beyond this region, i.e., the Cartesian transform does not automatically fulfill the dispersion relation $k^2 = \omega^2/c^2$ Carozzi (2015). E region targets tend to be spatially extended resulting in spatially coherent targets, which is in opposition of yet another vCZ assumption. Orientation of the direction cosine plane cannot be adjusted as there is a limitation of antennas, and regridding methods induce far too much error. In summary, ICEBEAR-3D has four problems when developing an adequate transform:

1. extended source target,
2. extremely wide field of view,
3. non-planar geometry, and
4. low elevation angles.

All of which the Cartesian basis vCZ is unable to manage. The solution to all four problems is to re-derive the vCZ in spherical coordinates without assuming a zenith phase reference position (Carozzi, 2015). This is the Spherical Wave Harmonic Transform.

4.4 The Spherical Wave Harmonic Transform

Carozzi and Woan (2009) extended the vCZ to non-coplanar arrays and wide fields of view, then subsequently generalized the relationship between brightness and visibility to any arbitrary domain using a special case of the spherical Fourier-Bessel transform (Carozzi, 2015). This method, known as the Spherical Wave Harmonic Transform (SWHT), allowed: non-coplanar arrays phased in arbitrary directions, wide fields of view, imaging of extended source targets, and does not arbitrarily exasperate the low elevation angle problem. The following, is the formulation presented by Carozzi (2015). The SWHT solution begins by noting that Equation 4.14 does fulfill the Helmholtz equation in the visibility domain

$$\nabla^2 V_i(\vec{k}, \vec{b}_i) + k_0^2 V_i(\vec{k}, \vec{b}_i) = 0 \tag{4.17}$$

where V_i is the visibility for the i^{th} antenna pair, $\vec{b}_i$ is the baseline for that visibility measurement, k is the wave vector and k_0 is the wavenumber. The Helmholtz equation is solvable in spherical coordinates, thus there is a vCZ relation in terms of eigen functions of the spherical wave equation.

Beginning by applying plane wave decomposition (Jackson, 1999),

$$e^{-j\vec{k}\cdot\vec{r}} = 4\pi \sum_{l=0}^{\infty} \sum_{m=-l}^{l} (-j)^l J_l(k_0 r) Y_{lm}(\Theta, \Phi) Y_{lm}^*(\theta, \phi) \tag{4.18}$$

where now l and m are not the direction cosines, but the Spherical Harmonic Function $Y(l, m)$ degree l and order m, and $J_l(k_0 r)$ is the Bessel function of the first kind. Additionally, (r, θ, ϕ) visibility spatial frequency coordinates (u, v, w) in spherical coordinates and (Θ, Φ) are viewing angles to the celestial imaging sphere. Inserting Equation 4.18 into Equation 4.14 and expanding the brightness distribution into spherical coordinates as well, while also expanding the visibility distribution into spherical coordinates and using the orthogonality relationship of spherical harmonics then summing over all antenna pairs i, gives

$$B(\Theta, \Phi) = \sum_{l=0}^{\infty} \sum_{m=-l}^{l} b_{lm} Y_{lm}(\Theta, \Phi) \tag{4.19}$$

$$\tilde{v}_{lm}(k_0) = \frac{2k_0^2}{\pi} \sum_{i=1}^{Q} V_i(k_0) J_l(k_0 r_i) Y_{lm}^*(\theta_i, \phi_i) \tag{4.20}$$

where b_{lm} and $\tilde{v}_{lm}$ are related to each other by,

$$b_{lm} = \frac{\tilde{v}_{lm}}{4\pi(-j)^l} \tag{4.21}$$

From Equations 4.21 it is evident that there is a simple proportionality relationship between the visibility and brightness distribution. Combining Equation 4.21 with Equation 4.19 which shows the relation between multipole moments and the brightness map, and Equation 4.20 which is the visibility distribution gives

$$B(\Theta,\Phi) = \sum_{l=0}^{\infty}\sum_{m=-l}^{l} Y_{lm}(\Theta,\Phi)\frac{k_0^2}{2\pi^2(-j)^l}\sum_{i=1}^{Q} V_i(k_0)J_l(k_0 r_i)Y_{lm}^*(\theta_i,\phi_i) \tag{4.22}$$

The final output brightness $B(\Theta,\Phi)$, for a given view angle (Θ,Φ) where Θ is the elevation view angle and Φ is the azimuthal view angle, is determined by transforming the visibility values V_i, where the summation index i is per interferometer antenna pair, through the discrete summation of Bessel functions of the first kind J_l, and spherical harmonic functions Y_{lm}, where l and m are the harmonic order and degree. The baseline vectors u_i, v_i, w_i are given in spherical coordinates as $r_i = \sqrt{u_i^2 + v_i^2 + w_i^2}$, $\theta_i = \arctan(\sqrt{u_i^2 + v_i^2}/w_i)$, and $\phi_i = \arctan(v_i/u_i)$ and $k_0 = 2\pi/\lambda$ is the radar wavenumber. Q is the number of visibility quantities from the baselines, which is 91 in the case of ICEBEAR-3D. The maximum spherical harmonic order is determined from Janke and Emde (1945) as the integer evaluation of

$$l_{max} = [2\pi b_{max}] \tag{4.23}$$

For the ICEBEAR-3D receiver antenna array reconfiguration, the maximum baseline length is 34λ giving $l_{max} = 213$. In practice, it is found that higher harmonic orders will begin to overfit to noise. The standard practice is to choose the largest harmonic order that corresponds to a brightness map which does not substantially change from the brightness map of the previous harmonic order. A harmonic order of $l_{max} = 85$ was selected for ICEBEAR-3D.

The performance of the SWHT method versus vCZ was checked by simulating a target from 0° to 20° elevation in 0.1° increments and comparing imaging results. The target simulated was completely noiseless and perfectly point-like to give the Cartesian based vCZ the best chance. The comparison showed that for all elevation angles, the SWHT performed better, by as much as 2.5°. The results are shown in Figure 4.4. Most real targets are found between elevation angles 2° and 16°. The Earth occludes the transmitter line of sight below 2° for all

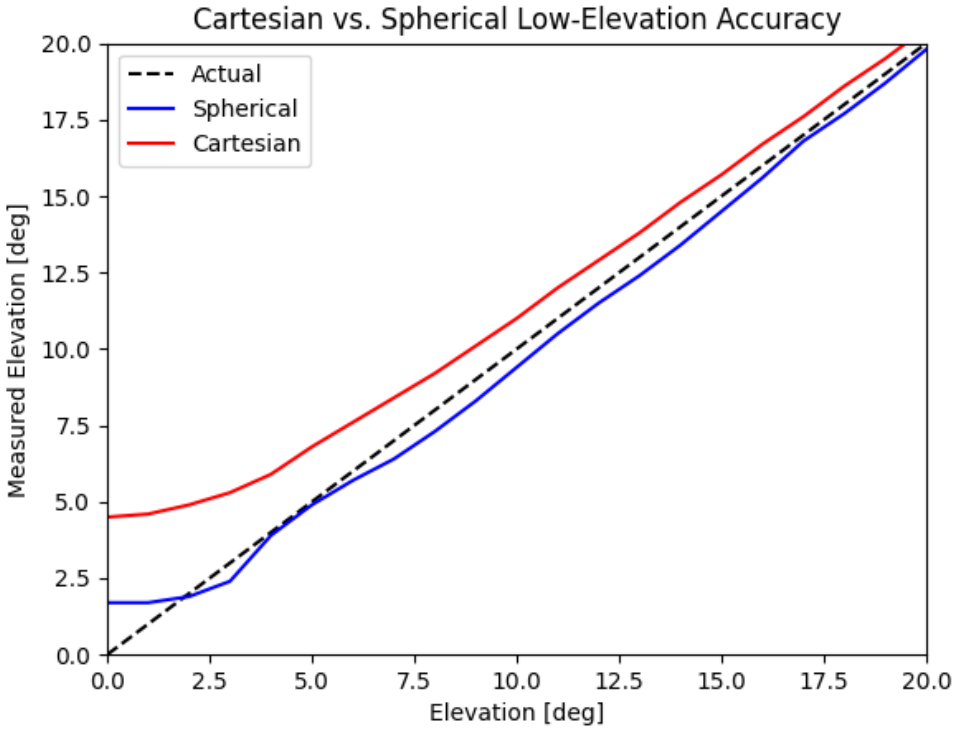

Figure 4.4: Plot of the simulated elevation angle result versus the actual elevation angle. The dashed line is the expected result, red is the vCZ (Cartesian) result, and blue is the SWHT (Spherical) result. The figure shows that in the region of interest 2° to 20°, the SWHT is always more accurate.

but the shortest of links, and above 16° targets becomes sparse. At $\approx 30°$ the two methods converge and provide no difference in results. However, with extended targets, the Cartesian based vCZ is significantly less performant. The elevation error, which is discussed in detail in Chapter 5, is not present when using the simulator. The code used to simulate targets can be found in Appendix C.

4.5 Transform Processing Speed

The 200,000 ICEBEAR-3D range-Doppler bins containing 91 visibility samples each, and each bin is a possible image ICEBEAR-3D can produce per second. It is not possible to compute 200,000 per second using the standard SWHT without sufficiently powerful computer hardware. Expanding from Carozzi (2015), the SWHT can be improved to be more com-

putationally efficient. Since, ICEBEAR-3D is a narrow bandwidth spread spectrum radar with a constant center frequency, the wavelength and thus the wavenumber k_0 only varies by the Doppler range ±500 Hz, which is essentially constant for the purposes of imaging. This allows for pre-processing of a set of transform coefficient matrices from Equation 4.22

$$C_i(\Theta, \Phi) = \frac{k_0^2}{2\pi^2(-j)^l} \sum_{l=0}^{\infty} \sum_{m=-l}^{l} Y_{lm}(\Theta, \Phi) J_l(k_0 r_i) Y_{lm}^*(\theta_i, \phi_i) \tag{4.24}$$

where $\mathbf{C}$ is a 3-dimensional matrix made from the set of $C_i(\Theta, \Phi)$ 2-dimensional matrices from $i = 1 \rightarrow Q$. To clarify, matrix $\mathbf{C}$ has the dimensions of the number of Θ angles by Φ angles by Q baselines. For ICEBEAR-3D the required field of view is ±45° azimuth and horizon to 45° elevation at 0.1° resolution, which fully encompasses the region of interest. Thus, to generate C_i from Equation 4.24 a matrix is preallocated with the dimensions of azimuth angles by elevation angles by antenna pairs, then processed up to the l_{max}. The matrix $\mathbf{C}$, with shape [900, 450, 91], is stored in memory, incrementally denoted as $\mathbf{C}_l$, for every value of l. This pre-calculation allows for much quicker image computation by only needing to directly apply the set of visibility values as a vector to their corresponding coefficient matrices and summing to make a 2D brightness map at the l harmonic of $\mathbf{C}_l$

$$\begin{aligned} \mathbf{B}_l(\Theta, \Phi) &= \sum_{i=1}^{Q} \mathbf{C}_{i,l}(\Theta, \Phi) V_i(k_0) \\ \mathbf{B}_l(\Theta, \Phi) &= \mathbf{C}_l \cdot \vec{V} \end{aligned} \tag{4.25}$$

which is identical to Equation 4.22. Using $l_{max} = 85$, this generates the standard SWHT brightness map. The pre-calculation of $\mathbf{C}$ takes considerable time, but as it is unchanging it reduces transform computation time by a factor of 10^5. The code to produce the coefficient matrices $\mathbf{C}_l$ is given in Appendix D. The average time to fully process a set of visibilities into a standard 900x450 pixel (0.1° per pixel) image using this method is 30 ms on average on an Intel Core i7-9700K CPU at 3.60GHz. On an NVidia RTX 2080 GPU this processing time is reduced by an order of magnitude to 0.26 ms on average.

4.6 The Suppressed-SWHT Method

Dirty beam artefacts introduced by the undersampled visibility domain are suppressible by deconvolution of the brightness map with the dirty beam (Thompson et al., 2001). Neverthe-

less, this is impractical for ICEBEAR-3D due to image size and quantity. Several techniques, Capon, CLEAN, and MaxENT, as previously discussed exist, but these methods typically require very narrow fields of view, point-like targets, and are computationally intensive. The Suppressed-SWHT technique, is computationally efficient as it is based on multiple applications of the SWHT, which is inherently adequate for wide fields of views and extended targets. Multiplication of brightness maps produced at lower maximum harmonic orders with higher maximum harmonic order brightness maps suppresses artefacts and noise. The suppressed brightness map, $B'(\Theta, \Phi)$, is thus the product of brightness maps of various harmonic order B_l

$$B'(\Theta, \Phi) = \prod_{l}^{l_{max}} B_l(\Theta, \Phi) \tag{4.26}$$

Since $\mathbf{C}$ is already calculated for all harmonic orders below the selected l_{max} during the pre-calculation period, there is no additional pre-processing required to obtain lower harmonic coefficient matrices provided they have been retained. For ICEBEAR-3D $\mathbf{C}_l$ uses $l = 15, 25, 35, 45, 55, 65, 75, 85$ as it was found that this limited set is computationally efficient without a loss in angle of arrival accuracy. Thus, Suppressed-SWHT 2D brightness maps for ICEBEAR-3D are formed from Equation 4.25 and 4.26

$$\mathbf{B}' = \prod_{l=15,25,35,\ldots}^{85} \mathbf{C}_l \cdot \vec{V} \tag{4.27}$$

This makes the Suppressed-SWHT roughly 10x slower than the base SWHT. The GPU implementation however optimizes processing by cleverly expanding all the coefficient matrices into one large matrix and repeats the visibility vector into a larger coefficient matrix length matching vector then performing a simple dot product, exploiting the GPU's strengths. This produces runtimes of 12 ms on average on an NVidia RTX 2080 GPU.

This suppression comes with a trade-off. Spatial extent information of the target and other targets of lower power within the same brightness map are likewise suppressed. Even though spatial extent information is suppressed in the Suppressed-SWHT image, the detection and location of the extended target is not, in fact it is accurately discernible, and extent information is recoverable from measuring the spatial coherence (Huyghebaert et al., 2021). The suppression of lower power targets is acceptable as it is assumed typically only one target should exist per brightness map because each brightness map only represents the full field of view at one specific range bin and one specific Doppler bin (a single range-Doppler bin) in 1 s. This makes the likelihood of multiple targets with the same velocity and the same range, which are also spatially incoherent and separate in elevation or azimuth, unliekly.

An example image processing for a real target seen in one 1.5 km range bin, for one 10 Hz Doppler bin, over 1 s is shown in Figure 4.5. The top of Figure 4.5 shows the unsuppressed brightness map $\mathbf{B}_{85}$ with a target at $\Phi = -15.0°$ azimuth and $\Theta = 9.8°$ elevation. Artefacts within the unsuppressed brightness map have brightness values at $\approx 60\%$ the normalized maximum brightness. These are removed from the bottom image $\mathbf{B}'$ by application of the Suppressed-SWHT method.

Figure 4.6 shows a simulation where two targets are presented with different powers in the same range-Doppler bin. This shows multiple targets per brightness map may exist and are discernible, however the Suppressed-SWHT has eliminated the lower power target. In a future study the comparison of the Suppressed-SWHT to other synthesis aperture imaging deconvolutional methods such as Capon's, CLEAN, and MaxENT, is planned to obtain extent information and resolve the extremely unlikely situations of multiple targets per brightness map. The Suppressed-SWHT technique results in a well-defined target for angle of arrival determination. The simulator used can be found in Appendix C.

ICEBEAR-3D sets the brightness map field of view to $\pm 45°$ azimuth from boresight and $0°$ to $45°$ in elevation at $0.1°$ resolution producing high resolution 900x450 pixel images for each range-Doppler bin for each second. As such, ICEBEAR-3D obtains a $0.1°$ angular resolution with a 1.5 km range resolution, giving on average over the typical 300 km to 1100 km slant ranges a spatial resolution bin of 1.5 km x 1.5 km x 1.5 km.

4.7 Target Acquisition

Target acquisition with an image is a multistep process. All targets are firstly imaged with a coarse $1°$ resolution Suppressed-SWHT coefficient matrix. The absolute maximum value point in this image is taken as the true angle of arrival. If the target is located within the field of view further processing is done, if it is not the angle of arrival is recorded and flagged as errant. Targets inside the field of view are then processed with the $0.1°$ SWHT and Suppressed-SWHT coefficient matrices to form $\mathbf{B}_{85}$ and $\mathbf{B}'$ respectively. Then ICEBEAR-3D uses image processing techniques to find the contour of the target in $\mathbf{B}_{85}$ which encloses the location of maximum brightness found in $\mathbf{B}'$. From the contour, the location of the local maximum brightness is found. This location corresponds to the angle of arrival of the received signal.

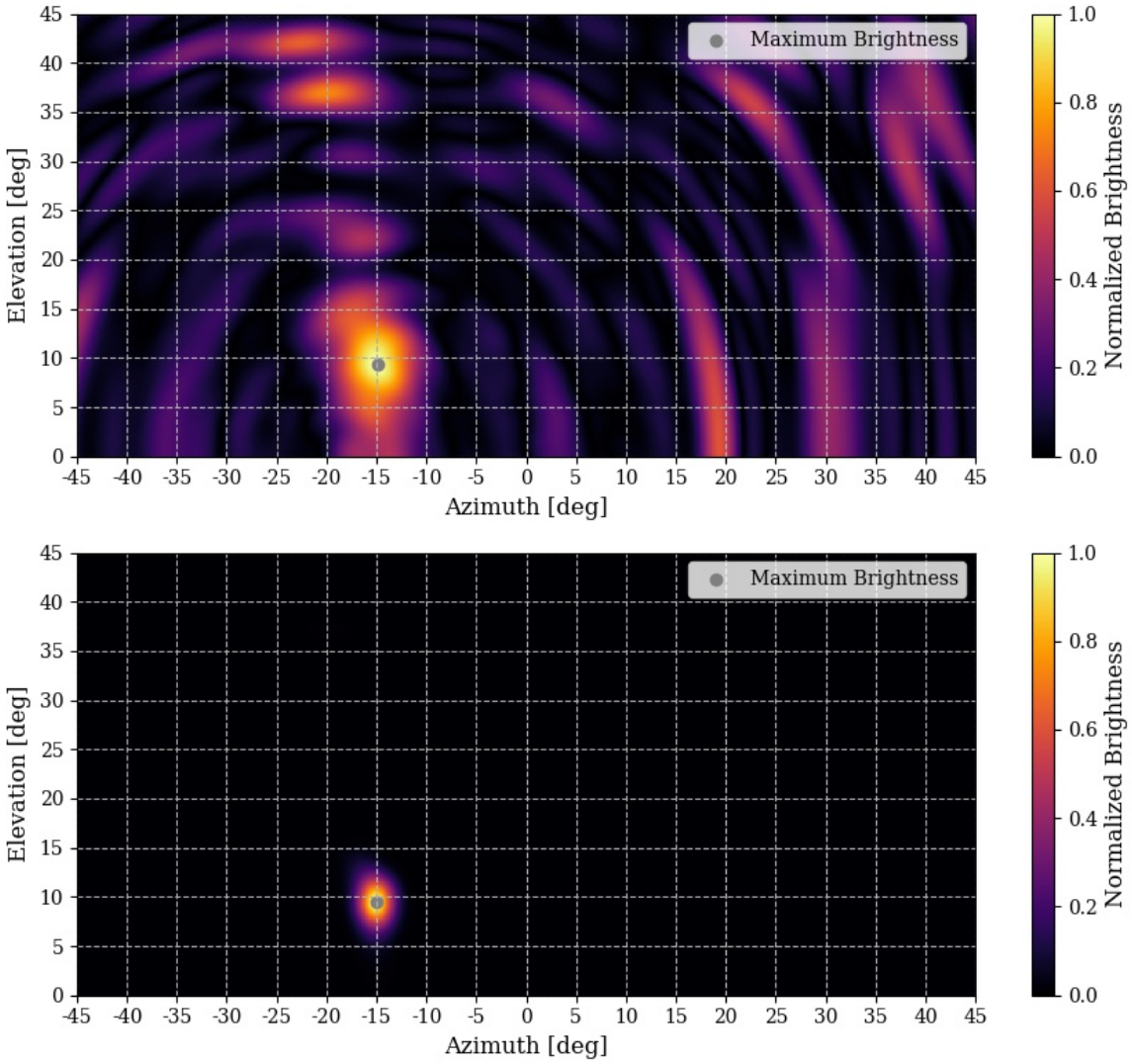

Figure 4.5: (Top) Brightness map $\mathbf{B}_{85}$ containing a target created using the SWHT method with pre-calculated coefficients up to $l_{max} = 85$. The brightness maps are 900x450 pixels corresponding to a 0.1° resolution with azimuth field of view of ±45° and elevation field of view from 0° to 45°. The target is located at $\Phi = -15.0°$ azimuth and $\Theta = 9.8°$ elevation. (Bottom) The same brightness map with Suppressed-SWHT applied at harmonic steps of 10 from $l = 5$ to $l = 85$, resulting in a well-defined target location with artefacts suppressed.

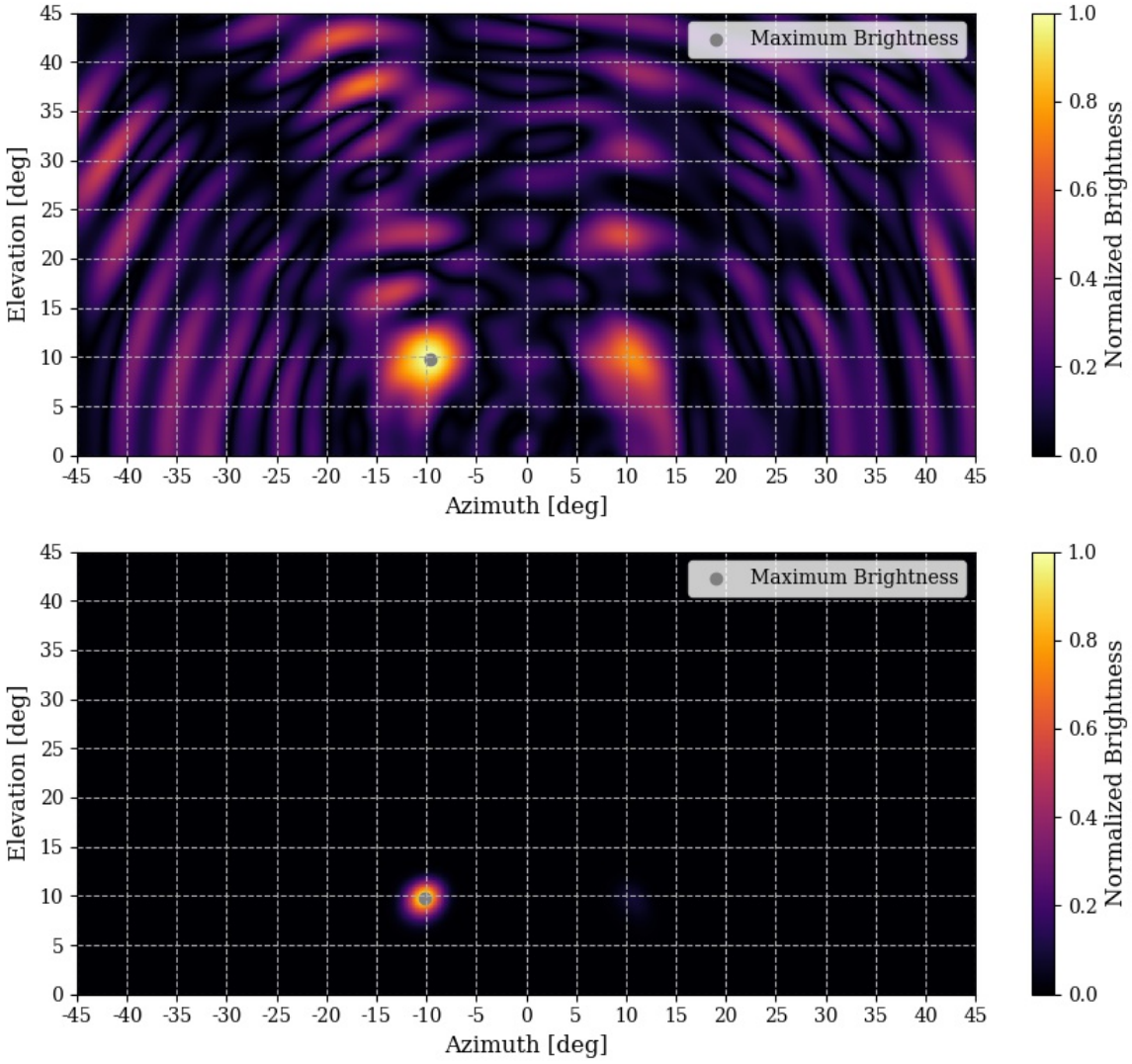

Figure 4.6: (Top) Brightness map $\mathbf{B}_{85}$ containing two targets created using the SWHT method with pre-calculated coefficients up to $l_{max} = 85$. The brightness maps are 900x450 pixels, corresponding to a 0.1° resolution with azimuth field of view of ±45° and elevation field of view from 0° to 45°. One target is located at $\Phi = -10.0°$ azimuth and $\Theta = 10.0°$ elevation the other target at 3/4 power is at $\Phi = 10.0°$. (Bottom) The same brightness map with Suppressed-SWHT applied at harmonic steps of 10 from $l = 5$ to $l = 85$, resulting in a well-defined target location with artefacts and the lower power target suppressed.

The elevation and azimuth angles of arrival found through imaging are with respect to the receiver antenna array. Using them along with the slant range as the bearing and heading, the geographic location of targets are determined. With the nascent ICEBEAR-3D imaging radar using the novel Supressed-SWHT to its first radar targets, it quickly found that there was an inconsistency in elevation. Elevations were increasing with slant range. This error could not be explained by any error in imaging, target acquisition, array design, or operations. Yet, it would persist, but only with real targets and never simulated ones, and unlike past radar the elevations would be tightly packed into a thin layer rather than dispersing with slant range. This illuminated the long standing problem with radar interferometer elevations and led to a solution.

5 Elevation Angles

Section 5.3 of this chapter contains in part works directly from my contributions in Lozinsky et al. (2022).[1]

Past radars studying targets at low elevation angles have typically seen elevation angles become erratic, dispersing with slant range, and trending to increase in altitude with increasing slant range as elevation angles become lower, most notably by Ierkic et al. (1992) and Sahr et al. (1991). This is the long standing problem of low elevation radar interferometry that is not unique to just E region radars (White, 1974; Barton, 1974; Kerr, 1951). The poorly grouped or erratic results leads naturally to the conclusion that there must be phase errors and/or incorrect calibrations. The phase tolerant design of ICEBEAR-3D allowed for elevation angles to be measured with consistent accuracy, resolving erratic measurements, keep elevation angles well grouped into a thin ribbon. The underlying nonphysical trend of targets rising higher as elevation angles lower is unmistakable.

Figure 5.1 shows ICEBEAR-3D observations of the Geminid meteor shower collected from 12 to 15 December 2020. The radar ran from 00:00 UT to 14:00 UT (6:00 pm to 8:00 am local time) each day. The period was very geomagnetically quiet (Kp of 0.0 to 1.7) and only meteor trails were observed. Under these nighttime conditions, there will be no refraction at the ICEBEAR radar operating frequency of 49.5 MHz. During this period, ICEBEAR-3D observed $\sim 60,000$ meteor trails, at an average rate of about 1 meteor trail observation every 4 s. It is well known from upward looking radars that meteor trails are observed typically at altitudes from 70 km to 110 km (McKinley, 1961). The top plot in Figure 5.1 clearly indicates the expected thickness of $\sim$ 40 km for meteor trail observations; however, the altitude of this layer unrealistically increases with increasing slant range, which is nonphysical. This unmistakable curving upwards, which is not hidden by erratic measurements, sheds new

[1] Lozinsky, A., Hussey, G., McWilliams, K., Huyghebaert, D., and Galeschuk, D. (2022). ICEBEAR-3D: A Low Elevation Imaging Radar Using a Non-Uniform Coplanar Receiver Array for E Region Observations, *Radio Science*, 57(3). DOI: 10.1029/2021RS007358

light on the low elevation problem. One can observe that the radius of curvature of this curve is nearly the radius of the Earth R_E. This clearly should not be the case, rather, it should be a flat layer like the bottom plot of Figure 5.1. This curving upwards is caused by improper interpretation of the geometry for vertical interferometry. When the proper geometry for vertical interferometry is applied, then elevation angles — even low elevation angles — resolve physically and correctly as shown in the bottom plot of Figure 5.1.

The chapter discusses the proper geometry interpretation for vertical interferometry. Investigation into the long standing low elevation problem is difficult, as literature on this effect is underreported. The problem is one of common knowledge within the radio signal propagation community, but is typically avoided. In order to verify that the problem was not an artefact of misconfigured hardware or software, a rigorous validation test was performed. This validation is first presented to establish confidence in the instrument. Next, a myriad of alternative explanations and corrections is presented. Ultimately, these alternative solutions failed to account for the elevation difference between physical and measured. Subsequently, this chapter focuses on the explanation of the proper geometry interpretation for vertical interferometry, which leads to the high quality and accurate altitude measurements shown in Figure 5.1.

5.1 Hardware and Software Validation

Elevation angles are phase and baseline dependent, as these values are related to the propagation difference between a signal arriving at two antennas of an interferometer. The location of the as built ICEBEAR-3D antennas were confirmed using GPS surveying equipment as well as a theodolite. The design of the receiver antenna array discussed in Chapter 3 allows for a 25 cm antenna location error. The GPS surveying equipment registered a 50 mm precision when the measurements were performed during construction in summer 2019. The antenna locations are accurate, but their heights are less well known. Heights were measured by adding the height of the tower, which the receiving antenna sits upon, to the ground height measured by the GPS total station surveyor. There is an unknown amount of height error, which equates to an unknown amount of error in the w terms. The imaging celestial sphere is orientated with respect to the antenna locations, and error in the w term acts to rotate the equatorial plane of the imaging celestial sphere. Although the w offsets measured are relatively small compared to the signal wavelength, such that the ICEBEAR-3D receiver

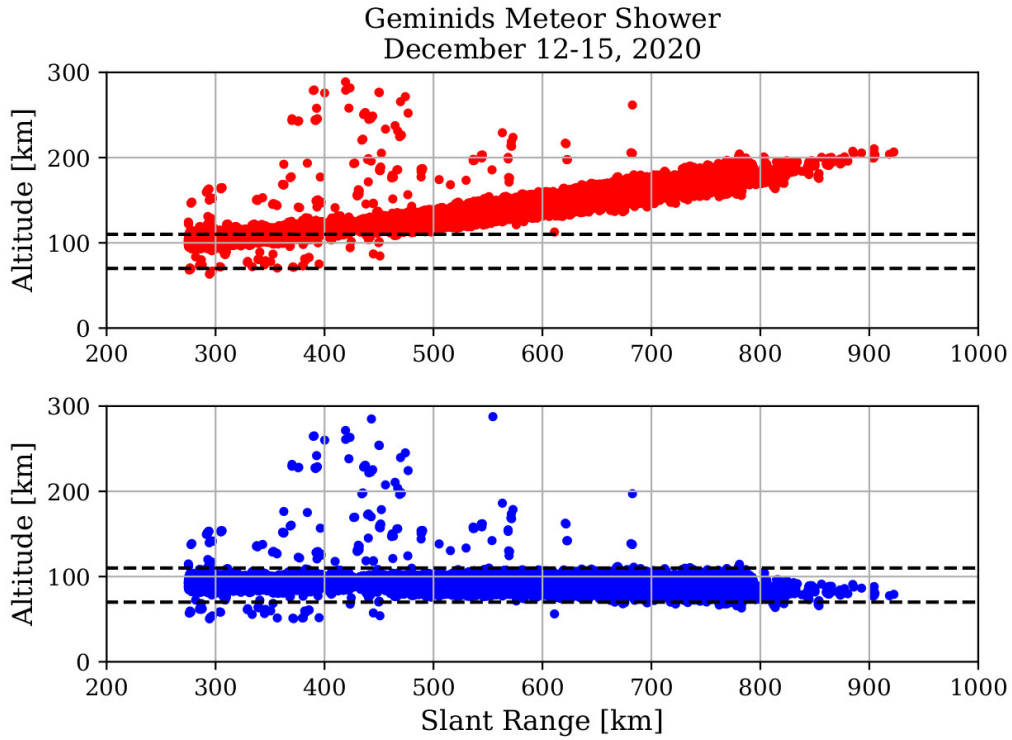

Figure 5.1: ICEBEAR-3D observations of the Geminid meteor shower from 00:00 UTC to 14:00 UTC daily from 12-15 December 2020. This was a geomagnetically quiet period which observed $\sim$ 60,000 meteor trails (on average about 1 meteor trail every 4 s). (Top) Altitude of meteor trails calculated using conventional geometry for elevation angle vertical interferometry determination. (Bottom) Same ICEBEAR-3D data as presented in the top plot, except now the geocentral geometry for elevation angle vertical interferometry determination, as described in the text and Figure 5.6, has been taken into account. Now all the meteor trail observations are between 70 km and 110 km (black dashed lines) as expected, and do not unrealistically increase in altitude with range.

antenna array is often considered co-planar, their effect was checked. The w offsets were checked by fitting a plane to the antenna locations, then elevation and azimuth offsets between this plane and the equator of the imaging celestial sphere were found. These elevations and azimuth offsets were found to be minimal, causing no significant change in the results; also they are constant offsets which cannot account for the growing elevation angle with slant range, as it is not a simple linear change. Furthermore, artificially setting all w terms to zero and collecting data from imaged meteor trail targets does not significantly change results. Therefore, the antenna location measurements are considered accurate.

Signals arriving at the receiver antennas run through lengths of cable and pass several RF devices. The unique noise signal generated by the celestial body Cygnus A is measurable with ICEBEAR-3D. Galeschuk (2021) showed that ICEBEAR-3D can track Cygnus A as it crosses the sky. The unique Cygnus A signal was seen on all antennas, verifying that each channel was functioning. This total path length, or feedline, is slightly different per antenna. The phase delay caused by these paths was accounted for by manual calibration. This reduces the phase error caused by the different paths to less than 1°, which is well below the array's designed 14.86° phase measurement error tolerance. This manual calibration is done using a Vector Network Spectrum Analyzer to measure the magnitude and phase of each channel from the X300 SDR to the antenna. Then the magnitude and phase are normalized to Antenna 0 to generate a set of calibrations. The calibrations are then subtracted from the raw complex IQ voltage samples. The voltage samples for each antenna were compared to each other to ensure they were realistic quantities.

A chip delay is caused by the X300 SDR clock becoming skewed and undisciplined. When an X300 SDR loses synchronization, the signals sampled are displaced temporally. This acts to shift the PRN in time, and this shift is called chip delay. The matched filtering processing then generates either an early detection when synchronization is forward shifted, or late detection when reverse shifted (Richards et al., 2010). These early and late detections cause the targets to appear in the wrong ranges bins, either slightly closer or farther, respectively. Each X300 SDR has 2 channels, so a chip delay would systematically bias the results of those two channels, affecting multiple baselines. A 70 ns early chip delay on the farthest two Southern antennas would be required to lower the measured elevations by 6°, which would correct targets at the farthest ranges but over correct closer ranges. The X300 SDRs are time disciplined by a 10 MHz GPS synchronized reference signal, which prevents chip delay, and samples at 200 Msps (one sample every 5 ns). Accounting for a 70 ns chip delay did not remove the elevation error.

A full receiver side system validation, which includes all hardware and software elements from the antenna through Level 1 data processing, was performed by checking the closure relationship. The closure relationship states that the summation of the phases for any three antennas observing a point source in the far-field will equal zero (Thompson et al., 2001). Consider antennas A_1, A_2, and A_3 in Figure 5.2, with antenna separation vectors d_{12}, d_{23}, and d_{31} forming a triangle. The phase differences between each antenna are then ψ_{12}, ψ_{23}, and ψ_{31}, and the phase errors on each antenna are ψ_1, ψ_2, and ψ_3. The sum of the phases ψ_{123} is the closure angle and is given by

$$\psi_{123} = (\psi_1 - \psi_2 + \psi_{12}) + (\psi_2 - \psi_3 + \psi_{23}) + (\psi_3 - \psi_1 + \psi_{31}) \tag{5.1}$$

$$\psi_{123} = \psi_{12} + \psi_{23} + \psi_{31}$$

where the phase errors from each antenna nominally cancel out. Inserting this result into Equation 3.1, the basic interferometer equation gives

$$\psi_{123} = \frac{2\pi}{\lambda}(\vec{d_{12}} + \vec{d_{23}} + \vec{d_{31}}) \cdot \vec{s} \tag{5.2}$$

where $\vec{s}$ is the direction of the incident wave from a point source. For a perfect phase calibration, the vector summation of the antenna separations forming a triangle must sum to zero. Therefore, the summation of the phases must also equal zero, regardless of the direction of $\vec{s}$. In the real world, however, the closure angle is rarely zero. Yet, a nearly zero result indicates that the instrument is well calibrated. For ICEBEAR-3D $n = 10$ antennas there are $n(n-1)(n-2)/6 = 120$ unique combinations of three antennas and each antenna appears $(n-1)(n-2)/2 = 36$ times in the set. Using meteor trail targets, which are point like, the closure angles were checked for each combination and each closure angle for ICEBEAR-3D was within $\pm 5^\circ$ of 0°. With this analysis, hardware and Level 1 processing were eliminated as potential causes of the elevation problem.

Image processing of data from Level 1 to Level 2 using the Suppressed-SWHT method couples the azimuth and elevation angles of arrival, as they are both derived from the same set of visibilites. Any significant errors will cause sporadic results in both elevation and azimuth. During the elevation error investigation, it was noted that the targets were correctly azimuthally located. Notably, systematic software errors such as a 180° phase rotation, -1 error inverting all antenna locations, misaligned coordinates basis, or reversing cross-correlations, simply rotated the final results azimuthally while causing no elevation changes. After an extensive code review, these systematic errors were removed and the data was cor-

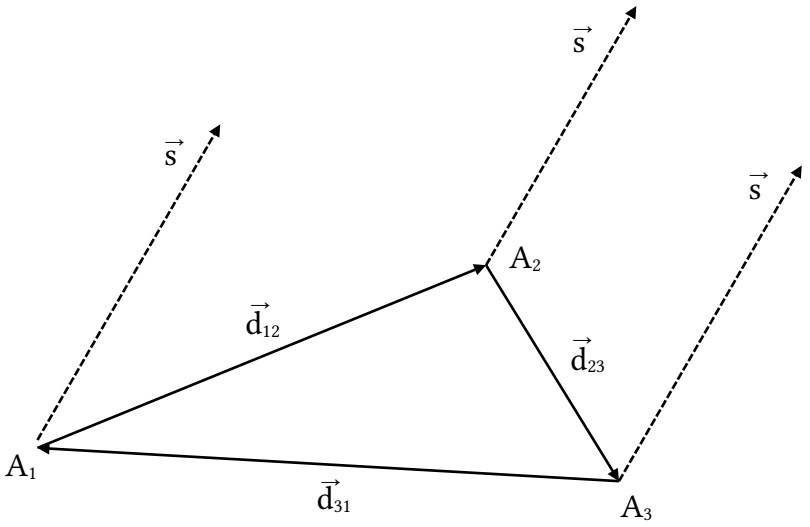

Figure 5.2: Closure angle triangle. Antennas A_1, A_2, and A_3 for a triangle with baseline vectors d_{12}, d_{23}, and d_{31}.

rectly oriented, so the imaging celestial sphere was orientated with 0° azimuth pointing 7° East of North along the horizon. This eliminated the notion that the elevations were simply due to a rotated reference frame. Using the simulator described in Chapter 4, simulated targets with programmable spatial extents and angles of arrival were created. These simulated targets were processed using the same processing chain real data used. All the simulated targets were accurately located, and no elevation errors were detected. Simulated targets did not rise in elevation with increasing slant range. The simulator, however, did not include a ground plane. To take into account the contribution of the signal which reflects off the Earth's surface, the method of images was used to simulate a ground plane. All simulations were performed again with the simulated ground plane and there was no change, simulated targets did not show the elevation problem. This was expected, as the result from Equation 3.10 $S_1 S_2^* = 2|A|^2 e^{jk_0\Delta}$, showed that the combination of a direct and reflected was to only double the power of the signal received. This both validated the software and suggested that the source of the elevation error was physical, but not due to the radar itself.

5.2 Alternative Corrections

Completing a thorough check of the radar system, from hardware through software, lead to the conclusion that elevation error must be occurring due to an unaccounted for physical effect. The search was exhaustive; however, only the most reasonable alternatives: refraction, glint, and reflections, are discussed here. Additionally, an empirical correction was attempted.

5.2.1 Refraction

Refraction occurs when electromagnetic waves pass through mediums of differing density. The plasma of the terrestrial ionosphere causes bending of radio waves, but it is a frequency dependent process. At 49.5 MHz, straight line propagation is expected at all times except during high levels of activity where the E region is heavily ionized (Hussey, 1995). A custom simple ray tracing refraction model (see, Appendix E) was developed that generates a linear electron density gradient from 80 km to 120 km. The model estimated the index of refraction n from the electron density N_e using the Appleton-Hartree dispersion relation in the approximated form

$$n = \sqrt{1 - \frac{81 N_e}{f^2}} \tag{5.3}$$

where f is the radar frequency (Kivelson & Russel, 1995). The model applied Snell's law to simulate the rays bending. The peak electron density was adjusted until the rays were completely refracted, such that a target at 900 km slant range was detected 80 km higher than actual. This is the electron density required to explain the amount of elevation bending observed. This amount of bending occurred at an electron density peak of 30×10^{12} m^{-3} at 115 km altitude, which is the electron density for total internal reflection $f = 9\sqrt{N_e}$, and is not physical for the terrestrial E region. Figure 5.3 shows simulated rays with elevation angles $8°, 10°$, and $12°$. The dashed blue lines are the totally reflected rays, while the solid black lines are direct line of sight rays. Applying a reasonably typical E region electron density peak of 3×10^{11} m^{-3} (Watermann, 1990) at 115 km refracted the rays very little, so little that these rays coincided with the black direct line of sight lines. The elevation upward curving with slant range was not caused by refraction, as the elevation problem existed regardless of the E region electron density, and to get the amount of bending observed required unrealistically large non-physical electron densities.

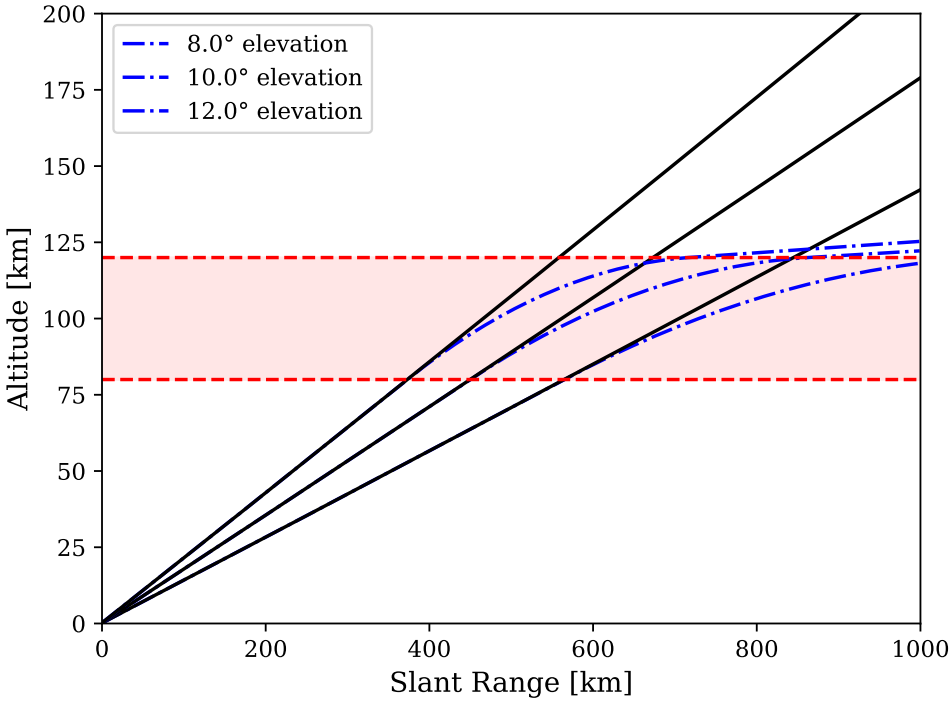

Figure 5.3: Three ray traces with elevation angles of $8°, 10°$, and $12°$. The shaded red area shows the lower E region, 80 km to 120 km. The black lines are the straight line propagation with no refraction; these lines coincide with ray traces from the ray tracing refraction model with a peak electron density of 3×10^{11} m^{-3} at 115 km altitude. At this typical density, there is no observable bending. The dashed blue lines use a peak electron density of 30×10^{12} m^{-3} at 115 km altitude. This is the electron density required for a 49.5 MHz wave to totally reflect. At this density an 80 km altitude difference is visible, which would explain the elevation error, but this is an unrealistic electron density for the E region.

5.2.2 Glint

Glint is a fluctuation of the apparent angle of the target caused by coherent scattering off a complex target. (Richards et al., 2010). These complex targets can be considered as an ensemble of point scattering targets, which act together to create the echo signal. A spatially extended target such as E region scatter is spatially coherent across its scattering cross-section and structured along the magnetic field lines. An incident radar wave striking this complex target with varied aspect angles causes variations in the orientation of the echo phase fronts, potentially causing glint. This coherency makes glint very difficult to filter for and remove. The changing orientation of the echo phase fronts from the extended spatially coherent source would be imaged as a single target with an erroneous angle of arrival. Regardless, glint is not likely the cause of the elevation problem, as it is a random process that is a function of the target rather than the instrument and ICEBEAR-3D observes a well grouped thin layer for both E region scatter targets and point-like meteor trails which would not cause glint.

5.2.3 Reflection

The Earth's surface is reflective at 49.5 MHz (Balanis, 2016). If the targets are purely reflections with no direct propagation path, which is not the case, then the elevation angles measured are negative. The imaging celestial sphere is normally computed using the upper hemisphere, but the lower hemisphere returns the same elevation angles, only negative, due to the reflection symmetry about the equatorial plane ambiguity that is only broken with longer w baselines. Altitudes are determinable using these negative elevations angles; simply assume that the targets are below the Earth's surface and apply Cosine law to determine distances they are below the surface. Then invert those distance and call that altitude. The bottom plot of Figure 5.5 from the Gemininds meter shower 12-15 December 2020 shows the difference between the proper geometry interpretation which use the geocentral angle and this below the Earth's surface alternative in red. There is minimal difference except at long ranges and high altitudes, which is not fully captured in this plot. As discussed in Chapter 3 the total signal received by an antenna is the summation of the direct and reflected signals. When the reflected signal is considered as a purely specular reflection or the direct path is significantly more powerful, the elevation determined will be with respect to the signal's direct path. This case presented would require the reflected path power to be significantly larger than the direct path; thus biasing the radar towards the reflected path.

In reality, the ground reflection plane produces diffuse reflection and is rarely more powerful than the direct path, except in cases where numerous multipath propagation reflections coherently sum, like in a parabolic reflector. A diffuse reflection has the effect of broadening the signal in elevation. They are due to the rough surfaces at the reflection point scattering the signal. This broadened area is called the *glistening surface* and is described by the divergence factor D (Richards et al., 2010).

$$D \approx \sqrt{1 + \frac{2\rho_{rp}^2(\rho_g - \rho_{rp})}{R_E \rho_g (h - (\rho_{rp}^2/2R_E))}} \tag{5.4}$$

where h is the target altitude, R_E is the radius of the Earth, ρ_g is the ground distance between the receiver and target, and ρ_{rp} is the ground distance from the receiver to the reflection point. For typical ICEBEAR-3D ranges and altitude $D \simeq 1$, meaning the reflected path does not dominate. Consider the example in Figure 5.4, a spatially extended target is imaged. The direct path arrives at 5° and the diffusely reflected path at $-5°$, albeit skewed. The resulting imaged target would be the combination of the direct and reflected path. This combination skews the elevation angle measured to larger angles. The true target elevation becomes lower to the horizon at increasing slant range, which stretches the glistening surface, causing the measured elevations to nonphysically rise. Thus, the combined direct and reflected combination target's elevation angle of arrival becomes increasingly ambiguous and biases upwards. This is unlikely the case as the solution latter presented is quite clear, however, reflections cannot be completely ruled out.

5.2.4 Empirical Fit

The most direct, albeit least satisfying way to correct the elevation angles, is to simply fit a curve to the well defined distribution of targets and correct empirically. A simple second order polynomial was found. It is shown in the top plot of Figure 5.5, and described by $f(\rho) = 8.0 \times 10^{-4}\rho^2 + 0.07\rho + 77.4$, where ρ is the slant range. The fit was done during a quiet geomagnetic period (Kp of 0.0 to 1.7) from 00:00 UT to 14:00 UT (6:00 pm to 8:00 am local time) each day between 12 and 15 December 2020. The middle plot shows two groupings of meteor trails. The red grouping is elevation corrected by treating measured elevations as pure reflection that came from under the ground, while the magenta grouping was corrected using the fit. Both methods agreed well with the accepted E region layer altitudes, laying between 70 km and 110 km. The bottom plot of Figure 5.5 is the difference of the two alternative

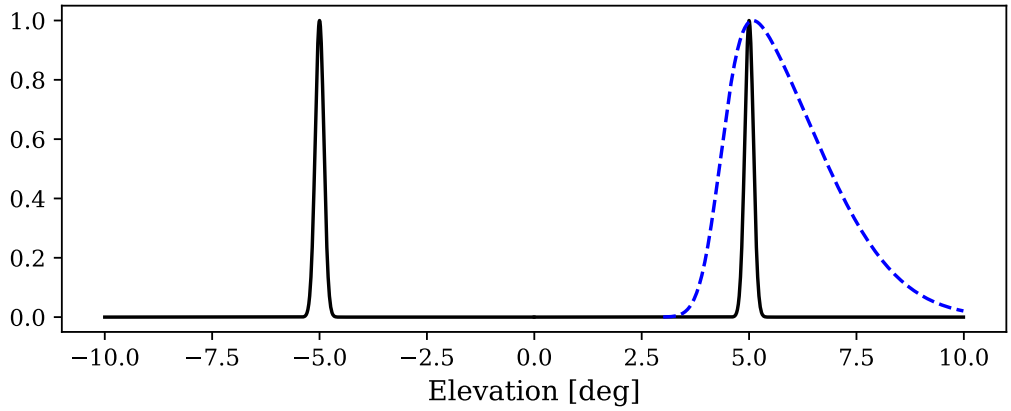

Figure 5.4: A signal with a direct angle of arrival at 5° elevation and a reflected angle of arrival of −5°. The assumed specular reflection is shown as the normal distribution as a solid black line. This matches the direct path. The diffuse reflection is shown as the dashed blue line. The target angle of arrival detected is the combination of the direct and reflected signal. The diffuse reflection becomes more skewed as the grazing angles reduces, which biases the radar to higher altitudes.

methods to the proper geometry for vertical interferometry geocentral angle calculation. The reflection correction was less effective at further ranges, but was otherwise very close. The fit correction tends towards lower altitudes and over corrected when compared to the geocentral interpretation.

The radius of curvature R_c of the fit function $f(\rho) = 8.0 \times 10^{-4}\rho^2 + 0.07\rho + 77.4$ is determined using

$$R_c = \frac{(1 + f'(\rho)^2)^{3/2}}{|f''(\rho)|} \tag{5.5}$$

At $\rho = 77.4$ km the radius of curvature R_c is 6314 km. This is very close to the radius of the Earth $R_E = 6361$ km at 60° latitude where the meteor trails used to generate the empirical fit were detected. There is no place in the processing where the radius of the Earth was used in determining the target's elevation angles; it is only used in the altitude determination and should not appear as the radius of curvature of the fit. This result clearly indicated that there was a geometric relationship was missing when determining the elevation angles and computing altitudes using the conventional Cosine law method. An analytical solution that would match the empirical fit and reflection method without having to fictitiously place the targets below the Earth's surface was needed. The remainder of this chapter is that solution.

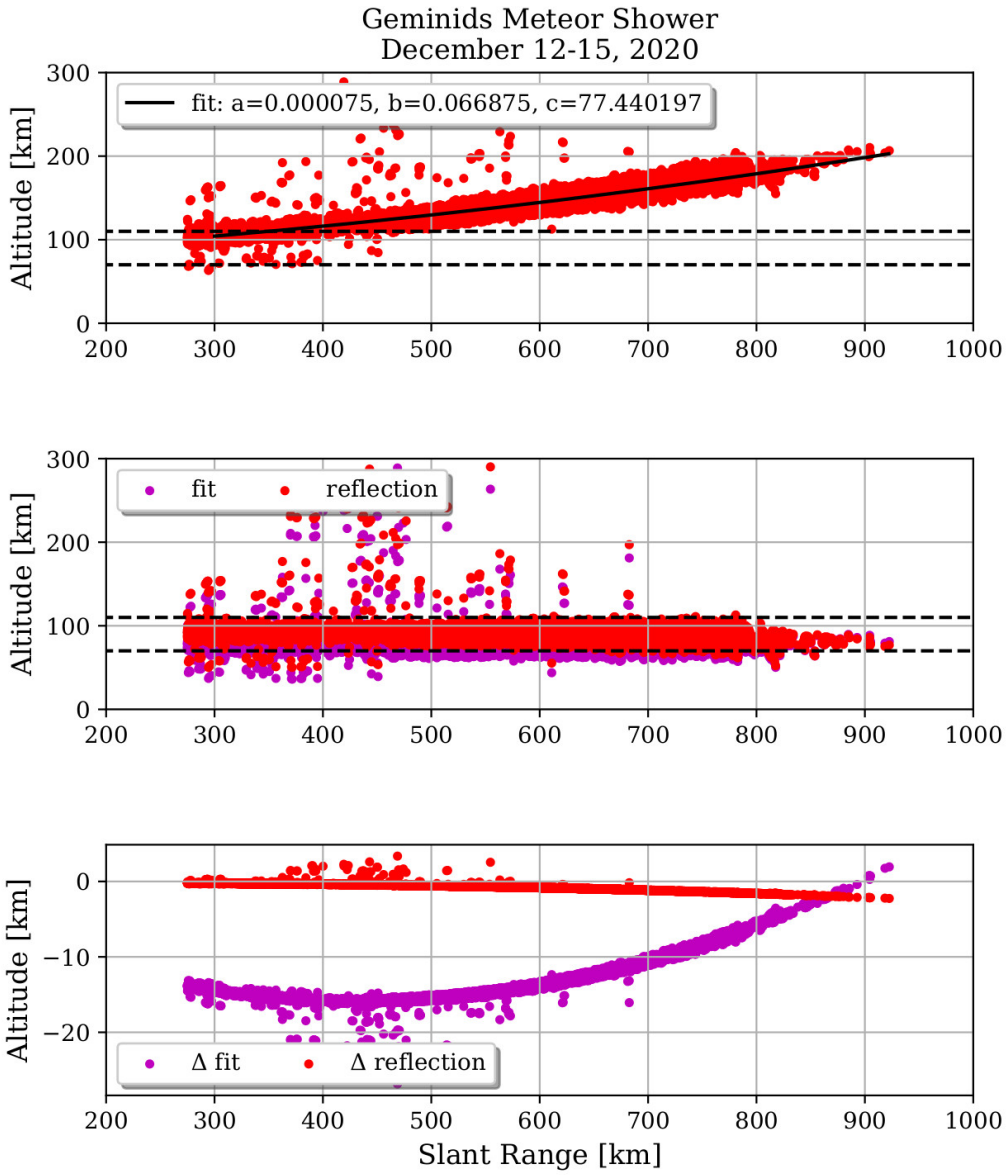

Figure 5.5: Demonstration of alternative methods to correct the long standing elevation problem. (Top) Plot showing a second order polynomial $f(\rho) = 8.0 \times 10^{-4}\rho^2 + 0.07\rho + 77.4$ fitted to the upward curving elevations. (Middle) Scatter plot of $\approx 60,000$ meteor trails from 2020 December 12-15, which have been corrected by the empirical fit and by treating the measured elevation angles as negatives angles coming from below the Earth's surface. (Bottom) The difference of the empirical fit and below surface method to the geocentral proper geometry interpretation for vertical interferometry.

5.3 The Proper Geometry for Vertical Interferometry

Although ICEBEAR-3D is a bistatic radar system, the elevation angle geometry is identical to that of a monostatic radar; it is with respect to the receiver antenna array. The following applies whether or not the vertical interferometer has a single baseline or multiple baselines. The conventional approach is to express the elevation geometry as a triangle in a vertical plane as depicted in the left diagram in Figure 5.6. The sides of the triangle in the vertical plane consists of the radar receiver slant range ρ, with the other two sides of the triangle, both measured from the center of the Earth: one, R_E, to the antenna array (point Rx) and the other, $R_E + h$, to the scattering target location (point Sx). The altitude of the scattering location is h. The angle between the Earth centered sides of the triangle, R_E and $R_E + h$, is the geocentral angle Γ, while the elevation angle α is defined with respect to the tangent plane the receiving antenna array makes with the surface of the Earth at the antenna array location and is the measurement of interest.

The normal procedure is to take the phase difference ψ between an antenna pair and apply the basic interferometer equation, presented in Equation 3.1, to determine the angle of arrival η. Solving for the angle of arrival term η and ignoring aliasing gives

$$\eta = \arccos\left(\frac{\psi\lambda}{2\pi d}\right) \tag{5.6}$$

$$\eta = \arccos\left(\frac{\psi}{k_0 d}\right)$$

With regard to the elevation angle of arrival, this interpretation is not complete. What also needs to be taken into account is the implicit assumption that the reference phase surface is a constant phase surface.

The classic Young's two-slit experiment is planar and the plane is also a constant phase surface. As the Earth is a curved surface, roughly a sphere, this defines the geometry of the reference constant phase surface with respect to the center of the Earth, which must be taken into consideration when determining the elevation angle from vertical interferometry as is shown in the right diagram of Figure 5.6. The intersection of the vertical elevation angle plane defined above, with the spherical constant phase reference surface of the Earth is an arc of a circle and therefore also a constant phase reference. The ends of this arc are defined by the pierce-points at the surface of the Earth; the first is Rx on the surface of the Earth

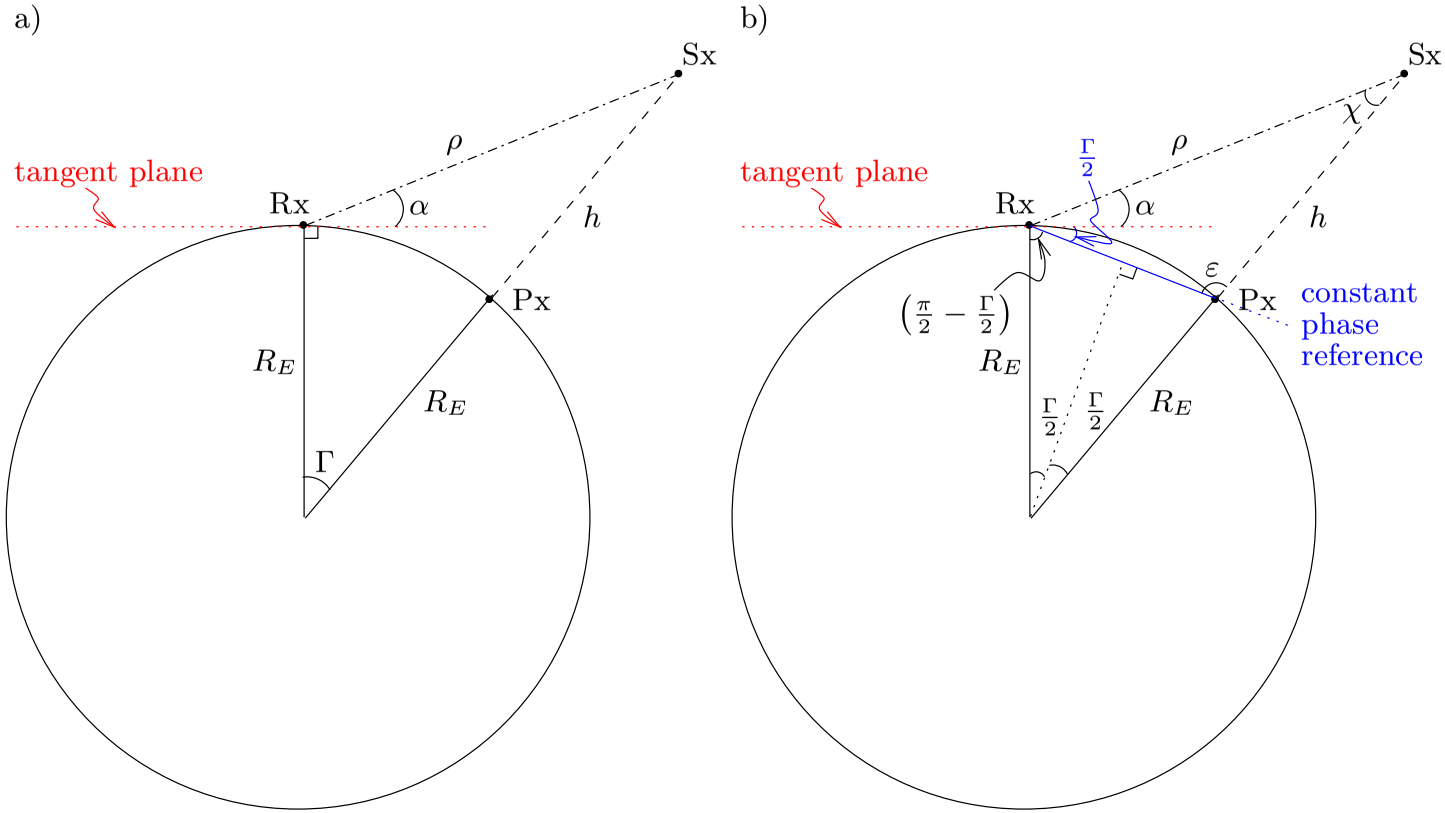

Figure 5.6: (Left) Conventional geometry for elevation angle α from vertical interferometry determination. (Right) Proper geometry for elevation angle α determination taking into account the constant phase surface, the plane containing chord/arc Rx–Px. The scatter altitude is not realistic for E region radar observations, but has been enhanced for illustration purposes.

along a line from the center of the Earth to the receiver antenna array, and the second is Px on the surface of the Earth along a line from the center of the Earth to the scatter altitude Sx.

Although the tangent plane of the receiver antenna array defines the baseline separations as described by the Young's two-slit formulation (Equation 3.1 or 5.6), the chord g joining the two pierce-points (Rx and Px) defines the phase reference orientation for the measured phase difference ψ for vertical interferometry elevation angle determination. This geometry consideration for vertical interferometry is independent of the radar wavelength and antenna baseline spacing, and is simply applying the implicit requirement in Equation 3.1; that the proper constant phase reference described by the non-planar curved geometry be taken into consideration. This complicates the geometry determination for vertical interferometry, as at different slant ranges and/or different elevation angles moves the pierce-point Px of the scattering altitude line and therefore changes the orientation of the chord.

As such, the angle η in Equation 5.6, when discussing terrestrial vertical interferometry elevation angle measurements, is actually the measurement $\eta = \beta = \alpha + \Gamma/2$, and $\eta \neq \alpha$. Additionally, the traditional presumption that the constant phase reference is with respect to the tangent plane is errant, as the constant phase reference is actually with respect to the chord which is below the tangent plane. As a result, this then adds another $\Gamma/2$ when taking the tangent plane as the constant phase reference. Consequently, Γ, the geocentral angle defined by the pierce-points Rx and Px with respect to the center of the Earth, must be subtracted from the elevation angle of arrival value β determined from the basic interferometer equation, Equation 3.1, plus the presumptive $\Gamma/2$ tangent plane reference, to get the proper elevation angle α with respect to the tangent plane

$$\begin{aligned} \beta &= \alpha + \Gamma/2 + \Gamma/2 \\ \alpha &= \beta - \Gamma/2 - \Gamma \\ \alpha &= \beta - \Gamma \end{aligned} \tag{5.7}$$

The degree of significance of using the proper elevation angle determination depends on the radar geometry configuration; however, for any implementation requiring low elevation angle measurements, say 0° to $\approx 30^\circ$, and slant ranges $<\approx 0.1R_E$, the proper determination becomes extremely significant. For example, for ICEBEAR-3D with a mean scattering altitude of 100 km, slant ranges ρ vary from 100 km ($\alpha = 90^\circ$; straight up or perpendicular to the

tangent plane) to $\approx$ 1100 km ($\alpha = 0°$; horizontal or parallel to the tangent plane). For $\alpha = 90° \rightarrow 30°$, $\Gamma = 0° \rightarrow 1.5°$, therefore taking Γ into consideration is small and on the order of calibration and measurement errors. However, when $\alpha = 0°$ (horizontal), $\Gamma \simeq 10°$ and therefore it is critical that Γ be taken into consideration to determine the proper elevation angle. As otherwise, the elevation angle α would be determined to be 10° using the conventional vertical interferometry geometry interpretation, when in fact it actually should be 0°.

With the proper geometry applied to vertical interferometry, the ICEBEAR-3D meteor trail observations of the Geminid meteor shower now fall in the expected altitude range of 70 km to 110 km at all slant ranges, as shown in the bottom plot of Figure 5.1. Proper implementation of vertical interferometry geometry does not just apply to E region radars, but any radar observing finite ranges up to $\approx 10R_E$, for example aircraft tracking radars, ionospheric physics radars, satellite tracking radars, etc. using interferometry. The application of the proper geometry for vertical interferometry for other radars is discussed in Appendix F.

The above discussion applies to any situation where the constant phase reference cannot be represented by strictly planar geometry, such as vertical interferometry. For horizontal or azimuthal interferometry (East-West for ICEBEAR-3D) the constant phase reference surface corresponds simply to a plane only. Therefore, the basic interferometer equation, Equation 3.1, is directly applicable, where η would be azimuth angle of arrival, which is determined directly from the phase difference ψ. Even if the planar surface needs to be defined as the plane containing the constant phase chord from vertical interferometry, the projection to the tangent plane does not modify the horizontal interferometry azimuth angle. Likewise, if a sphere is the defining constant phase surface, the projection onto the tangent plane of the azimuth angle is unchanged.

5.3.1 Geocentral Angle Γ Determination

Determination of the geocentral angle Γ involves transcendental functions and therefore does not have a closed-form solution and must be solved using numerical techniques. As just discussed, Γ is needed for proper determination of the elevation angle α. Following is the geocentral angle Γ derivation based on Figures 5.6 and 5.7. From Figure 5.6

$$g = 2R_E \sin \frac{\Gamma}{2} \tag{5.8}$$

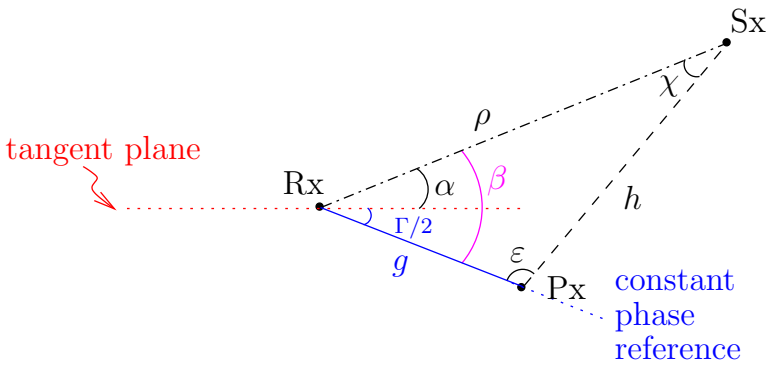

Figure 5.7: Proper geometry for elevation angle α determination, taking the constant phase reference chord of length g (line/chord Rx–Px) from Figure 5.6, into account. The scatter altitude is not realistic for E region radar observations, but has been enhanced for illustration purposes.

and

$$\varepsilon = \frac{\pi}{2} + \frac{\Gamma}{2} \tag{5.9}$$

therefore

$$\begin{aligned} \chi &= \pi - \beta - \varepsilon \\ &= \pi - \left(\alpha + \frac{\Gamma}{2}\right) - \left(\frac{\pi}{2} + \frac{\Gamma}{2}\right) \\ &= \frac{\pi}{2} - \alpha - \Gamma \end{aligned} \tag{5.10}$$

From Figure 5.7 and the law of sines

$$\begin{aligned} \frac{\rho}{\sin\varepsilon} &= \frac{g}{\sin\chi} \\ \frac{\rho}{\sin\left(\frac{\pi}{2} + \frac{\Gamma}{2}\right)} &= \frac{2R_E \sin\frac{\Gamma}{2}}{\sin\left(\frac{\pi}{2} - \alpha - \Gamma\right)} \\ \frac{\rho}{R_E} &= \frac{\sin\Gamma}{\cos\left(\alpha + 3\Gamma/2\right)} = \frac{\sin\Gamma}{\cos\left(\beta + \frac{\Gamma}{2}\right)} \end{aligned} \tag{5.11}$$

where R_E, the radius of the Earth, is constant and known and ρ and β are radar measured quantities, the slant range and improper angle of arrival output. Clearly, Equation 5.11 does not have a closed-form solution for the geocentral angle Γ and must be solved numerically. This equation is valid for all elevation angles from completely horizontal at $\alpha = 0°$ to completely vertical at $\alpha = 90°$ with respect to the tangent plane. However, although Γ depends

on the actual altitude geometry for a given radar implementation, it is markedly most significant for low elevation angles at finite slant ranges with $\rho < \approx 0.1 R_E$, which corresponds to altitudes h up to $\approx$ 1000 km. For other conditions, Γ can be small and need not necessarily explicitly be taken into consideration. For all ICEBEAR-3D observations, the geocentral angle Γ is numerically calculated from the transcendental equations, Equation 5.11. However, a very good approximation for $\alpha < 30°$ determinations is (in radians)

$$\Gamma \simeq \frac{\rho}{R_E} \tag{5.12}$$

Interestingly, this approximation works reasonably well for altitudes up to 1000 km, where Γ values are larger, being within 3–5° of the true value.

For E region altitude geometry with elevation angles α of 90° to 30°, not accounting for Γ introduces errors of 0° to $\sim$ 1.5°. These errors are typical on the order of phase calibration and measurement accuracies, therefore application of the conventional geometry for elevation angle determination works sufficiently well. Note that zenith viewing meteor radars only use observations from $\alpha = 00°$) down to $\alpha = 60°$–$70°$ due to concerns with spurious lower elevation angle measurements. For lower elevation angles the importance of taking the geocentral angle Γ into consideration becomes extremely significant: for elevation angles of 20° to 0° (horizontal), not taking Γ into consideration introduces substantial errors into the elevation angle determination of 2.3° to 10.1°, at E region altitudes. Most crucially, not taking Γ into account makes calibrating for low elevation angle measurements for horizontally viewing radars intractable. See Appendix F for the role of Γ for all types of radars.

5.3.2 Bistatic Slant Range Determination

The slant range ρ from receiver to target for a monostatic pulsed radar configuration is directly measured, whereas the slant range for a bistatic radar, such as ICEBEAR-3D, must be determined from the total RF propagation distance ρ_{RF}. From Figure 5.8 and the law of cosines

$$(\rho_{RF} - \rho)^2 = \rho_D^2 + \rho^2 - 2\rho_D \rho \cos\kappa \tag{5.13}$$

Solving for the slant range ρ

$$\rho = \frac{\rho_{RF}^2 - \rho_D^2}{2(\rho_{RF} - \rho_D \cos\kappa)} \tag{5.14}$$

where ρ is the bistatic slant range from the Rx antenna array to scattering location Sx, ρ_{RF} is the measured total RF propagation distance from Tx to Sx to Rx, ρ_D is the distance between the Rx and Tx locations, which are fixed and known, and κ is the angle between the measured slant range ρ direction, unit vector $\hat{u}_\rho$, and known value ρ_D direction, unit vector $\hat{u}_D$. The value for κ can be determined from the measured and known values using the dot product

$$\hat{u}_\rho \cdot \hat{u}_D = ||\hat{u}_\rho|| \cdot ||\hat{u}_D|| \cos\kappa = \cos\kappa \tag{5.15}$$

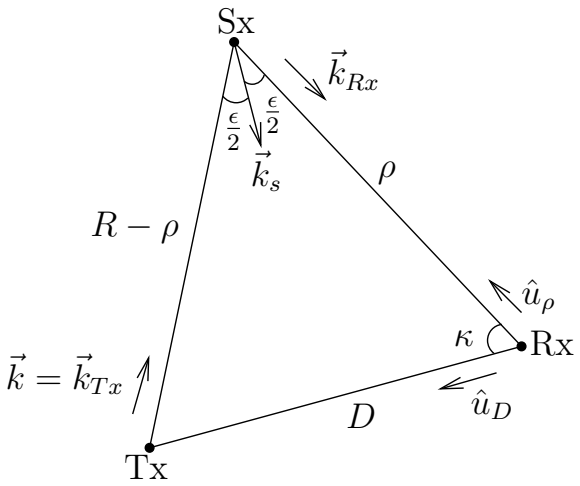

Figure 5.8: Bistatic geometry forms a triangle from Tx, Sx, and Rx locations. From this geometry the slant range ρ with respect to the receiver antenna array Rx can be determined.

Finally, the direction of the scattering medium wavevector $\vec{k}_s$ is in the bisector direction between the incident (or transmitted) radar wavevector $\vec{k}_{Tx} = \vec{k} = 2\pi/\lambda\ \hat{k}$ and the received radar wavevector $\vec{k}_{Rx}$ as shown in Figure 5.8. The scattering medium wavelength λ_s of the scattering medium detected by a bistatic radar configuration is given by Lovberg and Griem (1971)

$$\lambda_s = \frac{\lambda}{2\cos(\epsilon/2)} \tag{5.16}$$

where λ is the radar wavelength, which is $\lambda = 6.06$ m for ICEBEAR-3D, and ϵ is the angle between the transmitted $\vec{k}$ and received $\vec{k}_{Rx}$ radar wavevectors. Expressing Equation 5.16 in wavevectors

$$k_s = 2k\cos(\epsilon/2) \tag{5.17}$$

The final elevation angles and slant ranges for ICEBEAR-3D were determined by application

of iterative numerical relaxation to solve the transcendental equation, Equation 5.11. The relaxation method is initialized using the measured elevation angle β, total RF propagation length ρ_{RF}, and an assumed $\Gamma = 0.1°$. Then ρ is solved for using Equations 5.14 and 5.15, the results are used to find a new Γ, then iterates. The iterations continue until the slant range ρ is relaxed to an error of 10^{-5} km. Typically, this takes 5—6 iterations. The code is fully realized using a WGS84 Earth model and is given in Appendix G. The final output produced is target geolocation in latitude, longitude, and altitude, along with the bistatic velocity vector.

With the reliable and accurate geolocation of targets, the second and thirds goals of this thesis have been achieved. A method of measuring the altitude of terrestrial auroral E region instabilities and meteor trails has successfully been implemented, and a solution to the underlying problem with elevation angles measured in the low elevation regime has been given. The next chapter demonstrates the geolocated ICEBEAR-3D data and validates its veracity.

6 ICEBEAR-3D Results

The work of the previous chapters culminate in physical measurements of E region scatter and meteor trails that are distributed both spatially and temporally with unprecedented resolution. ICEBEAR-3D scans are 1 s temporally comprised of 1 (typically a meteor trail) to $\approx 12,000$ (active E region) targets, depending on E region and meteor trail activity. The location of each target is determined at 1.5 km range resolution and 0.1° angular resolution. This locates targets in spatial bins roughly 1.5 km by 1.5 km by 1.5 km, depending on the slant range. Doppler velocity is measured at 10 Hz (≈ 30 m/s) resolution along the bistatic vector. The final data product produced by synthesis aperture imaging is the location of the target in azimuth, elevation, and range, and in geographic coordinates.

This chapter relates the distribution of spatial locations of targets collected by ICEBEAR-3D to expected locations. As the azimuth, elevation, and slant ranges are converted to geographic coordiantes, validation was performed on the latitude, longitude, and altitudes measurements. The latitude and longitude locations of several million targets were compared to the modeled link gain, discussed in Chapter 2. Elevation angles and slant ranges that were determined by application of the proper geometry for vertical interferometry are validated by comparing the altitudes of meteor trails detected to well established meteor trail altitude distributions. The validation leads to an error in altitudes of targets in the far west lobe of the radar's field of view. This error is discussed. Then several examples of the ICEBEAR-3D Level 2 1 s data products are shown.

6.1 Validation by Data

In the previous chapters, each stage of development of ICEBEAR-3D was validated through isolated measurement or simulation. The accuracy of the complete integrated system was validated using real measured data. The final ICEBEAR-3D Suppressed-SWHT imaging data product is the geographic coordinates of targets. The latitude, longitude, and altitude accuracy were validated by use of E region scatter for latitude and longitude and meteor trail echoes for altitude.

In Chapter 2 the link gain, Figure 2.8, was discussed. This plot showed the regions in latitude and longitude at 110 km altitude that the link between the transmitter and receiver would be powerful enough to detect echoes. Assuming echoes in this region are not biased, Figure 2.8 is the theoretical map of where the radar expects to locate echoes in longitude and latitude. A histogram of $\simeq$ 19.5 million E region scattering target locations is shown in Figure 6.1. The histogram was generated from 177 days across all seasons of low to moderate E region activity in 2020 and 2021. The histogram illustrates the locations where echoes with sufficient power are typically located. The histogram and the theoretical link gain each show the same five prominent areas, which are separated into three distinct lobes. Figure 6.2 overlays the histogram of real data with a contour of the theoretical link gain model at the E region scatter peak altitude of 107 km (Hussey, 1995). Qualitatively, the data aligns extremely well with the link gain model. At a 3 dB link gain minimum and 3 dB SNR cutoff, the model encapsulates 98.8% of all targets. The normalized counts of the histogram and normalized gain of the link model are fairly strongly positively correlated, with a correlation coefficient of 0.83. The primary difference being, the close slant range data missing in the histogram, but this is due to the practice of cutting all data less than 300 km slant range to remove self-clutter.

The altitude validation was performed using the meteor trail altitude distribution from the Geminid meteor shower from 12–15 December 2020. Application of the proper geometry for vertical interferometry gives a meteor trail altitude distribution which precisely matches the distributions and peak altitudes measured by various zenith looking radars. Regardless of the radars latitude or operating frequency, meteor trails are detected between 70 km and 110 km with a peak altitude around 90 km to 105 km (Hocking, Fuller, & Vandepeer, 2001; Holdsworth & Reid, 2004; Holdsworth, Reid, & Cervera, 2004; Lee, Jee, Kim, & Song, 2018; Chau et al., 2019). This altitude peak varies with solar cycle, time of year, time of

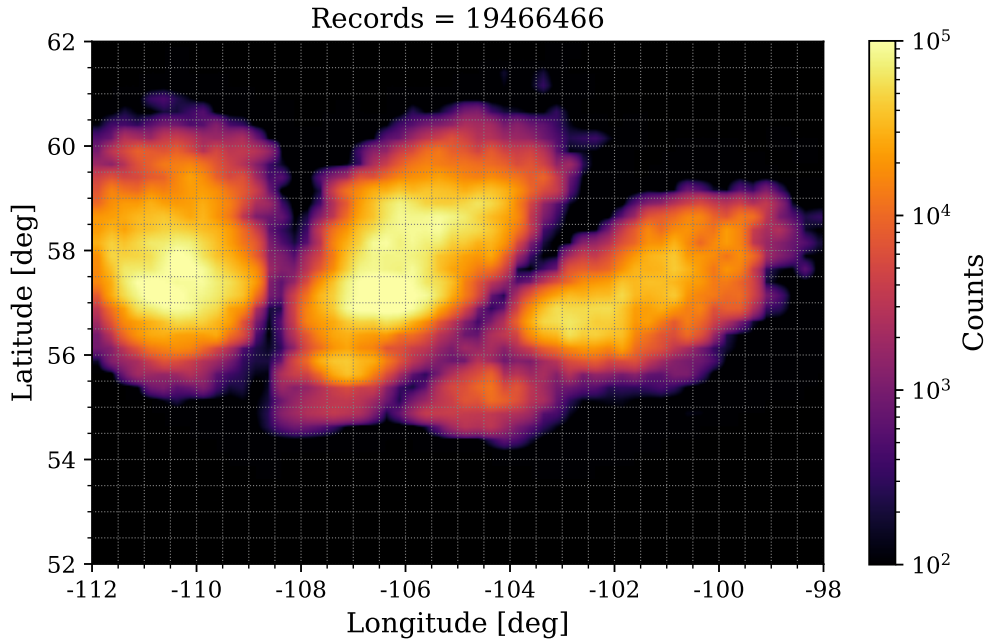

Figure 6.1: Histogram of real target echo locations from ICEBEAR-3D from 177 days of low to moderate E region activity. The data was collected from 3 March 2020 to 31 March 2021. A 3 dB threshold is applied to remove extraneous noise, leaving 19,466,466 data points. The histogram has a latitude and longitude bin size of 0.25° by 0.25°. There are three distinct lobes, with the east most and center lobes subdivided into two lobes. The formation matches the theoretical locations of the link gain model.

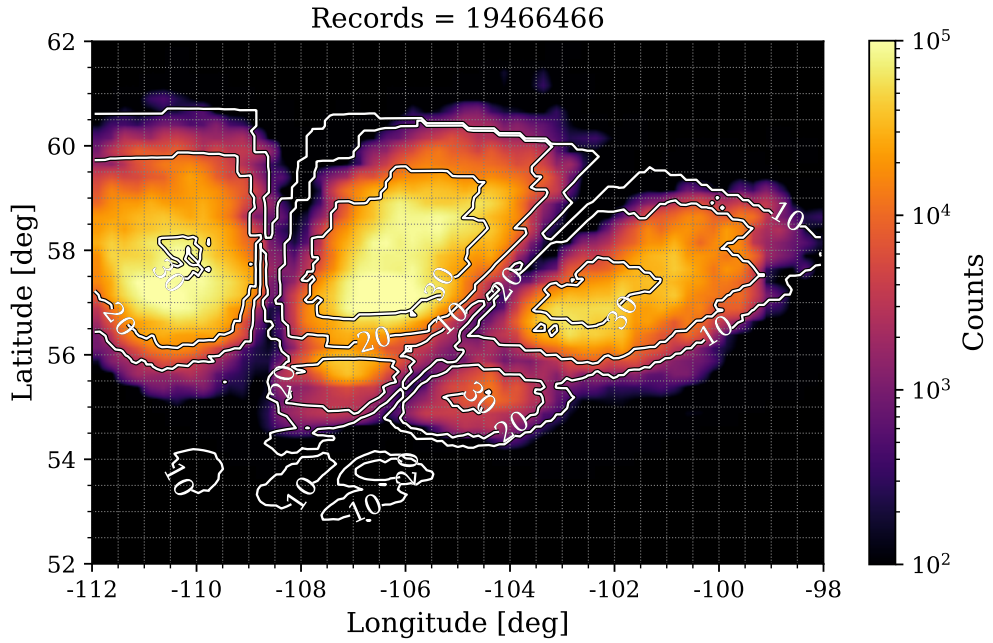

Figure 6.2: A contour plot of the theoretical link gain model at 107 km with coarse levels of 10 dB, 20 dB, and 30 dB overlaid on the results shown in Figure 6.1. The contours outline the areas where echoes are more likely to be powerful enough to be detected. The contours link gain and background histogram have a correlation coefficient of 0.83 indicating they are strongly positively correlated.

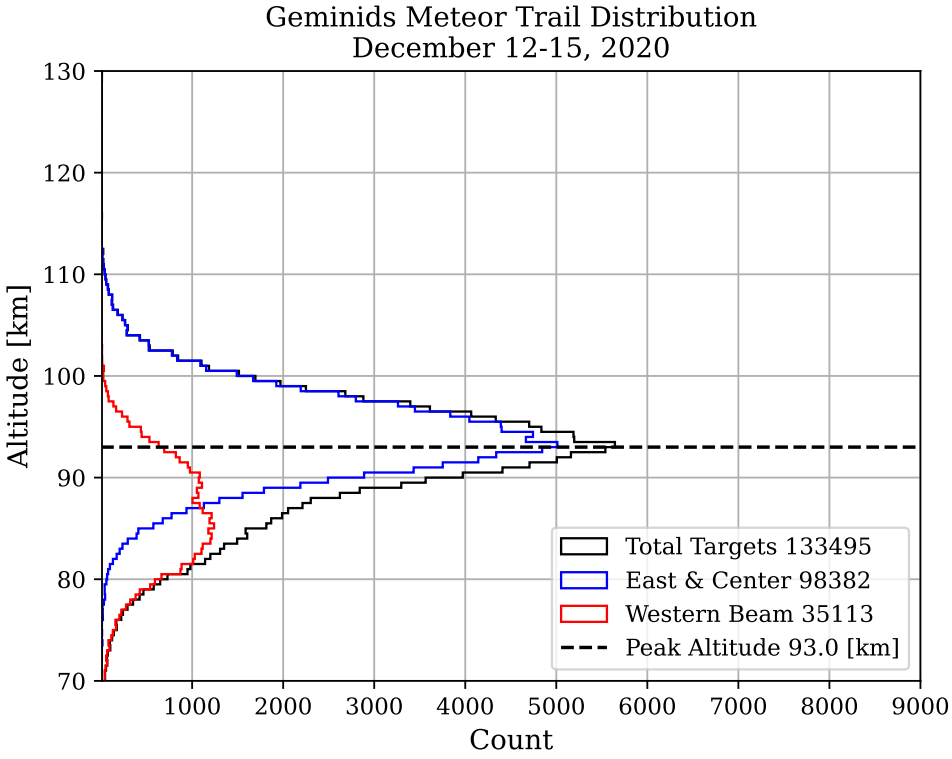

Figure 6.3: Altitude histogram of meteor trails from the Geminids meteor shower from 12–15 December 2020, showing a peak altitude of 93.0 km distributed between 70 km to 110 km. The west lobe (red) has been removed from the center and east lobe (blue). The data has a 1.0 dB cutoff SNR.

day, and radar operating frequency. The ICEBEAR-3D altitude distribution results for the 2020 Geminid meteor shower are shown in Figure 6.3. The black line shows the altitude distribution for all lobes. The blue line isolates the west lobe (red) from the center and east lobe. This is done to reject the west lobe data as it is errant, being lower in altitude than echoes from the center and east lobes. The west lobe discrepancy will be discussed in the next section; here only the center and east lobe data is used for comparisons. The measured meteor trail distribution and peak altitude agree exceedingly well with the aforementioned radar studies. In direct comparison, Sugar et al. (2010) found that nonspecular meteor trail altitude distributions peak between 93 km and 105 km (with standard deviation of 3.8 km to 4.6 km), the variance in peak altitude depending on short trails versus long trails and time of day. These meteor trails peak is at 93.0 km with a standard deviation of 4.77 km.

The altitude distribution shown in Figure 6.4 is a typical ICEBEAR-3D altitude distribution of E region ionospheric scatter during a geomagnetically active period after the proper

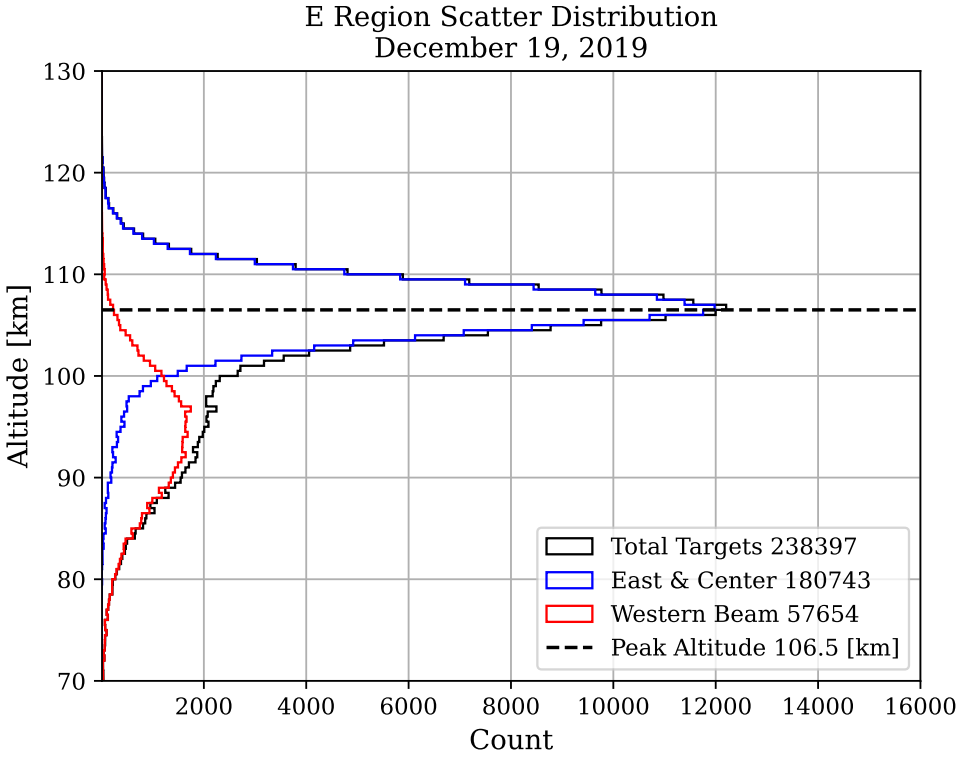

Figure 6.4: Altitude histogram of E region echoes from 19 December 2019, four days after the 2019 Geminids meteor shower. This plot shows a typical E region scatter observation altitude distribution. The peak altitude of the center and east lobes (blue) is 106.5 km. The smaller, lower altitude distribution peak corresponds to the west lobe (red). The data has a 1.0 dB cutoff SNR.

geometry for vertical interferometry is applied. This event was recorded from 00:00 UT to 14:00 UT 19 December 2019. The distribution peak altitude is 106.5 km (standard deviation of 4.28 km), agreeing with the expected E region peak between 105 km to 110 km (Hussey, 1995). The altitude distribution shown in Figure 6.5 is a period from 00:00 UT to 14:00 UT 20 March 2021. This period was very active, ICEBEAR-3D measured 38 times as many records as 19 December 2019 in the same time period. Here echoes from the bottom of the E region dominate, biasing the altitude distribution peak to 103.5 km (standard deviation of 7.53 km). This peak is possibly dominated by the slow broad echoes (Type 2) that spread across the whole field of view. These altitude distributions generated from the proper geometry for vertical interferometry all align with expected altitudes; in particular, the meteor trail echoes altitude distributions agree extremely well with both observation and theory.

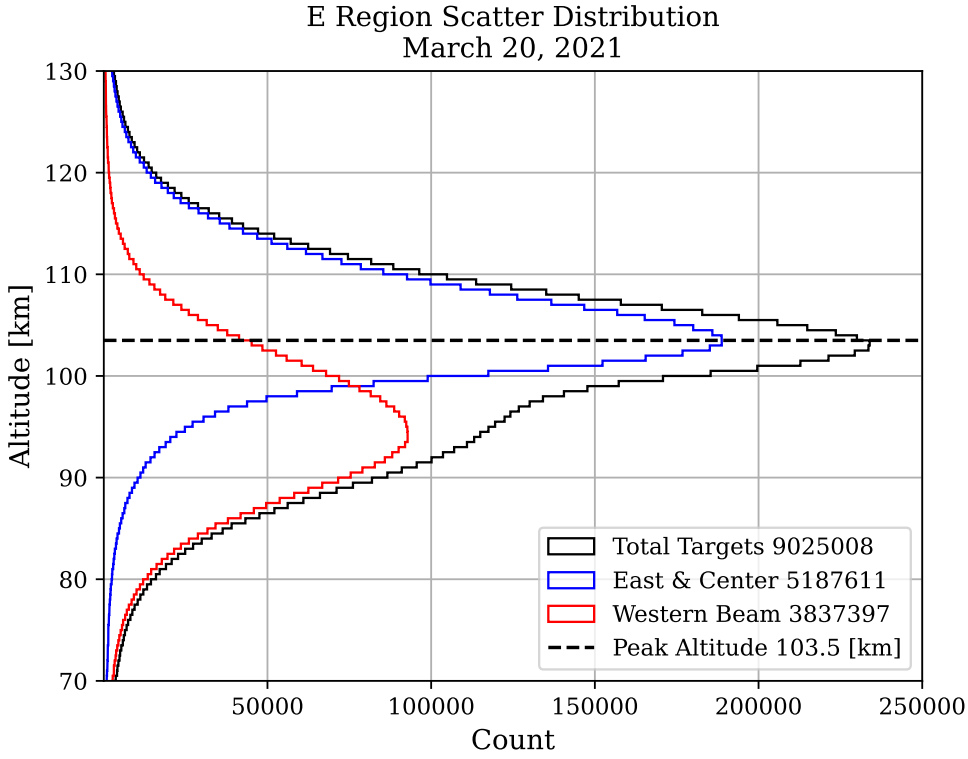

Figure 6.5: Altitude histogram of E region echoes from 20 March 2021 during an active day. The day is dominated by the slow broad echoes (Type 2). The peak altitude determined by the center and east lobes (blue) is 103.5 km. The west lobe (red), although numerous, is errant and biased lower than what E region physics would suggest. The data has a 1.0 dB cutoff SNR.

6.2 West lobe Anomaly

As plainly seen in Figures 6.3, 6.4, and 6.5, the altitude distribution of the western lobe is characteristically lower than the eastern or center lobes. By separating the western lobe into 1° azimuth slices it becomes apparent that the altitude distribution peak is not smoothly dropping across the lobe. Rather, there appears to be a local minimum. This indicates that there is not a systematic computation error causing the western lobe to be errant, but a physical one. Upon inspection of the area around the receiver antenna array, one can clearly see that the field of view in the direction of the western lobe, and only the western lobe, is occluded by a dense patch of trees. In particular, the azimuth angle of arrival which produces the lowest altitudes, $-23°$ from boresight, was directly aligned with a row of dense brush. Considering the radar signal wavelength is ≈ 6 m and the receiver antenna array is placed in

a relatively flat region of the Canadian prairies, it was assumed that the ground plane around ICEBEAR-3D was nearly symmetrical in all directions. To a ≈ 6 m wave, minor topological variations like those of arable land are neglectable as the signal will penetrate the ground by ≈ 1 m before reflecting due to the skin effect (Boithias, 1987). However, buried structures such as large boulders, tree roots, metal fences, etc. potentially break this assumption.

From Equation 3.4, it was shown that provided the ground plane is similar at the points of reflection for the reflecting rays for two antennas, such that the reflection coefficients are equal, that the received magnitude is doubled. The phase is unmodified, as only the total phase difference between the two antennas matters. In the western lobe direction, the points of reflection for reflected rays along the vertical interferometry baselines will vary as one scans azimuthally between water, arable farmland, and trees with dense root structures. For example, for a North-South antenna pair will, the front antenna will have reflection points on arable farmland, whereas the rear antenna's reflection point may lay in a forested area. Since the reflection coefficients for these two antennas would not be equal, the cross terms in Equation 3.4 cannot be neglected and the relationship from Equation 3.6 would no longer hold. The cross terms would contribute a phase error, which when propagated through the synthesis aperture imaging stages results in erroneously low altitudes being detected in the western lobe.

Although it is expected that this multipath interference from differing ground planes causes the anomalously low altitudes in the western lobe, this requires further investigation and is beyond the scope of this thesis. Currently, ICEBEAR-3D studies only use altitudes from the center and eastern lobes.

6.3 Examples of ICEBEAR-3D Data Products

Following are several examples of typical ICEBEAR-3D 1 s data products. Figure 6.6 demonstrates the ability to isolate multiple scattering volumes within the radar field of view. Figure 6.7 demonstrates the ability to study the evolution of E region plasma physics in great detail, both temporally and spatially.

In Figure 6.6 the left and top plots show altitude cross-sections of three distinct scattering volumes from 2 February 2021 at 5:53:48 UT. The altitudes range from 80 km to 130 km. The

velocity of each scattering volume is distributed in altitude: the near white (≈ 0 m/s) volume (Type 2) being lower altitude than the faster light blue (Type 1) and dark blue (Type 4) volumes. The right plot of Figure 6.6 shows the three distinct scattering volumes distributed in latitude and longitude. Also shown are the transmitter (Tx) and receiver (Rx) locations.

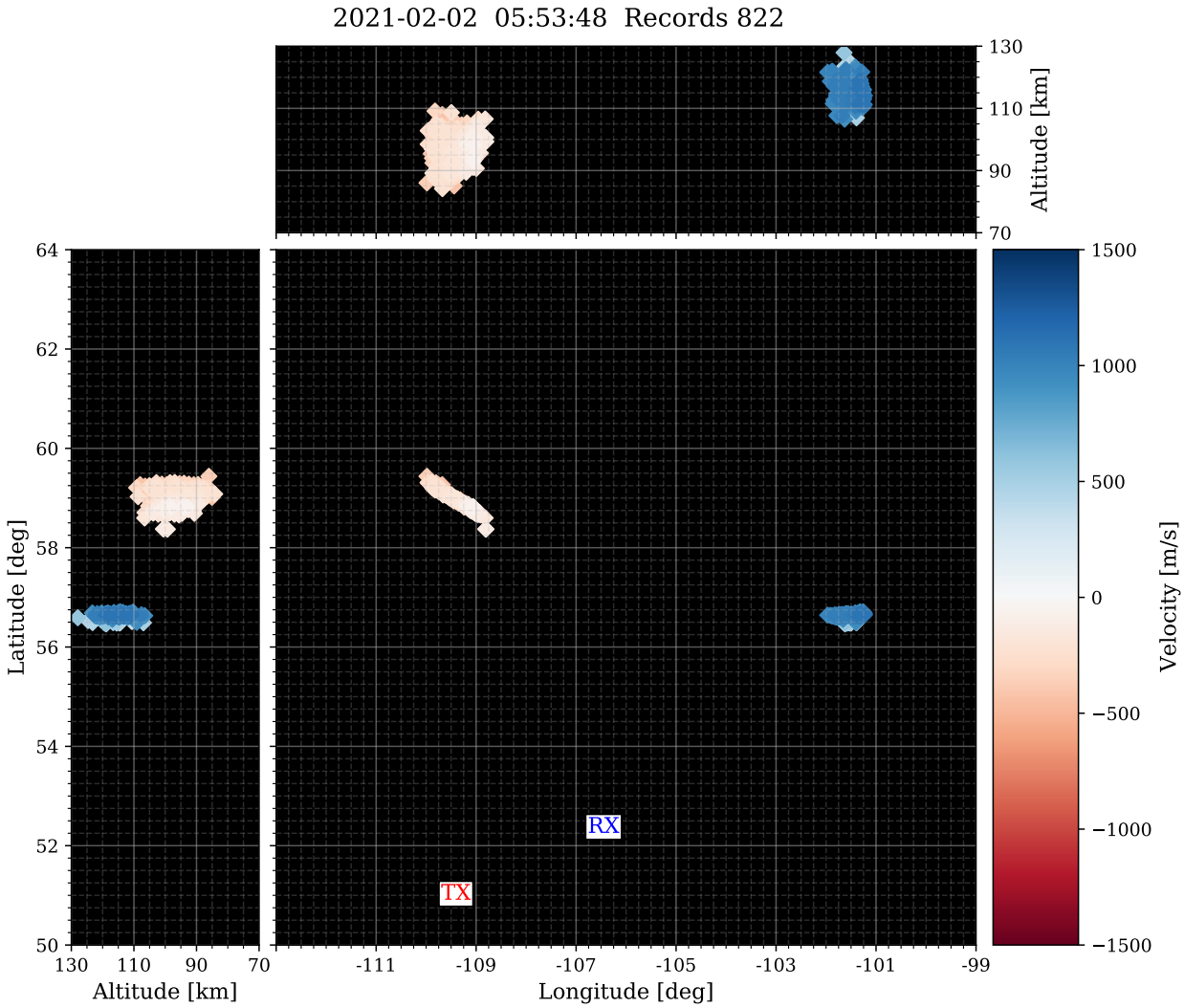

Figure 6.6: A 1 s ICEBEAR-3D data product from 2 February 2021 at 5:53:48 UT. The left plot presents a latitude versus altitude perspective, the top plot is a longitude versus altitude perspective, while the right plot is a 'birds-eye view' in latitude and longitude. The color indicates the magnitude and direction of the Doppler velocity in m/s as measured along the bistatic vector. Observable are three distinct scattering volumes showing decidedly different velocities towards and away from the radar. The plot is comprised of 822 individually observed targets. A 1 dB SNR cutoff was applied. Figure from (Lozinsky et al., 2022).

Figure 6.7 is from an event on 31 March 2020 between 3:19:20 UT and 3:24:10 UT. Here, ICEBEAR-3D observed a scattering volume with a measured velocity near 500 m/s (blue) towards the radar, which formed earlier to the east before travelling westward and disappearing. The blue scattering volume was well defined and localized throughout the entire period. As the volume travelled westward it passed through two transmitter antenna array directivity nulls within the bistatic radar antenna field of view. The white (0 m/s) scattering volume is continuous across the latitude-longitude view, the empty regions at (57.0°, −108.5°) and (56.5°, −104.5°) correspond to the nulls in the transmitter antenna array directivity.

The spatial geolocation of targets, meteor trails and E region scatter, align with both the theoretical locations and locations expected by past radar observations. This was confirmed using many millions of points over several years. The altitudes of meteor trails specifically, were used to validate the difficult to find elevation angles. The two 1 s snapshots examples provided demonstrate the wide range of E region targets capturable by ICEBEAR-3D simultaneously. These results would not be possible if the three goals set at the outset of this thesis were not achieved.

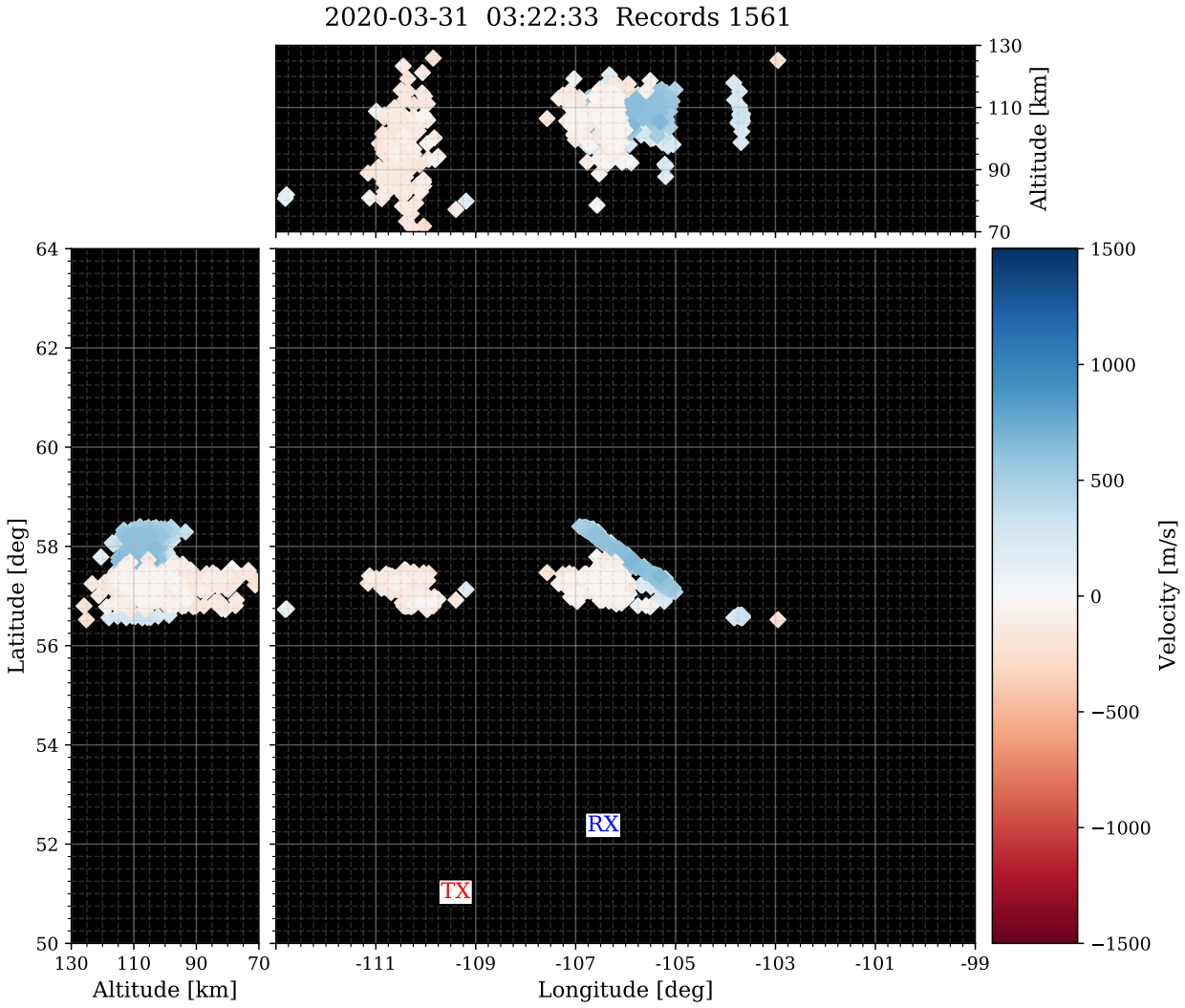

Figure 6.7: A 1 s ICEBEAR-3D data product from 31 March 2020 at 3:22:33 UT. The left plot presents a latitude versus altitude perspective, the top plot is a longitude versus altitude perspective, while the right plot is a 'birds-eye view' in latitude and longitude. The color indicates the magnitude and direction of the Doppler velocity in m/s as measured along the bistatic vector. Observable is a distinct scattering volume, which is narrow and long with a velocity near 500 m/s (light blue). This distinct scattering volume formed at 3:19:20 UT and traveled westward until 3:24:10 UT; presented herein is the middle evolution of this scattering volume. The plot is comprised of 1561 individually observed targets. A 1 dB SNR cutoff was applied. Figure from (Lozinsky et al., 2022).

7 Conclusion

At the outset of this thesis, the original task was a straight forward and seemingly simple goal — redesign the receiver antenna array to get elevation angles. However, this task is neither simple nor straight forward. The scope of the project quickly expanded to include not only antenna array design, but radar imaging, elevation angle determination, software development, and data product management. This is because obtaining radar elevation angles within the low elevation regime is exceedingly complex. After a thorough literature review, it was clear that although trying to obtain elevation angles with a 49.5 MHz radar at viewing angles near the horizon has been attempted in the past, it has never been done successfully. Until now. ICEBEAR-3D is the foremost coherent auroral ionospheric E region radar. It is the first instrument to use the Suppressed Spherical Wave Harmonic Transform (Suppressed-SWHT), and the first instrument to apply the Spherical Wave Harmonic Transform (SWHT). It is the first radar to acquire accurate 1.5 km resolution altitude measurements of the auroral E region.

Each of the goals outlined at the outset of this thesis have been accomplished.

1. To determine and implement a method to remove the effects of azimuth aliasing caused by the inherent 2π phase ambiguity

Azimuth angles of the original ICEBEAR, with its linear uniformly spaced receiver antenna array, were affected by $n2\pi$ aliasing. In Chapter 3 this goal was achieved by the radar receiver antenna array design, which used all unique and non-harmonic baselines to remove aliasing. The redesign was performed using a combination of the Jacobs-Ralston technique and Random-walk Annealing technique. The resulting array had a phase error tolerance of $\pm 14.86°$. This keeps results consistent even as the receiver antenna array phase calibration drifts. Construction of the new receiver antenna array design was completed in the summer of 2019 and has been operating since.

2. To determine and implement a method of measuring the altitude of terrestrial auroral E region instabilities and meteor trails

The new receiver antenna array used baselines placed in the North-South direction and exploited the ground plane reflection to gather phase difference information related to target elevations. The complex receiver antenna array with all unique baselines required more complex methods to process voltage samples into useful measurements than the original ICEBEAR. The imaging method used was the Suppressed-SWHT, introduced in Chapter 4. The Suppressed-SWHT was selected as it solved all the problems associated with imaging auroral E region scatter, namely: extended source targets, extremely wide fields of view, non-planar geometry, and low elevation angles. The Suppressed-SWHT used pre-cached coefficient matrices and GPU processing to rapidly image upto 200,000 images per second. Targets within each image were located with an image processing algorithm. The result is target acquisition in 3D at 1.5 km x 1.5 km x 1.5 km spatial resolution. Evidence provided in Chapter 6 shows clearly that the goal of acquiring accurate altitudes of both E region scatter and meteor trails has been accomplished.

3. To elucidate and solve the underlying problem with elevation angles measured in the low elevation regime when using horizon pointing radar interferometers

Elevation angles measured in the low elevation regime are often conflated with phase errors. ICEBEAR-3D observers an unmistakable rising of elevations with slant range, that is common across all radars operating in the low elevation regime. This long standing problem is poorly recorded in literature, but well known in application. All alternative corrections and explanations were exhausted attempting to solve this problem for ICEBEAR-3D. Due to the excellent phase tolerance and resolution of ICEBEAR-3D the underlying dependency on the geocentral angle Γ was elucidated. This led to the development of the proper geometry for vertical interferometry interpretation, which uses the geocentral angle to adjust the phase reference plane to the chord which connects the receiver antenna array location to the target-Earth pierce point. This geometry accounts for the apparent excessive angle measurement β, which is naturally measured by an interferometer when measuring phase differences between antennas at differing phase references on a curved measuring surface such as the Earth. The proper interpretation geometry for vertical interferometry is a potential and compelling solution to the long standing low elevation angle regime problem.

7.1 Future Work

The work detailed within this thesis has readied ICEBEAR-3D for further development. Taking this future development into a consideration, careful diligence was taken to design the data products so that they would be easily usable. Considerable time and effort was spent conforming the data products to Common Data Format (CDF) standards (Liu, 2022). This means the packaged HDF5 data files are user complete; no additional supplementary material is needed, all necessary information is contained within the data product's metadata.

ICEBEAR-3D has shown significant improvement over its predecessor, ICEBEAR, yet there remains much work to be done. The future engineering projects for ICEBEAR-3D are listed below, ordered from most readily doable in the short term to most challenging long term projects.

Auto-calibration

Accurate and timely phase and magnitude calibration of the 10 receiver channels is required to maintain radar performance. Manual calibrations using a vector network analyzer are currently irregularly performed, typically once or twice per year. A calibration that could be performed once per month or even daily would dramatically improve the confidence in the data. Galeschuk (2021) purposed a calibration method that used the celestial radio source Cygnus A as it passes through the ICEBEAR-3D field of view. The method had good results, but was occasionally unable to generate calibrations for some baselines. The Cygnus A calibration used the known location of a radio source to compute the expected phase response of the receiver antenna array and compared it to the response measured. This technique is in principle similar to determining the closure angle, as discussed in Section 6.1.

A phase calibration is determinable by averaging the closure angles of many meteor trail echoes in a given day. The process is simple; given a meteor trail echo, which is a point like target, find all closure angles for each combination of three channels. Then for each channel sum the closure angles for each combination the channel appears and divide by the number of appearances. For ICEBEAR-3D which has $n = 10$ channels there is $n(n-1)(n-2)/6 = 120$ three channel combinations where each antenna appears $(n-1)(n-2)/2 = 36$ times. This process is then repeated for several meteor trail echoes in a given day and the result

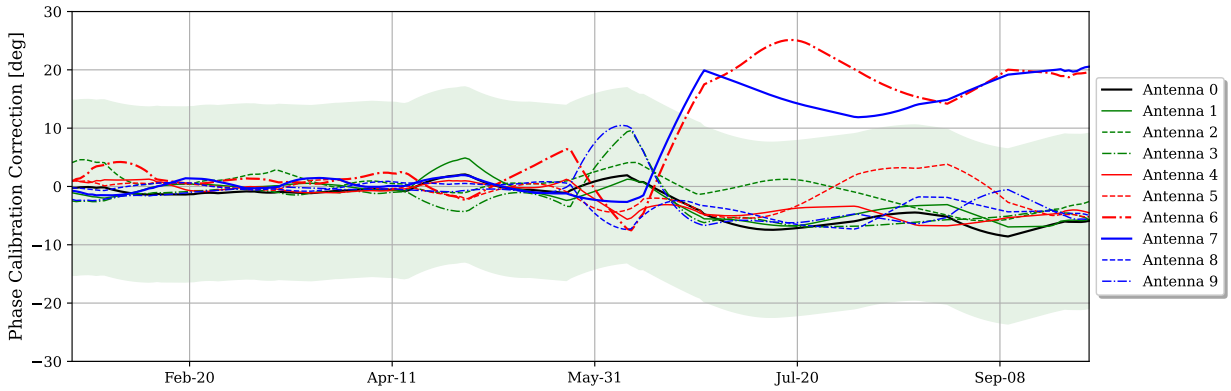

Figure 7.1: Phase calibration correction per channel for each day of year 2020. The shaded green area is the phase error tolerance margin. Antennas 6 and 7 become out of tolerance after 17 June 2020.

per channel is averaged. This final averaged value is the offset required from the current calibration to return the closure angles to zero, causing the array to be properly calibrated.

In Figure 7.1 the closure angle autocalibration has been performed for every recorded day in 2020. The plot shows the phase calibration correction required per channel as the year progresses. The shaded green area is the zone in which the phase calibration is within design tolerance ($\pm 14.86°$) and no noticeable angle of arrival deflections are measured. Sometime around 2020 June 17 the channels for antennas 6 and 7 moved out of tolerance. This is reflected in the summary data for days after this point, where noise is far more prevalent. What remains to be done is validation, daily implementation, and adding the magnitude calibration, which can be calculated similarly using the magnitude closure relationship given in Thompson et al. (2001). Validation is done by finding the calibration correction for a given day, then manually calibrating the next day and comparing the results.

1λ Transmitter Baseline

The three beam pattern seen in the ICEBEAR-3D data histogram shown in Chapter 6 and link gain maps in Chapter 2 are due to the two transmitter antennas having a 3λ separation. This three beam pattern leaves nulls within the field of view. When viewing animations of the 1 s data, mapped streams of targets will disappear in the nulls. This effect can be removed by operating the transmitter antennas with a 1λ separation. This would create one

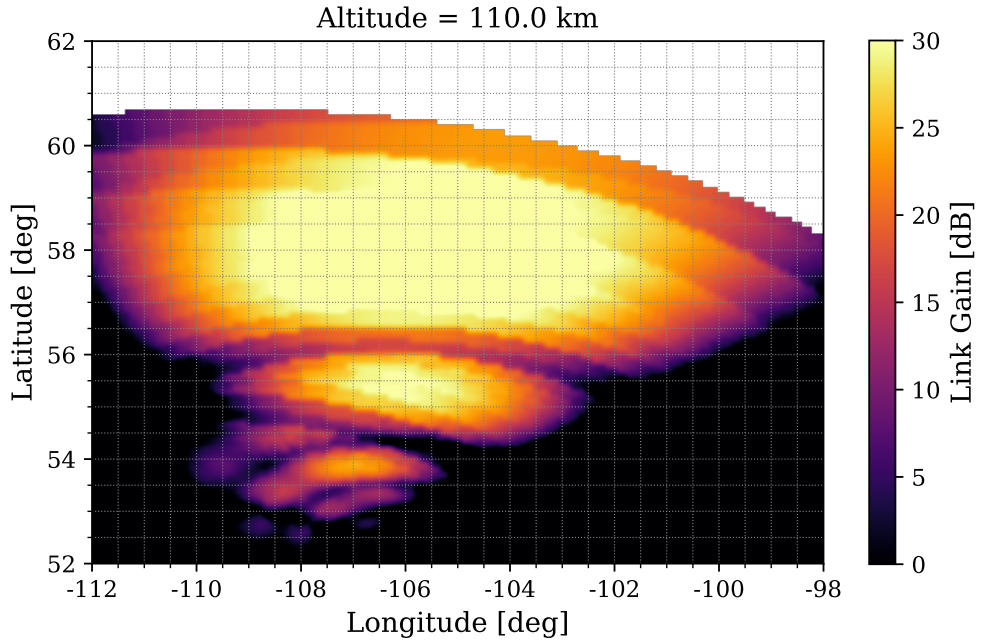

Figure 7.2: Superposition of a 1λ two antenna separation transmitter array gain pattern and receiver antenna gain pattern in dB. The link is modeled on a WGS84 Earth model at a constant 110 km altitude. The white area is the region where the Earth occludes a direct line of sight link. The regions show where the bistatic radar has sufficient gain to sense targets.

larger central lobe, narrowing the field of view slightly, while removing the nulls. Figure 7.2 illustrates what the resulting link gain map would look like. The results from Figure 6.2 show that the theoretical and observed match well in the 3λ separation case, indicating that the data collected with a 1λ transmitter configuration would also match the theory.

σ Cross-sectional Area

A target's received power P_{rx} is given by the radar range equation (Richards et al., 2010)

$$P_{rx} = \left[\frac{P_{tx}G_{tx}G_{rx}\lambda^2}{(4\pi)^3 r_{tx}^2 r_{rx}^2}\right]\sigma \tag{7.1}$$

where P_{tx} is the transmitted power, G_{tx} is the gain due to the transmitter antenna array, G_{rx} is the receiver antenna gain, λ is the radar wavelength, r_{tx} is the distance between the transmitter and scatter location, r_{rx} is the distance between the receiver and scatter location, and σ is the echo cross-section area. The goal is to measure the echo signal strength due to the cross-sectional area σ. This is a relative measurement. For a monostatic radar, removing system contribution is unnecessary, as the radio propagation to and from the target follow the same path. Meaning $G_{tx} = G_{rx}$ and $r_{tx} = r_{rx}$, so the parts within the square brackets of Equation 7.1 is only a function of total range and easily accounted for. The bistatic case is more complicated as the part within the square brackets becomes a function of the RF propagation path ellipse, and angle of arrival (since gain is not equal in all directions). The link gain map calculation generated from NEC models of the transmitter and receiver antenna arrays gives the value of $G_{tx}G_{rx}$. P_{tx} is known (59 dBm (Huyghebaert et al., 2019)) as well as λ, r_{tx}, and r_{rx} from the geocentral calculation. Thus, all system components of the received power can be removed and the power due to σ is calculable. It is suggested that this be attempted and possibly added to regular processing.

Doppler Spectra

The Doppler spectra of a target is a useful parameter for studying the physics of the E region, as well as classifying scatter into the Types mentioned in Chapter 1. The nature of ICEBEAR Level 1 data processing, as discussed in Section 2.4, produces discrete Doppler. A Doppler spectra for each target is not directly obtainable. A method of producing Doppler spectra by using the Doppler values of many adjacent targets around the target of interest and fitting a Gaussian has been attempted by other ICEBEAR researchers, specifically Devin Huyghbaert. This method produces uncharacteristically narrow spectra. This method and others to generate Doppler spectras should be explored and become a part of the regular processing chain.

Dropped Samples

The Ettus Instruments X300 SDRs have a quirk which has as yet not been patched by the manufacturers. This quirk is known as a dropped sample. It occurs when a X300 SDR detects a dropped packet and then fills the buffer with zeros. A dropped sample occurs roughly once

every 15 minutes, making the data for the few seconds around it unusable. A dropped packet is caused by: network hardware failure, the PCIe bus on the operating computer being unable to sustain the throughput, a CPU governor or power management being misconfigured, or data frame size errors. When the operating computer receives a dropped sample message, it replaces the voltage values in the buffer with $1 + 0j$. When these voltage samples are processed, they appear as targets that fill every range-Doppler bin and seem to come from a specific direction. Currently, these dropped samples are filtered at several stages, but the filters are not completely effective. The dropped samples need to be removed at the source by fixing the issue with the X300 SDRs and operating computer.

Interference

There are interference sources that affect the radar irregularly. Their sources are difficult to locate due to their intermittent behavior. The current best analysis for one interference source is that it originates from somewhere around the Dundurn, SK, military base and ammunition depot. The other source is not well understood and appears to cause a very low SNR responses in random range-Doppler bins across long periods of time. These interference sources, and other, need further investigations.

Deconvolution Method for Multiple Targets per range-Doppler Bin

As briefly mentioned in Chapter 4, the current Suppressed-SWHT imaging solution is limited to assuming only one target exists per range-Doppler bin. This however is not necessarily a safe assumption. ICEBEAR-3D using the unsuppressed SWHT is capable of detecting and isolating multiple targets per range-Doppler bin, provided the targets are spatially separated by more than the Rayleigh criterion limit $\theta \approx 1.22/b_{max}$, which is about 30 km for targets in the ICEBEAR-3D field of view.

An example of multiple targets in a single image was shown in Figure 4.6. In this image there are clearly two targets, but there are also many other artefacts caused by the dirty beam. The Suppressed-SWHT is a way to suppress the dirty beam effects, but it also removes other targets. Removing the dirty beam artefacts is usually done with a deconvolutional method. A modified Cotton-Schwab CLEAN algorithm is a likely candidate as it works with

ungridded points, uses the full phase equation, and includes the w-term when computing residuals (Schwab, 1984). Alternatively, a CLEAN like approach using the Suppressed-SWHT should be attempted.

Selection Algorithm

Application of a deconvolution method would necessitate the development of a new selection algorithm as the current algorithm, described in Section 4.7, assumes a single target per image. The current method uses the OpenCV image processing library to determine the contours around a target (Bradski, 2000). These contours can be found around multiple targets and a bounding box placed around each. Then the maximum points inside each bounding box can be used to determine the target's angles of arrival. Additionally, the algorithm would also likely need to take into account the mean and maximum brightness points across the dirty image in order to discern real and false targets.

Comparison of Imaging Methods

In Chapter 4 the SWHT imaging method was discussed. The imaging method was compared to the direct vCZ theorem. Not discussed in this thesis are the attempts to image using the w-stacking, w-projection, regridded direct FFT, fit lookup table, or MUSIC methods. These attempts had varying degrees of success, and development with them was halted once the SWHT showed significant promise over them. However, these methods and many more newer methods should all be attempted and compared to the Suppressed-SWHT. These comparisons have begun with the development of the pyIRIS (Python Interferometric Radar Imaging Suite) by Adam Lozinsky and Devin Huyghebaert.

Optimized Suppressed-SWHT

The product of spherical harmonics is equivalent to the summation of a high order spherical harmonic with residuals (S. A. Holmes, 2002). The Suppressed-SWHT suppresses the dirty beam by using the product of lower coefficient matrices with higher order ones, where a coefficient matrix C_l is the sum of many spherical harmonics, as discussed in Chapter 4.

This means the products in the Suppressed-SWHT are effectively generating many high order spherical harmonics and many residuals from all the cross terms. For example, take the product of $\mathbf{C}_1$ and $\mathbf{C}_2$

$$\mathbf{C_1C_2} = (Y_{0,0}+Y_{1,-1}+Y_{1,0}+Y_{1,1})(Y_{0,0}+Y_{1,-1}+Y_{1,0}+Y_{1,1}+Y_{2,-2}+Y_{2,-1}+Y_{2,0}+Y_{2,1}+Y_{2,2}) \quad (7.2)$$

which has many repeated cross terms. The high order spherical harmonics found provide a better imaging fit. The residuals, however, are lower order spherical harmonics which have already been accounted. This effectively biases, or windows, the image by the lower order spherical harmonics, which fixate on the single strongest source in the image. There should exist a way to compute specific higher order spherical harmonics and subtract away the residuals to form a precise Suppressed-SWHT coefficient matrix with a designed window. This coefficient matrix would be collapsed, making image processing less memory intensive and quicker.

More Receiver Antennas

The discussions in Chapter 3 showed that resolving power of the receiver antenna array was limited by the number of antennas available. Every additional antenna added to the receiver antenna array will dramatically improve performance, provided it is placed in areas off axis that creates all unique baselines. Currently, the ICEBEAR transmitter site has 10 antennas, but only 2 are used. Each X300 SDR has two channels, so the transmitter site has 5 SDRs. One X300 SDR and two antennas could be moved to the receiver antenna array at little cost. This would bring the total unique baselines to 132 from 45, a three times increase of baselines. This would have a profound effect on the radars image quality and tolerance, at the expense of more data storage and processing.

Multistatic Configuration

As just mentioned, the transmitter site nominally only requires 2 antennas and 1 X300 SDR. If 1 X300 SDR and two antennas are moved to the receiver site, and 2 X300 SDRs and 4 antennas are kept at the transmitter site for redundancy, that leaves 2 spare X300 SDRs and 4 spare antennas. The spare equipment and respective cabling and HPAs could be moved to another transmitter site. An optimal location would be near Lipton, SK. A transmitter site

there would be equal distance from the Bakker receiver site as the Prelate transmitter site is currently. Lipton, SK is also at the same latitude as Prelate, SK, thus keeping the propagation characteristics similar. The second transmitter site would transmit an orthogonal CW PRN code to Prelate. The additional transmitter site would give a second bistatic radar vector per target. This allows for 2D velocity vectors to be found. The second transmitter would also fill in the field of view more completely.

Although ICEBEAR-3D could be improved by the previously discussed topics, it is operating extremely well. It reliably produces a higher spatial resolution data product than initially thought possible. The quality of the ICEBEAR-3D data product has already led to three publications (Lozinsky et al., 2022; Huyghebaert et al., 2021; Ivarsen et al., 2022). With more upcoming publications including: Adapting Statistical Methods from Cosmology to study the Distribution of Farley-Buneman Scattering Centers in the Auroral Region (Ivarsen and Lozinsky, et al.); What E-region radar echo rates can tell us about Ionospheric Plasma Turbulence (Ivarsen, et al.); and three more untitled working articles which I have collaborated on.

And, many more to come...

References

Balanis, C. A. (2016). *Antenna theory analysis and design* (4th ed.). Wiley.

Barton, D. K. (1974). Low-angle radar tracking. *Proceedings of the IEEE*, *62*(6).

Boithias, L. (1987). *Radio wave propagation* (D. Beeson, Trans.). North Oxford Academic Publishers Ltd.

Bracewell, R. N. (1958). Radio interferometry of discrete sources. *Proceedings of the IRE*, *46*, 97-105.

Bradski, G. (2000). The OpenCV Library. *Dr. Dobb's Journal of Software Tools*.

Carozzi, T. (2015). Imaging on a sphere with interferometers: the spherical wave harmonic transform. *Monthly Notices of the Royal Astronomical Society: Letters Oxford University Press*, *451*.

Carozzi, T., & Woan, G. (2009). A generalized measurement equation and van Cittert-Zernike theorem for wide-field radio astronomical interferometry. *Monthly Notices of the Royal Astronomical Society*, *395(3)*. doi: 10.1111/j.1365-2966.2009.14642.x

Chau, J., & St-Maurice, J. (2016, 10). Unusual 5 m E region field-aligned irregularities observed from Northern Germany during the magnetic storm of 17 March 2015. *Journal of Geophysical Research: Space Physics*(7), 239. doi: 10.1002/2016JA023104

Chau, J., Urco, J. M., Vierinen, J. P., Volz, R. A., Clahsen, M., Pfeffer, N., & Trautner, J. (2019). Novel specular meteor radar systems using coherent MIMO techniques to study the mesosphere and lower thermosphere. *Atmospheric Measurement Techniques*, 2113-2127. doi: 10.5194/amt-12-2113-2019

Chisham, G., Burrell, A. G., Marchaudon, A., Shepherd, S. G., Thomas, E. G., & Ponomarenko, P. (2021). Comparison of interferometer calibration techniques for improved SuperDARN elevation angles. *Polar Science*, *28*, 100638. (SuperDARN / Studies of Geospace Dynamics - Today and Future) doi: 10.1016/j.polar.2021.100638

Clark, R. R. (1977). Meteor wind data for global comparisons. *Journal of Atmospheric and Solar-Terrestrial Physics*, 905-911.

Cornwell, T. J., & Perley, R. A. (1992). Radio-interferometric imaging of very large fields - the problem of non-coplanar arrays. *Astronomy and Astrophysics*, 353-364.

Galeschuk, D. (2021). *Verification and calibration of the ICEBEAR radar through GPU acceleration, noise characterization and calculation, and radio galaxy phase calibration* (Unpublished master's thesis). University of Saskatchewan, Saskatoon.

Glanz, F. H. (1971). Azimuth measuring system for a meteor trails radar. *IEEE Transactions on Geoscience Electronics*(1).

Haldoupis, C. (1989). A review on radio studies of auroral E-region ionospheric irregularities. *Annales Geophysicae*(121), 10,316–10,340.

Hocking, W. K., Fuller, B., & Vandepeer, B. (2001). Real-time determination of meteor-related parameters utilizing modern digital technology. *Journal of Atmospheric and Solar-Terrestrial Physics*, *63*, 115-169.

Holdsworth, D. A., & Reid, I. M. (2004). The buckland park mf radar: routine observation

scheme and velocity comparisons. *Annales Geophysicae*, *22*, 3815-3828.
Holdsworth, D. A., Reid, I. M., & Cervera, M. A. (2004). Buckland park all-sky interferometric meteor radar. *Radio Science*, *39*(RS5009). doi: 10.1029/2003RS003014
Hussey, G. C. (1995). *The polarisation of 50 MHz auroral backscatter* (Unpublished doctoral dissertation). University of Saskatchewan, Saskatoon.
Huyghebaert, D. (2019). *The ionospheric continuous-wave e region bistatic experimental auroral radar (ICEBEAR)* (Unpublished doctoral dissertation). University of Saskatchewan, Saskatoon.
Huyghebaert, D., Hussey, G. C., Vierinen, J., McWilliams, K. A., & St-Maurice, J. (2019, 4). ICEBEAR: An all-digital bistatic coded continuous-wave radar for studies of the e region of the ionosphere. *Radio Science*(54), 349-364. doi: 10.1029/2018RS006747
Huyghebaert, D., McWilliams, K., Hussey, G., Galeschuk, D., Chau, J. L., & Vierinen, J. (2021). Determination of the azimuthal extent of coherent E-Region scatter using the ICEBEAR linear receiver array. *Radio Science*, *56*(3). doi: 10.1029/2020RS007191
Hysell, D. (2018). *Antennas and radar for environmental scientists and engineers*. Cambridge University Press.
Ierkic, H. M., Haldoupis, C., Moorcroft, D. R., & Nielsen, E. (1992). Coherent radar interferometry of vertical irregularity structures in the auroral E region. *Radio Science*, *27*(5), 743-758.
Ivarsen, M. F., St-Maurice, J.-P., Hussey, G. C., Galeschuk, D., Lozinsky, A., Pitzel, B., & McWilliams, K. A. (2022). An algorithm to separate ionospheric turbulence radar echoes from those of meteor trails in large datasets. *Journal of Geophysical Research - Space Physics*(2022JA031050).
Jackson, J. D. (1999). *Classical electromagnetics*. John Wiley & Sons.
Jacobs, E., & Ralston, E. W. (1981). Ambiguity resolution in interferometry. *IEEE Transactions on Aerospace and Electronic Systems*(9), 17.
Janke, E., & Emde, F. (1945). *Tables of functions with formulae and curves*. New York: Dover.
Jones, J., et al. (1998, 2). An improved interferometer design for use with meteor radars. *Radio Science*, *33*(1), 55-65.
Kelly, M. C. (1989). *The earth's ionosphere plasma physics and electrodynamics* (2nd ed., Vol. 96). Academic Press.
Kerr, D. E. (1951). *Propagation of short radio waves* (1st ed.). McGraw-Hill Book Company, Inc.
Keto, E. (1997, 2). The shapes of cross-correlation interferometers. *The American Astronomical Society: The Astrophysical Journal*, *475*.
Kivelson, M., & Russel, C. (1995). *Introduction to space physics*. Cambridge University Press.
Lawrence Livermore National Laboratory. (2020). *Numerical electromagnetics code NEC-5*. Retrieved from `https://ipo.llnl.gov/technologies/it-and-communications/nec-v50-numerical-electromagnetic-code`
Lee, C., Jee, G., Kim, J.-H., & Song, I.-S. (2018). Meteor echo height ceiling effect and mesospheric temperature estimation from meteor radar observations. *Annales Geophysicae*, 21267-1274. doi: 10.5194/angeo-36-1267-2018
Liu, M. (2022). *Common data format*. Retrieved from `https://cdf.gsfc.nasa.gov/`

Lovberg, R. H., & Griem, H. R. (1971). *Methods of experimental physics* (Vol. 9 - Part B; Plasma Physics). New York: Academic Press.

Lozinsky, A., Hussey, G., McWilliams, K., Huyghebaert, D., & Galeschuk, D. (2022). ICEBEAR-3D: A low elevation imaging radar using a non-uniform coplanar receiver array for e region observations. *Radio Science*, *57*(3). doi: 10.1029/2021RS007358

McKinley, D. W. R. (1961). *Meteor science and engineering*. McGraw-Hill Book Company, Inc.

Nathanson, F. E., Reilly, J. P., & Cohen, M. N. (1991). *Radar design principles: Signal processing and the environment* (2nd ed.). Scitech Publishing, inc.

Offringa, A. R., Mckinley, B., Hurley-Walker, N., Briggs, F. H., Wyath, R. B., Kaplan, D. L., ... Hughes, J. D. (2014). WSCLEAN: An implementation of a fast, generic wide-field imager for radio astronomy. *Monthly Notices of the Royal Astronomical Society*, *444*, 606-619.

Richards, M. A., Scheer, J. A., & Holm, W. A. (2010). *Principles of modern radar: Basic principles* (Vol. 1). SciTech Publishing.

S. A. Holmes, W. E. F. (2002). A unified approach to the Clenshaw summation and the recursive computation of very high degree and order normalised associated Legendre functions. *Journal of Geodesy*, *76*, 279–299. doi: 10.1007/s00190-002-0216-2

Sahr, J. D., Farley, D. T., E.Swartz, W., & Providakes, J. F. (1991). The altitude of Type 3 auroral irregularities radar interferometer observations and implications. *Journal of Geophysical Research*, *96*(A10), 805-811.

Schwab, F. R. (1984). Relaxing the isoplanatism assumption in self-calibration; applications to low-frequency radio interferometry. *Astronomical Journal*, *89*, 1076-1081.

St-Maurice, J., & Chau, J. (2016, 9). A theoretical framework for the changing spectral properties of meter-scale Farley-Buneman waves between 90 and 125 km altitudes. *Journal of Geophysical Research: Space Physics*(121), 10,341-10,366. doi: 10.1002/2016JA023105

Sugar, G., Oppenheim, M. M., Bass, E., & Chau, J. L. (2010). Nonspecular meteor trail altitude distributions and durations observed by a 50 MHz high-power radar. *Journal of Geophysical Research*, *115*(A12334). doi: 10.1029/2010JA015705

Sullivan, W. T. (1991). Some highlights of interferometry in early radio astronomy. *Radio interferometry: Theory, techniques, and applications*.

Thompson, A. R., Moran, J. M., & Swenson, G. W. (2001). *Interferometry and synthesis in radio astronomy* (3rd ed.). John Wiley & Sons.

van Cittert, P. H. (1934). Die wahrscheinliche schwingungsverteilung in einer von einer lichtquelle direkt oder mittels einer linse beleuchteten ebene. *Physica*, *1*, 201-210.

Watermann, J. (1990). Refraction of 50-MHz radar waves in a realistic ionospheric model. *Radio Science*, *25*(5), 805-812. doi: 10.1029/RS025i005p00805

White, W. D. (1974). Low-angle radar tracking in the presence of multipath. *IEEE Trans. Aerospace and Electronic Systems*, *AES-10*(6).

Zernike, F. (1938). The concept of degree of coherence and its application to optical problems. *Physica*, *5*, 785-795.

Appendix A

Jacobs Ralston Algorithm

The Jacobs-Ralston phase error minimization technique for a linear array written in Python.

```
# Author: Adam Lozinsky
# Date: June 17, 2019
# Name: Jacobs Ralston
# Description: Use 'Ambiguity Resolution in Interferometry
#               (Jacobs,. Ralston, 1981)' to determine the
#               best antenna spacing in a crossed configuration.
import numpy as np


class JacobsRalston:
    def __init__(self, antennas, end, iterations, step=0.001, minsep=1.5):
        """
        For two antennas (antenna and end) this algorithm determines to optimal
        phase error minimization point to place a third antenna between the
        first two. This is then repeated as for as many (iterations) as
        required. A final average optimal point can be found. This process
        should be repeated for all possible combination of antennas along
        a linear array. Qualitative analysis must be used in conjunction.

        Parameters
        ----------
        antennas : float np.array
            [a1, a2, ...] the first antenna and any assumed or required
            antenna locations (<=iterations) in [lambda] from a1.
        end : float
            the last antenna location in [lambda] from a1.
        iterations : int
            number of antennas to place between a1 and end.
        step : float
            step size of the calculation, default = 0.1*lambda.
        minsep : float
            minimum distance two antennas can be placed in [lambda].
        """
        self.antennas = antennas
        self.end = end
        self.x = np.arange(antennas[0] + minsep, end - minsep, step)
        self.y = np.ones((iterations, self.x.shape[0]))
        self.step = step
        self.minsep = minsep
        self.iterations = iterations

        self.run()
```

```
        self.y_total = np.sum(self.y, axis=0) / len(self.y)
        self.antennas = np.append(self.antennas, self.end)

    def run(self):
        for i in range(self.iterations):
            self.y[i, :], pos = self.find_position(self.antennas[i], self.end)
            if i <= self.antennas.shape[0]:
                self.antennas = np.append(self.antennas, pos)
        return

    def find_position(self, x1, x2):
        """Find the next position for the antenna in the linear array. """
        x = np.arange(x1 + self.minsep, x2 - self.minsep, self.step)
        y = np.zeros_like(x)
        n1 = self.modulo_integer(np.abs(x2 - x1) / 2, np.pi / 2)
        for i in range(len(x)):
            n2 = self.modulo_integer(x[i], np.pi / 2)
            y[i] = 1 + self.find_lmin(np.abs(x2 - x1) / 2, x[i], n1, n2)
        idx = np.argmax(y)
        y = self.pad_like(y, self.x, value=1.0)
        return y, x[idx]

    @staticmethod
    def pad_like(arr, ref, value=0.0, mode='before'):
        """Pad the array either before or after with any value."""
        """Pad array given a reference"""
        pad = np.ones_like(ref) * value
        if mode is 'before':
            pad[ref.shape[0] - arr.shape[0]:] = arr
        elif mode is 'after':
            pad[:arr.shape[0]] = arr
        return pad

    @staticmethod
    def modulo_integer(d, theta_max):
        """Find the largest n (Jacobs and Ralston, 1981)."""
        nmax = int(np.abs(d * np.sin(theta_max) + 0.5))
        n = np.arange(-nmax, nmax, 1, dtype='int')
        return n

    @staticmethod
    def find_lmin(d1, d2, n1, n2):
        """Find the smallest l (Jacobs and Ralston, 1981)."""
        y = np.zeros((len(n1), len(n2)))
        for i in range(len(n1)):
            for j in range(len(n2)):
                y[i, j] = d1 / d2 * n2[j] - n1[i]
        y = np.sort(y.flatten())
        lmin = np.min((y[1::] - y[0:-1]) / ((1 + (d1 / d2) ** 2) ** 0.5))
        return lmin
```

Appendix B

Random-walk Annealing Algorithm

The Random-walk Annealing algorithm written in Python.

```
# Author: Adam Lozinsky
# Date: June 18, 2019
# Name: Random-walk Annealing
# Description: Generates optimal antenna array designs based on
#              perturbed realeaux triangles (Keto, 1997).
import numpy as np


class RandomWalkAnnealing:
    def __init__(self, antennas, wavelength, boundary, weights=np.array([]),
                 elasticity=2.0, dampening=0.1, uniformity=0.89, minsep=1.5,
                 limit=10000):
        """
        Random-walk Annealing is a simulated annealing like antenna array
        optimization algorithm. It attempts to find optimal array patterns
        where; the arrays are bounded, have minimal closure distance to
        avoid mutual coupling effects, desire all unique baselines, and
        uniformity of the uv-plane.

        Parameters
        ----------
        antennas : float np.array
            [[x1, y1], [x2, y2], ...] positions of the antennas in local
            coordinates [meters].
        wavelength : float
            array centered wavelength.
        boundary : float np.array
            [[xmin, xmax], [ymin, ymax]] the bounded region the antennas can
            be placed within.
        weights : float np.array
            [[w1, w1], [w2, w2], ...] the same shape as antennas, this holds
            the initial weights each antenna can be perturbed by.
            Set this to 0.0 to keep an antenna from ever moving.
        elasticity : float
            the amount of energy to add to an antennas if it is not
            placed well, w *= e.
        dampening : float
            the amount to reduce an antennas energy by if finds a
            local or global minima, w *= d.
        uniformity : float
            the maximum allowable distance two visibility points
            (location not value) can be next to each other.
```

```
        minsep : float
            the minimum distance two antenna can be placed next to
            each other in units of lambda.
        limit : int
            maximum number of iteration to preform per simulation.
        """
        if not weights:
            self.weights = np.ones_like(antennas) * 2.0
        self.num_antennas = len(antennas)
        self.unique_baselines = int(
            self.num_antennas * (self.num_antennas - 1) / 2)
        self.antennas = antennas
        self.baselines = np.zeros((self.unique_baselines, 2))
        self.order = np.zeros_like(self.baselines, dtype=int)
        self.wavelength = wavelength
        self.boundary_min = np.ones_like(antennas) * boundary[0, :]
        self.boundary_max = np.ones_like(antennas) * boundary[1, :]
        self.weights_maximum = np.abs(self.boundary_min - self.boundary_max)
        self.condition = np.ones_like(antennas, dtype=np.bool)
        self.elasticity = elasticity
        self.dampening = dampening
        self.uniformity = uniformity
        self.minsep = minsep
        self.limit = limit
        self.flag = True

        self.run()

    def run(self):
        count = 0
        while self.flag and (count < self.limit):
            print(f"\rsimulating␣iteration:\t{count:05d}/{self.limit}", end='')
            count += 1
            self.perturbate()
            self.evaluate()
            self.weighting()
        self.baselines = np.concatenate((self.baselines, -1 * self.baselines),
                                        axis=0)
        print('\tdone')
        return

    def perturbate(self):
        pmax = np.where(self.antennas + self.weights > self.boundary_max,
                        self.boundary_max,
                        self.antennas - self.weights)
        pmin = np.where(self.antennas - self.weights < self.boundary_min,
                        self.boundary_min,
                        self.antennas + self.weights)
        self.antennas = np.random.uniform(pmin, pmax)
        return

    def evaluate(self):
        self.condition *= False
        count = 0
```

```
        for i in range(self.num_antennas):
            for j in range(i + 1, self.num_antennas):
                self.baselines[count, :] = (self.antennas[i, :] -
                                            self.antennas[j, :]) / self.wavelength
                self.order[count, :] = np.array([i, j])
                # Check for minimal separation
                d = np.sqrt(self.baselines[count, 0] ** 2 + self.baselines[
                    count, 1] ** 2)
                if d <= self.minsep:
                    self.condition[i, :] = np.array([True, True])
                    self.condition[j, :] = np.array([True, True])
                count += 1
        rounded_baselines = np.copy(np.round(self.baselines, decimals=2))
        for m in range(len(self.baselines)):
            # Check for uniqueness
            if (rounded_baselines[m, :] in rounded_baselines[:m, :]) or \
                    (rounded_baselines[m, :] in rounded_baselines[m + 1:, :]):
                self.condition[self.order[m, 0], :] = np.array([True, True])
                self.condition[self.order[m, 1], :] = np.array([True, True])
            for n in range(m + 1, len(self.baselines)):
                # Check for uniformity
                d = np.sqrt(
                    np.sum((self.baselines[m, :] - self.baselines[n, :]) ** 2))
                if d < self.uniformity:
                    self.condition[self.order[m, 0], :] = np.array([True, True])
                    self.condition[self.order[m, 1], :] = np.array([True, True])
                    self.condition[self.order[n, 0], :] = np.array([True, True])
                    self.condition[self.order[n, 1], :] = np.array([True, True])
        if not np.alltrue(self.condition):
            self.flag = False

    def weighting(self):
        self.weights = np.where(self.condition, self.weights * self.elasticity,
                                self.weights * self.dampening)
        self.weights = np.where(
            self.antennas + self.weights > self.boundary_max,
            self.weights_maximum, self.weights)
        self.weights = np.where(
            self.antennas - self.weights < self.boundary_min,
            self.weights_maximum, self.weights)
        return
```

Appendix C

Target Simulator

The ICEBEAR target simulator written in Python.

```
import matplotlib.pyplot as plt
import numpy as np
from scipy.integrate import dblquad
import multiprocessing as mp
from icebear import swht
import icebear.utils as utils


def _real_pre_integrate(theta, phi, u_in, v_in, w_in, \
                        theta_mean, theta_spread, phi_mean, phi_spread):
    return 2 * np.real(np.exp(-(theta - theta_mean) ** 2 /
           (2.0 * theta_spread * theta_spread)) *
           np.exp(-(phi - phi_mean) ** 2 /
           (2.0 * phi_spread * phi_spread)) * np.cos(phi) *
           np.exp(-2.0j * np.pi * ((u_in * np.sin(theta) * np.cos(phi)) +
           (v_in * np.cos(theta) * np.cos(phi)) + (w_in * np.sin(phi)))))


def _imag_pre_integrate(theta, phi, u_in, v_in, w_in, \
                        theta_mean, theta_spread, phi_mean, phi_spread):
    return 2 * np.imag(np.exp(-(theta - theta_mean) ** 2 /
           (2.0 * theta_spread * theta_spread)) *
           np.exp(-(phi - phi_mean) ** 2 /
           (2.0 * phi_spread * phi_spread)) * np.cos(phi) *
           np.exp(-2.0j * np.pi * ((u_in * np.sin(theta) * np.cos(phi)) +
           (v_in * np.cos(theta) * np.cos(phi)) + (w_in * np.sin(phi)))))


def _visibility_calculation(x, u_in1, v_in1, w_in1, \
                            theta_mean, theta_spread, \
                            phi_mean, phi_spread, output):
    real_vis = dblquad(_real_pre_integrate, -np.pi / 2, np.pi / 2, \
                       lambda phi: -np.pi, lambda phi: np.pi,
                       args=(u_in1, v_in1, w_in1, \
                       theta_mean, theta_spread, phi_mean, phi_spread))[0]
    imag_vis = dblquad(_imag_pre_integrate, -np.pi / 2, np.pi / 2, \
                       lambda phi: -np.pi, lambda phi: np.pi,
                       args=(u_in1, v_in1, w_in1, \
                       theta_mean, theta_spread, phi_mean, phi_spread))[0]
    output.put((x, real_vis + imag_vis * 1.0j))
```

```
def simulate(config, azimuth, elevation, azimuth_extent, elevation_extent):
    """
    Parameters
    ----------
    config : Class Object
        Config class instantiation.
    azimuth : float np.array
        Azimuth angles of simulated targets.
    elevation : float np.array
        Elevation angles of simulated target.
    azimuth_extent : float np.array
        Azimuth spatial extents of simulated targets.
    elevation_extent : float np.array
        Elevation spatial extents of simulated targets.

    Returns
    -------
    brightness : float np.array
        Brightness map using the Suppressed-SWHT.
    swht_brightness : float np.array
        Brightness map using the SWHT.
    """
    print('simulation start:')
    print("Number of processors: ", mp.cpu_count())
    print(f'\t-input azimuth {azimuth} deg x {azimuth_extent} deg')
    print(f'\t-input elevation {elevation} deg x {elevation_extent} deg')

    idx_length = len(azimuth)
    wavelength = 299792458 / config.center_freq
    x = config.rx_ant_coords[0, :]
    y = config.rx_ant_coords[1, :]
    z = config.rx_ant_coords[2, :]
    # Simulate positional errors
    err = 0.0
    x[7] += err
    y[7] += err
    z[7] += err
    u, v, w = utils.baselines(x, y, z, wavelength)

    azimuth = np.deg2rad(azimuth)
    elevation = np.deg2rad(elevation)
    azimuth_extent = np.deg2rad(azimuth_extent)
    elevation_extent = np.deg2rad(elevation_extent)
    visibility_dist = np.zeros((int(len(u)/2), idx_length, idx_length,
                                idx_length, idx_length), dtype=np.complex64)

    # Instantiate multi-core processing
    output = mp.Queue()
    pool = mp.Pool(mp.cpu_count() - 2)

    # Loop process to allow for multiple targets in an image.
    # Typically only one target is used.
    for idx in range(idx_length):
        processes = [mp.Process(target=_visibility_calculation,
```

```
                    args=(x, u[x], v[x], w[x],
                          azimuth[idx], azimuth_extent[idx],
                          elevation[idx], elevation_extent[idx],
                          output)) for x in range(int(len(u)/2))]
        for p in processes:
            p.start()
        for p in processes:
            p.join()

        # Get process results from the output queue
        visibility_dist_temp = [output.get() for p in processes]

        visibility_dist_temp.sort()
        visibility_dist[:, idx, idx, idx, idx] = \
                        [r[1] for r in visibility_dist_temp]

        # for p in processes:
        #     p.close()

    visibility = np.array(visibility_dist)
    for i in range(len(azimuth)):
        visibility[:, i, i, i, i] = visibility[:, i, i, i, i] /
                                    np.abs(visibility[0, i, i, i, i])
    visibility = np.sum(visibility_dist, axis=(1, 2, 3, 4))
    visibility = np.append(np.conjugate(visibility), visibility)
    coeffs = swht.unpackage_coeffs(config.swht_coeffs, int(config.lmax))
    coeffs2 = np.copy(coeffs)

    brightness = swht.swht_py(visibility, coeffs)
    for i in range(15, 85, 10):
        coeffs = .swht.unpackage_coeffs(config.swht_coeffs, i)
        brightness *= swht.swht_py(visibility, coeffs)
    brightness = swht.brightness_cutoff(brightness, threshold=0.0)
    # Find the target center point
    cx, cy, cx_extent, cy_extent, area = swht.centroid_center(brightness)
    mx, my, _ = swht.max_center(brightness)

    mx = mx * config.resolution - config.fov[0, 0] + config.fov_center[0]
    my = my * config.resolution - config.fov[1, 0] + config.fov_center[1]
    cx = cx * config.resolution - config.fov[0, 0] + config.fov_center[0]
    cy = cy * config.resolution - config.fov[1, 0] + config.fov_center[1]
    cx_extent *= config.resolution
    cy_extent *= config.resolution
    print(f'\t-result azimuth {cx} deg x {cx_extent} deg -- max {mx}')
    print(f'\t-result elevation {cy} deg x {cy_extent} deg -- max {my}')
    if len(azimuth) == 0:
        if np.allclose([azimuth, elevation, azimuth_extent, elevation_extent],
                       [cx, cy, cx_extent, cy_extent], atol=1):
            print('\t-result matches input within error (10e-1)')

    swht_brightness = swht.swht_py(visibility, coeffs2)
    swht_brightness = swht.brightness_cutoff(swht_brightness, threshold=0.0)

    return brightness, swht_brightness
```

Appendix D

Spherical Wave Harmonic Coefficient Matrices

Spherical Wave Harmonic Transform coefficient matrix computation written in Python.

```
# Author: Adam Lozinsky
# Date: November 5, 2019
# Name: SWHT Coeffs
# Description: Generates the SWHT pre-calculated coeffs for caching
import numpy as np
import scipy.special as special
import time
import common.utils as utils
import h5py
import cv2

try:
    import cupy as cp
except:
    print('no␣cupy')


def generate_coeffs(config, fov=np.array([[0, 360], [0, 90]]), resolution=1.0,
                    lmax=85):
    """
    Makes an array containing all the factors that do not change with
    Visibility values. This array can then be saved to quickly create
    Brightness values given changing Visibilities. The array is then
    stored as a HDF5 file.

    Parameters
    ----------
        config : Class Object
            Config class instantiation.
        fov : float np.array
            [[start, stop], [start, stop]] azimuth, elevation angles
            within 0 to 360 and 0 to 180 degrees.
        resolution : float
            Angular resolution in degree per pixel.
        lmax : int
            The maximum harmonic degree.

    Returns
    -------
        None

    Notes
```

```
-----
    The array file must contain:
    wavelength : float
        Radar signal wavelength in meters.
    u : float np.array
        East-West baseline coordinate divided by wavelength.
    v : float np.array
        North-South baseline coordinate divided by wavelength.
    w : float np.array
        Altitude baseline coordinate divided by wavelength.
"""

array_name = config.radar_config
wavelength = 299792458 / config.center_freq
date_created = config.date_created
u, v, w = utils.baselines(config.rx_ant_coords[0, :],
                          config.rx_ant_coords[1, :],
                          config.rx_ant_coords[2, :],
                          wavelength)
if config.check_attr('fov'):
    fov = config.fov
if config.check_attr('resolution'):
    resolution = config.resolution
if config.check_attr('lmax'):
    lmax = config.lmax
ko = 2 * np.pi / wavelength
az_step = int(np.abs(fov[0, 0] - fov[0, 1]) / resolution)
el_step = int(np.abs(fov[1, 0] - fov[1, 1]) / resolution)
r, t, p = utils.uvw_to_rtp(u, v, w)
r *= wavelength  # Since r, t, p was converted from u, v, w we
# need the * wavelength back to match SWHT algorithm
az = np.deg2rad(np.linspace(fov[0, 0], fov[0, 1], az_step))
el = np.deg2rad(np.linspace(fov[1, 0], fov[1, 1], el_step))
setting_name = f"{int(np.round(np.abs(fov[0, 0] - fov[0, 1]))):03d}az_" \
               f"{int(np.round(np.abs(fov[1, 0] - fov[1, 1]))):03d}el_" \
               f"{str(resolution).replace('.', '')}res_" \
               f"{lmax}lmax"
filename = f"swhtcoeffs_{array_name}_{date_created[0]:04d}_" \
           f"{date_created[1]:02d}_{date_created[2]:02d}_" \
           f"{setting_name}.h5"

print(f"Calculating SWHT coeffs:")
print(f"\t-filename: {filename}")
print(f"\t-configuration: {array_name}")
print(f"\t-azimuth: {fov[0, 0]} - {fov[0, 1]}")
print(f"\t-elevation: {fov[1, 0]} - {fov[1, 1]}")
print(f"\t-resolution: {resolution}")
print(f"\t-degree: {lmax}")
print(f"\t-wavelength: {wavelength}")

create_coeffs(filename, date_created, array_name, fov, resolution, lmax,
              wavelength, np.array([u, v, w]))
calculate_coeffs(filename, az, el, ko, r, t, p, lmax)
```

```
    return filename


def create_coeffs(filename, date_created, array_name, fov, resolution, lmax,
                  wavelength, baselines):
    """
    Generates a HDF5 file to save the metadata and coeffs ndarrays.
    """

    f = h5py.File(filename, 'w')
    f.create_dataset('radar_config', data=np.array(array_name, dtype='S'))
    f.create_dataset('date_created', data=date_created)
    f.create_dataset('fov', data=fov)
    f.create_dataset('resolution', data=resolution)
    f.create_dataset('lmax', data=lmax)
    f.create_dataset('wavelength', data=wavelength)
    f.create_dataset('baselines', data=baselines)
    f.create_group('coeffs')
    f.close()

    return None


def append_coeffs(filename, l, coeffs):
    """
    Appends the HDF5 file with a new coeffs ndarray.
    """

    f = h5py.File(filename, 'a')
    f.create_dataset(f'coeffs/{l:02d}', data=coeffs)
    f.close()

    return None


def calculate_coeffs(filename, az, el, ko, r, t, p, lmax=85):
    """
    Computes the coeff matrix for each harmonic order and degree

    Parameters
    ----------
        filename : string
            Filename and path to the HDF5 file the calculated
            coefficients are to be appended.
        az : float np.array
            An array of azimuth angles in radians to calculate
            coefficients for.
        el : float np.array
            An array of elevation angles in radians to calculate
            coefficients for.
        lmax : int
            The maximum harmonic degree.
        ko : float
            Radar signal wave number, ko = 2pi/wavelength.
```

```
    r : float np.array
        Radius baseline coordinate divided by wavelength.
    t : float np.array
        Theta (elevation) baseline coordinate.
    p : float np.array
        Phi (azimuthal) baseline coordinate.

Returns
-------
    None

Notes
-----
    Maximum harmonic degree is Lmax = 85. Above this scipy crashes due
    to an overflow error. The potential fix is to scale the initial Pmm
    of the recursion by 10^280 sin^m (theta), and then rescale
    everything back at the end.

    Holmes, S. A., and W. E. Featherstone, A unified approach to the
    Clenshaw summation and the recursive computation of very high degree
    and order normalised associated Legendre functions,
    J. Geodesy, 76, 279- 299, doi:10.1007/s00190-002-0216-2, 2002.
"""

start_time = time.time()
AZ, EL = np.meshgrid(az, el)
coeffs = np.zeros((len(el), len(az), len(r)), dtype=np.complex128)

if lmax <= 85:
    for l in range(lmax + 1):
        for m in range(-l, l + 1):
            coeffs += ko ** 2 / (2 * np.pi ** 2 * np.round((-1j) ** l)) * \
                    np.repeat(
                    special.sph_harm(m, l, AZ, EL)[:, :, np.newaxis],
                    len(r), axis=2) * \
                    np.repeat(np.repeat(special.spherical_jn(l, ko * r) * \
                    np.conjugate(
                    special.sph_harm(m, l, p, t)) \
                    [np.newaxis, np.newaxis, :],
                    AZ.shape[0], axis=0), AZ.shape[1],axis=1)
            print(f"\tharmonic degree (l) = {l:02d}/{lmax:02d},"
                  f" order (m) = {m:02d}/{l:02d}\r")
        if l in [5, 15, 25, 35, 45, 55, 65, 75, 85]:
            append_coeffs(filename, l, coeffs)

elif lmax > 85:
    try:
        import pyshtools as pysh
    except ImportError:
        print(f'Error: lmax = {lmax} -- values over 85 requires PySHTOOLS '
              f'https://github.com/SHTOOLS try pip install pyshtools')
        exit()
    print(
        f'\twarning: lmax values over 85 generate massive '
```

```
            f'files␣only␣1/10th␣frames␣will␣be␣stored,␣evenly␣distributed')
        ylm_pysh = np.vectorize(pysh.expand.spharm_lm)
        for l in range(lmax + 1):
            for m in range(-l, l + 1):
                coeffs += ko ** 2 / (2 * np.pi ** 2 * np.round((-1j) ** l)) * \
                    np.repeat(
                    ylm_pysh(l, m, EL, AZ, normalization='ortho',
                    csphase=-1, kind='complex',
                    degrees=False)[
                    :, :, np.newaxis], len(r), axis=2) * \
                    np.repeat(np.repeat(special.spherical_jn(l, ko * r) * \
                    np.conjugate(ylm_pysh(l, m, t, p,
                    normalization='ortho',
                    csphase=-1,
                    kind='complex',
                    degrees=False)) \
                    [np.newaxis, np.newaxis, :],
                    AZ.shape[0], axis=0), AZ.shape[1], axis=1)
                print(f"\tharmonic␣degree␣(l)␣=␣{l:02d}/{lmax:02d},"
                      f"␣order␣(m)␣=␣{m:02d}/{l:02d}\r")
            if l == 85:
                append_coeffs(filename, l, coeffs)
            if l == int(lmax * 0.1):
                append_coeffs(filename, l, coeffs)
            if l == int(lmax * 0.2):
                append_coeffs(filename, l, coeffs)
            if l == int(lmax * 0.3):
                append_coeffs(filename, l, coeffs)
            if l == int(lmax * 0.4):
                append_coeffs(filename, l, coeffs)
            if l == int(lmax * 0.5):
                append_coeffs(filename, l, coeffs)
            if l == int(lmax * 0.6):
                append_coeffs(filename, l, coeffs)
            if l == int(lmax * 0.7):
                append_coeffs(filename, l, coeffs)
            if l == int(lmax * 0.8):
                append_coeffs(filename, l, coeffs)
            if l == int(lmax * 0.9):
                append_coeffs(filename, l, coeffs)
        append_coeffs(filename, l, coeffs)

    print(f"Complete␣time:␣\t{time.time()␣-␣start_time}")

    return None
```

Appendix E

Ray Tracing Refraction Model

Ray tracing refraction model for a linear electron density E region written in Python.

```
import numpy as np
import matplotlib.pyplot as plt


def ray_trace(angle_of_arrival, ground_distance, frequency, step):
    ranges = np.arange(0, ground_distance, step)
    theta = angle_of_arrival
    n1 = 1.0
    altitudes = np.array([])
    height = 0.0
    for s in range(len(ranges)):
        if (height < 80) or (height > 120):
            height = height + 2 * (6378.1 + height) *
                     np.sin(step / 6378.1 / 2) * np.tan(theta)
        elif height >= 80:
            height = height + 2 * (6378.1 + height) *
                     np.sin(step / 6378.1 / 2) * np.tan(theta)
            n2 = refractive_index(height, frequency)
            theta = snells_law(n2, n1, theta)
            n1 = n2

        altitudes = np.append(altitudes, height)
    return ranges, altitudes


def refractive_index(altitude, frequency):
    N = density_model(altitude)
    return np.sqrt(1-(81*N)/frequency**2)


def density_model(altitude):
    # Watermann (1990) says peak is 3.1x10^11 m^-3 at 115 km
    peak = 5e12
    a = 115
    b = 6e6
    m = (peak - b) / (a-80)
    return (altitude - 80) * m + b


def snells_law(n1, n2, theta1):
    return np.arcsin(n1/n2 * np.sin(theta1))
```

Appendix F

The Role of Γ in All Types of Radar Observations

This appendix contains work directly from my contributions in Lozinsky et al. (2022).[1]

The impact of the geocentral angle Γ on proper elevation angle α determination using vertical interferometry on a curved surface such as the Earth depends significantly on the magnitude of the slant range ρ. This influences how significant Γ is in proper determination of α. Variation of values of slant range ρ can be used to define three general regimes:

1. Regime I: $0 < h < \approx 0.1 R_E$ ($\approx$1000 km)
2. Regime II: $\approx 0.1 R_E < h < 10 R_E$
3. Regime III: $h > 10 R_E \rightarrow \infty$

Example target altitudes for Regime I for 10 km, 100 km, and 1000 km are presented in Table F.1 and Figure F.1 and includes E region altitudes as already discussed for ICEBEAR-3D. In this regime low elevation angles are significantly affected, for example, with Γ values of 3.2°, 10.1°, and 30.2° at altitudes of 10 km, 100 km, and 1000 km respectively for true $\alpha = 0°$ values. The value of Γ does not become $< 1°$, and therefore around typical calibration and measurement errors, until the true value of α reaches 6°, 45°, and 82° at the respective altitudes. As already presented and discussed, clearly not properly accounting for the geocentral angle Γ in the geometry for vertical interferometry at finite slant ranges introduces significant error.

Regime III represents target observations at very high altitudes ($> 10^5$ km)/slant ranges out to infinity. In this regime of $h > \approx 10 R_E$ km $\rightarrow \infty$, $\rho \simeq (R_E + h) \simeq h$ and $\chi \rightarrow 0°$, then from Equation 5.10 $\alpha = \pi/2 - \Gamma$. Therefore, there is a fixed phase difference between the elevation angle α and the geocentral angle Γ such that $\sin\alpha = \sin(\pi/2 - \Gamma) = \cos\Gamma$ or $\cos\alpha = \cos(\pi/2 - \Gamma) = \sin\Gamma$. Albeit, for such vertical interferometer implementations,

[1] Lozinsky, A., Hussey, G., McWilliams, K., Huyghebaert, D., and Galeschuk, D. (2022). ICEBEAR-3D: A Low Elevation Imaging Radar Using a Non-Uniform Coplanar Receiver Array for E Region Observations, *Radio Science*, 57(3). DOI: 10.1029/2021RS007358

Table F.1: Actual elevation angle α and corresponding geocentral angle Γ, incorrect conventional elevation angle α_C, and slant range ρ for measurements of vertical interferometry targets at altitudes of 10 km, 100 km, and 1000 km. Targets can be aircraft, plasma instabilities, meteor trails, beacons, etc.

α	Alt. $h = 10$ km			Alt. $h = 100$ km			Alt. $h = 1000$ km		
	Γ	α_C	ρ	Γ	α_C	ρ	Γ	α_C	ρ
(°)	(°)	(°)	(km)	(°)	(°)	(km)	(°)	(°)	(km)
0	3.21	3.21	357.1	10.09	10.09	1133.2	30.19	30.19	3707.0
2	1.78	3.78	198.3	8.28	10.28	932.5	28.25	30.25	3491.3
4	1.13	5.13	125.7	6.84	10.84	772.8	26.43	30.43	3289.2
6	0.80	6.80	89.7	5.72	11.72	648.5	24.73	30.73	3100.4
8	0.62	8.62	69.2	4.85	12.85	552.2	23.14	31.14	2924.9
10	0.50	10.50	56.2	4.17	14.17	477.4	21.66	31.66	2762.3
20	0.25	20.25	29.1	2.31	22.31	277.1	15.69	35.69	2121.0
30	0.16	30.16	20.0	1.50	31.50	195.6	11.54	41.54	1702.2
45	0.09	45.09	14.1	0.88	45.88	140.4	7.33	52.33	1329.1
60	0.05	60.05	11.5	0.51	60.51	115.2	4.39	64.39	1129.7
90	0.00	90.00	10.0	0.00	90.00	100.0	0.00	90.00	1000.0

calibrations should account for the geocentral angle Γ and it need not be explicitly taken into account for these extremely high altitude/large slant range/ ∞ observations.

Regime II represents the intermediate case between Regimes I and III and is presented, with an example altitude of $h = 10^4$ km, in Table F.2 and by the red dotted line in Figure F.1. Here the geocentral angle Γ has a significant impact on proper elevation angle α determination at all elevation angles α.

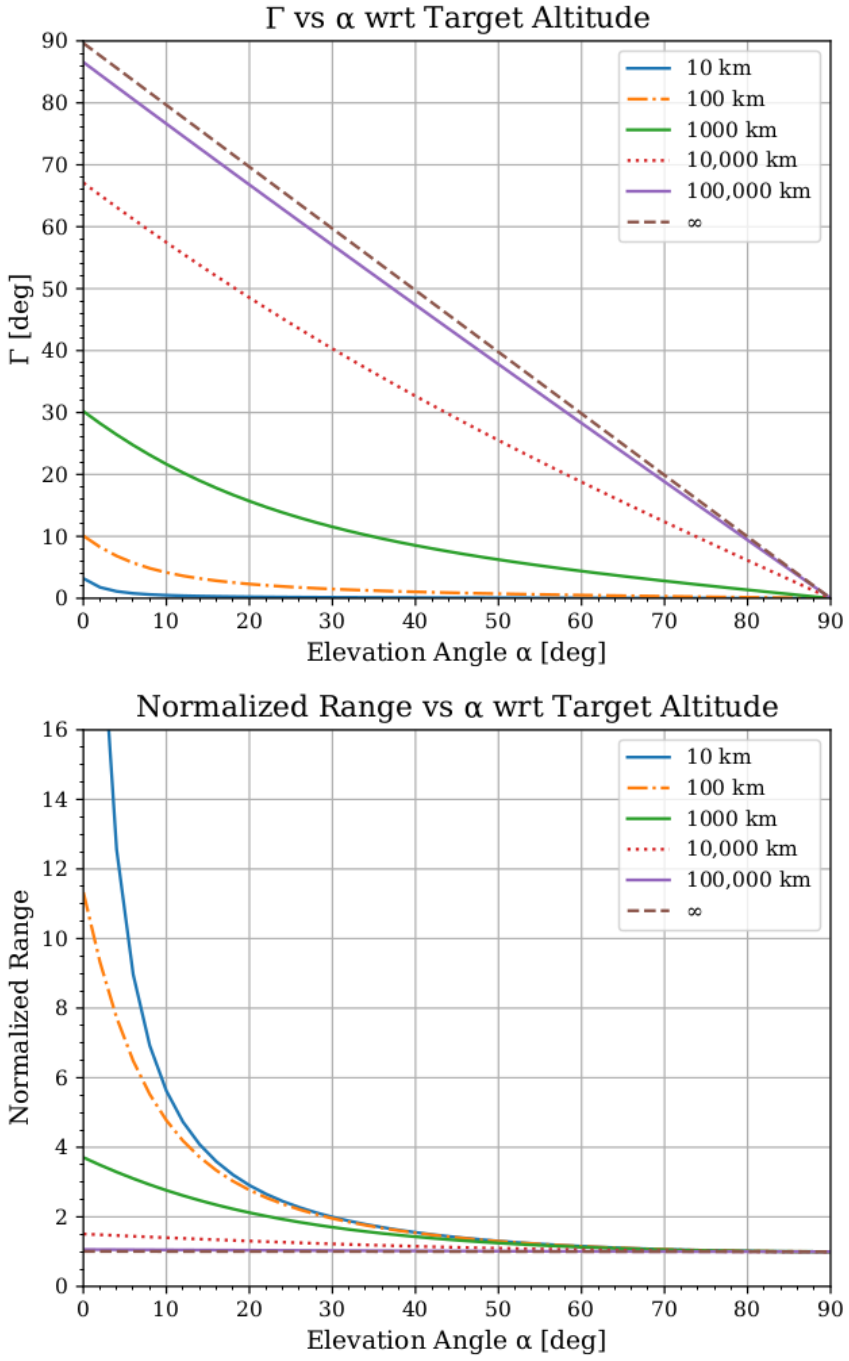

Figure F.1: The geocentral angle Γ (top) and the normalized slant range (bottom) versus the elevation angle α for varying target altitudes. Presented are the three regimes: I up to $0.1R_E$; II for $0.1R_E$ to $10R_E$; and III for $10R_E$ to ∞, showing the impact of the geocentral angle Γ on proper elevation angle α determination using vertical interferometry. Note that the normalized range is 35.7 at $\alpha = 0°$ at an altitude of $h = 10$ km.

Table F.2: Same as Table F.1 but for target altitudes of 10,000 km, 100,000 km, and ∞.

α	Alt. $h = 10^4$ km			Alt. $h = 10^5$ km			Alt. ∞ km		
	Γ	α_C	ρ	Γ	α_C	ρ	Γ	α_C	ρ
(°)	(°)	(°)	(km)	(°)	(°)	(km)	(°)	(°)	(km)
0	67.10	67.10	15,080	86.57	86.57	106,200	90.0	90.0	∞
2	65.11	67.11	14,860	84.57	86.57	106,000	88.0	90.0	∞
4	63.16	67.16	14,640	82.57	86.57	105,700	86.0	90.0	∞
6	61.23	67.23	14,430	80.59	86.59	105,600	84.0	90.0	∞
8	59.33	67.33	14,220	78.60	86.60	105,300	82.0	90.0	∞
10	57.46	67.46	14,020	76.62	86.62	105,100	80.0	90.0	∞
20	48.55	68.55	13,060	66.77	86.77	104,000	70.0	90.0	∞
30	40.30	70.30	12,230	57.03	87.03	103,000	60.0	90.0	∞
45	29.03	74.03	11,230	42.57	87.57	101,800	45.0	90.0	∞
60	18.78	78.78	10,540	28.28	88.28	100,800	30.0	90.0	∞
90	0.00	90.00	10,000	0.00	90.00	100,000	0.0	90.0	∞

Appendix G

Relaxation Geocentral Angle

The relaxation numerical method coupled with the geodesy calculation for determination of the geocentral angle written in Python.

```
import numpy as np
import sys
try:
    import cupy as xp
    CUDA = True
except ModuleNotFoundError:
    import numpy as xp
    CUDA = False
import h5py
import pymap3d as pm
import icebear.utils as utils
import matplotlib.pyplot as plt
import icebear.imaging.clustering as cl
import datetime
from dateutil.tz import tzutc
import pandas

def map_target(tx, rx, az, el, rf, dop, wavelength):
    """
    Find the scatter location given tx location, rx location, total
    rf distance, and target angle-of-arrival using the 'WGS84' Earth model.
    Also determines the bistatic velocity vector and bistatic
    radar wavelength.

    Parameters
    ----------
        tx : float np.array
            [latitude, longitude, altitude] of tx array in degrees
            and kilometers
        rx : float np.array
            [latitude, longitude, altitude] of rx array in degrees
            and kilometers
        az : float np.array
            angle-of-arrival azimuth in degrees
        el : float np.array
            angle-of-arrival elevation in degrees
        rf : float np.array
            total rf path distance rf = c * tau in kilometers
        dop : float np.array
            doppler shift in hertz
        wavelength : float
```

```
        radar signal center wavelength

Returns
-------
    sx : float np.array
        [latitude, longitude, altitude] of scatter in degrees
        and kilometers
    sa : float np.array
        [azimuth, elevation, slant range] of scatter in degrees
        and kilometers
    sv : float np.array
        [azimuth, elevation, velocity] the bistatic Doppler velocity
        vector in degrees and kilometers. Coordinates given in the
        scattering targets local frame (azimuth from North, elevation up
        from the plane normal to zenith,
        Doppler [Hz] * lambda/(2 cos(e/2)))

Notes
-----
tx : transmitter location
rx : receiver location
sx : scatter location
gx : geometric center of Earth, origin
u_rt : unit vector rx to tx
u_rs : unit vector rx to sx
u_gt : unit vector gx to tx
u_gr : unit vector gx to rx
u_gs : unit vector gx to sx
"""

# Initialize output arrays
sx = np.zeros((3, len(rf)), dtype=float)
sa = np.zeros((3, len(rf)), dtype=float)
sv = np.zeros((3, len(rf)), dtype=float)

# Setup variables in correct units for pymap3d
rf = rf * 1.0e3
az = np.where(az < 0.0, az + 360.0, az)
az = np.deg2rad(az)
el = np.deg2rad(np.abs(el))

# Determine the slant range, r
bx1, by1, bz1 = pm.geodetic2ecef(rx[0], rx[1], rx[2], \
                                 ell=pm.Ellipsoid("wgs84"), deg=True)
v_gr = np.array([bx1, by1, bz1])
bx2, by2, bz2 = pm.geodetic2ecef(tx[0], tx[1], tx[2], \
                                 ell=pm.Ellipsoid("wgs84"), deg=True)
v_gt = np.array([bx2, by2, bz2])
raz, rel, b = pm.ecef2aer(bx2, by2, bz2, rx[0], rx[1], rx[2], \
                          ell=pm.Ellipsoid("wgs84"), deg=True)
u_rt = np.array([np.sin(np.deg2rad(raz)) * np.cos(np.deg2rad(rel)),
                 np.cos(np.deg2rad(raz)) * np.cos(np.deg2rad(rel)),
                 np.sin(np.deg2rad(rel))])
el -= relaxation_elevation(el, rf, az, b, u_rt)
```

```
    u_rs = np.array([np.sin(az) * np.cos(el), \
                     np.cos(az) * np.cos(el), np.sin(el)])
    r = (rf ** 2 - b ** 2) / (2 * (rf - b * np.dot(u_rt, u_rs)))

    # WGS84 Model for lat, long, alt
    sx[:, :] = pm.aer2geodetic(np.rad2deg(az), np.rad2deg(el), np.abs(r),
                               np.repeat(np.rad2deg(rx[0]), len(az)),
                               np.repeat(np.rad2deg(rx[1]), len(az)),
                               np.repeat(rx[2], len(az)),
                               ell=pm.Ellipsoid("wgs84"), deg=True)

    # Determine the bistatic Doppler velocity vector
    x, y, z = pm.geodetic2ecef(sx[0, :], sx[1, :], sx[2, :],
                               ell=pm.Ellipsoid('wgs84'), deg=True)
    v_gs = np.array([x, y, z])
    v_bi = (-1 * v_gs.T + v_gt / 2.0 + v_gr / 2.0).T
    u_bi = v_bi / np.linalg.norm(v_bi, axis=0)
    v_sr = (v_gr - v_gs.T).T
    u_sr = v_sr / np.linalg.norm(v_sr, axis=0)
    radar_wavelength = wavelength / \
                       np.abs(2.0 * np.einsum('ij,ij->j', u_sr, u_bi))
    # 1 for positive, -1 for negative, and 0 for zero
    doppler_sign = np.where(dop >= 0, 1, -1)
    vaz, vel, _ = pm.ecef2aer(doppler_sign * u_bi[0, :] + x,
                              doppler_sign * u_bi[1, :] + y,
                              doppler_sign * u_bi[2, :] + z,
                              sx[0, :], sx[1, :], sx[2, :],
                              ell=pm.Ellipsoid("wgs84"), deg=True)

    # Convert back to conventional units
    sx[2, :] /= 1.0e3
    az = np.rad2deg(az)
    el = np.rad2deg(el)
    sa[:, :] = np.array([az, el, r / 1.0e3])
    sv[:, :] = np.array([vaz, vel, dop * radar_wavelength])

    return sx, sa, sv


def relaxation_elevation(beta, rf_distance, azimuth, \
                         bistatic_distance, bistatic_vector):
    """
    Due to the bistatic nature of ICEBEAR the problem of solving
    range and elevation is transcendental. This relaxation method applies
    numerical relaxation to derive a solution. Usually 2-3 iterations.

    Parameters
    ----------
    beta : float np.array
        Measured elevation angle in radians
    rf_distance : float np.array
        Total rf propagation distance in kilometers
    azimuth : float np.array
        Measured azimuth angle in radians
```

```
bistatic_distance : float
    The distance separating the transmitter and receiver in kilometers
bistatic_vector : float np.array
    Unit vector from the receiver to the transmitter

Returns
-------
m : float np.array
    Relaxed angle gamma in radians
"""
n = 3
radius_of_earth = 6378.0e3
err = np.deg2rad(1.0)
target = np.deg2rad(0.1)
m = np.zeros((3, len(beta)))
m[1, :] = 0.1
v = np.array(
    [np.sin(azimuth) * np.cos(beta - m[1, :]), np.cos(azimuth) * \
    np.cos(beta - m[1, :]), np.sin(beta - m[1, :])])
r = (rf_distance ** 2 - bistatic_distance ** 2) / (
     2 * (rf_distance - bistatic_distance * \
    (np.dot(bistatic_vector, v))))
m[2, :] = 1 / (radius_of_earth / r + np.sin(beta) / 2)
while np.nanmean(err) > target:
    m[0, :] = m[1, :]
    m[1, :] = m[2, :]
    v = np.array([np.sin(azimuth) * np.cos(beta - m[1, :]), \
                  np.cos(azimuth) * \
                  np.cos(beta - m[1, :]), \
                  np.sin(beta - m[1, :])])
    r = (rf_distance ** 2 - bistatic_distance ** 2) / (
         2 * (rf_distance - bistatic_distance * \
        (np.dot(bistatic_vector, v))))
    m[2, :] = 1 / (radius_of_earth / r + np.sin(beta) / 2)
    err = np.abs((m[1, :] - m[2, :]) ** 2 / \
                 (2 * m[1, :] - m[0, :] - m[2, :]))
    n += 1

m[2, :] = np.where(err >= target, np.nan, m[2, :])
return m[2, :]
```